UNIVERSIDADE FEDERAL DO RIO GRANDE DO SUL
INSTITUTO DE GEOCIÊNCIAS
PROGRAMA DE PÓS-GRADUAÇÃO EM GEOCIÊNCIAS

EVOLUÇÃO CRUSTAL EO A MESOARQUEANA DA PARTE NORTE DO CRÁTON DO SÃO FRANCISCO: ASPECTOS GEOCRONOLÓGICOS E ISOTÓPICOS.

RAFAEL GORDILHO BARBOSA

ORIENTADOR – Prof. Dr. Rommulo Vieira Conceição

CO-ORIENTADOR – Prof. Dr. Felipe Padilha Leitzke

Porto Alegre, 2023

UNIVERSIDADE FEDERAL DO RIO GRANDE DO SUL
INSTITUTO DE GEOCIÊNCIAS
PROGRAMA DE PÓS-GRADUAÇÃO EM GEOCIÊNCIAS

EVOLUÇÃO CRUSTAL EO A MESOARQUEANA DA PARTE NORTE DO CRÁTON DO SÃO FRANCISCO: ASPECTOS GEOCRONOLÓGICOS E ISOTÓPICOS

RAFAEL GORDILHO BARBOSA

Orientador – Prof. Dr. Rommulo Vieira Conceição

Co-orientador – Prof. Dr. Felipe Padilha Leitzke

Banca examinadora:

Prof. Dr. Lauro Valentim Stoll Nardi – Universidade Federal do Rio Grande do Sul

Profa. Dra. Anelise Losangela Bertotti – Universidade Federal de Pernambuco

Profa. Dra. Angela Beatriz de Menezes Leal – Universidade Federal da Bahia

Tese de Doutorado apresentada como requisito parcial para obtenção do Título de Doutor em Ciências.

Porto Alegre, 2023

FICHA CATALOGRÁFICA

CIP - Catalogação na Publicação

Gordilho Barbosa, Rafael
Evolução Crustal eo a mesoarqueana da parte norte do Cráton do São Francisco: aspectos geocronológicos e isotópicos / Rafael Gordilho Barbosa. -- 2023.
130 f.
Orientador: Rommulo Vieira Conceição.

Coorientador: Felipe Padilha Leitzke.

Tese (Doutorado) -- Universidade Federal do Rio Grande do Sul, Instituto de Geociências, Programa de Pós-Graduação em Geociências, Porto Alegre, BR-RS, 2023.

1. Evolução Crustal. 2. Paleoarqueano. 3. Mesoarqueano. 4. Cráton do São Francisco. 5. Bloco Uauá. I. Conceição, Rommulo Vieira, orient. II. Leitzke, Felipe Padilha, coorient. III. Título.

Elaborada pelo Sistema de Geração Automática de Ficha Catalográfica da UFRGS com os dados fornecidos pelo(a) autor(a).

DEDICATÓRIA

Esta Tese de Doutorado é dedicada àquela que me fez chegar até aqui e que, desde sempre, está ao meu lado, me dando todo o apoio e incentivo necessários para a conquista dos meus objetivos: minha mãe!

AGRADECIMENTOS

Esta Tese de Doutorado representa o fim de um ciclo, iniciado em meio ao caos da pandemia do COVID-19 e, para que eu pudesse chegar a este momento, muitas pessoas foram importantes ao longo desse período. Não poderia deixar de fazer um agradecimento mais que especial ao meu pai, amigo, geólogo, professor, mestre, exemplo de profissional, Johildo Barbosa, por toda a ajuda neste doutorado. Foram três viagens de campo, fora o apoio na confecção de lâminas e, principalmente, nas discussões geológicas sobre o Cráton do São Francisco ao longo desses 3 anos! Agradeço enormemente aos meus irmãos e padrinhos, Ricardo e Renata por todo o carinho e apoio, bem como aos meus sobrinhos Guga, Bia, Celo (dindo) e Tiago!

Também não poderia deixar de agradecer ao meu orientador, Prof. Rommulo Vieira Conceição por ter aceito o desafio de me orientar e por toda a ajuda dada ao longo do desenvolvimento da Tese. Agradeço ao meu co-orientador, Prof. Felipe Padilha Leitzke por ter sugerido a mudança de tema da Tese, o que me levou a descobrir e me encantar com a evolução crustal arqueana.

Agradeço muito ao professor Carsten Münker, da Universidade de Colônia, Alemanha e a todo o seu grupo pelo apoio incrível que me deram durante o doutorado sanduíche.

Essa Tese não seria possível sem a parceria de Alanielson Ferreira, o Alan, um grande amigo que a geologia me deu e que vou levar comigo pra vida! Obrigado pelas discussões, conversas e ligações, muitas vezes aleatórias. Não poderia deixar de agradecer a Taís Fontes, também parceira dos tempos de pandemia, pelas conversas no LGI. Sem vocês dois aquele período teria sido muito mais difícil.

Não poderia deixar de fazer um agradecimento mais que especial a Joel, motorista das minhas viagens de campo do doutorado. Sua ajuda soi simplesmente espetacular!! Muitíssimo obrigado!

Não poderia deixar de agradecer à minha co-orientanda de iniciação científica, Ísis Cortez, por toda a ajuda que me deu desde que iniciou o projeto. Haja resenha!

Agradeço muito a todos os professores com quem convivi ao longo do período do doutorado e aos meus colegas professores e alunos da UFPEL e da UNEMAT por me mostrarem que estou certo em querer seguir a carreira docente

Agradeço ao Francesco Battista, parceiro de pós-graduação, pelas resenhas e saídas! Elas tornaram todo esse processo mais leve!

Uma tese também tem seus momentos de diversão e eles não seriam possíveis sem a galera do Capone: Maurício, Thiago, Matheus, Nairim, Damiel, Aia. Você são incríveis.

RESUMO

Esta Tese de Doutorado objetiva compreender a evolução crustal eo a mesoarqueana da parte norte do Cráton do São Francisco e quais os mecanismos que operaram neste período do tempo geológico. Para tanto, utilizaram-se sobretudo dados de geoquímica de rocha total, geocronologia U-Pb em zircão, isótopos de Hf, Nd e Sr, bem como de elementos traço em zircão. Verificou-se que os dados isotópicos indicam a predominância de valores negativos de εNd(t) e valores de TDM entre 3,4 e 4,2 Ga para as rochas TTGs do Bloco Gavião, cujas idades variam de 3642 a 3259 Ma, o que sugere retrabalhamento de crosta hadeana a paleoarqueana neste Bloco. Também ocorrem, embora em menor proporção, valores positivos de εNd(t), o que sugere a ocorrência de processos juvenis na região. Neste Bloco, os valores de εHf(t) compilados vão ao encontro dos dados de Nd. Já para os TTGs mesoarqueanos dos Blocos Serrinha e Uauá, cujas idades variam entre 3150 e 2983 Ma, verificou-se uma relativa predominância de valores positivos de εNd(t) e valores de TDM entre 3,0 e 3,3 Ga, o que sugere que a origem destes segmentos crustais está relacionada a processos de natureza juvenil, embora ocorram, também valores negativos associados a retrabalhamento crustal. Especificamente no caso do Bloco Uauá, os novos dados de geocronologia U-Pb obtidos, isto é, as idades de 3320 Ma e 3245 Ma para os zircões ígneos, indicam que ele é cerca de 100 a 150 milhões de anos mais velho do que o que foi previamente mostrado pela literatura. Os dados também permitiram indicar que a origem destas rochas de idade paleoarqueana está associada a um ambiente colisional no qual houve retrabalhamento de uma crosta mais antiga. Também se verificou a ocorrência de um evento metamórfico de idade mesoarqueana (3099 Ma), em condições de fácies granulito, que foi posteriormente retrogradado pro fácies anfibolito em 2989 Ma.

ABSTRACT

This Doctoral Thesis aims to understand the Eo-to-Mesoarchean crustal evolution of the northern part of the São Francisco Craton and which mechanisms operated in this period of geological time. In order to achieve this objective, whole rock geochemical, zircon U-Pb geochronology, isotopes of Hf, Nd and Sr, as well as trace elements in zircon data were used. It was found that the isotopic data indicate a predominance of negative εNd(t) values and TDM values between 3.4 and 4.2 Ga for the TTG rocks of the Gavião Block, whose ages range from 3642 to 3259 Ma, which suggests Hadean to Paleoarchean crustal reworking in this Block. Positive εNd(t) values also occur, although to a lesser extent, suggesting the occurrence of juvenile processes in the region. In this Block, the compiled εHf(t) values match the Nd data. As for the Mesoarchean TTGs of the Serrinha and Uauá Blocks, which ages vary between 3320 and 2983 Ma, there was a relative predominance of positive εNd(t) values and TDM values between 3.0 and 3.3 Ga, which suggests that the origin of these crustal segments is related to processes of a juvenile nature, although negative values associated with crustal reworking also occur. Specifically, in the case of the Uauá Block, the new U-Pb geochronology data obtained, that is, the ages of 3320 Ma and 3245 Ma for the igneous zircons, indicate that it is about 100 to 150 million years older than the that has been previously shown in the literature. The data also allowed us to indicate that the origin of these rocks of Paleoarchean age is associated with a collisional environment in which there was reworking of an older crust. It was also verified the occurrence of a metamorphic event of Mesoarchean age (3099 Ma), in conditions of granulite facies, which was later retrograded to amphibolite facies in 2989 Ma.

LISTA DE FIGURAS

Figura 1. Primeiro estágio da geração de TTGs, segundo o modelo da sagducção. Fonte: Barbosa et al., (2021)..... 14

Figura 2. Segundo estágio de formação de TTGs por sagducção. Fonte: Barbosa et al., (2021)..... 15

Figura 3. Terceiro estágio da formação de TTGs pelo processo da sagducção. Fonte: Barbosa et al., (2021).....15

Figura 4. Quarto estágio da formação de TTGs pelo processo de sagducção. Neste caso, o deslocamento horizontal é necessário para que haja o surgimento do magma TTG, devido ao metassomatismo do mesmo com o peridotito do manto, o que vai formar os sanukitóides e seus correspondentes vulcânicos, os adakitos (SiO_2 > 60%). Fonte: Barbosa et al., (2021).....16

Figura 5. Mapas simplificados mostrando os domos de TTG dos Cratons arqueanos de Yilgarn e Pilbara na Austrália. Verifica-se a presença de TTGs com idades entre 2970 e 2740 Ma para o Cráton Yilgarn e entre 3484 e 3223 Ma para o Cráton Pilbara. Fonte: Barbosa et al., (2020).....16

Figura 6. Mapa geológico simplificado da parte sul do BG indicando a ocorrência de domos de TTG de idades paleo a mesoarqueanas.Fonte: Barbosa et al., (2020)..... 17

Figura 7. Representação esquemática do primeiro estágio da geração de crosta TTG arqueana pelo processo de subducção sub-horizontal.Fonte: Barbosa et al., (2021).....18

Figura 8. Representação do segundo estágio de geração de crosta TTG arqueana pelo processo da subducção sub-horizontal. NM – Nível do mar. Fonte: Barbosa et al., (2021).....19

Figura 9. Modelo esquemático do terceiro estágio da geração de TTGs no Arqueano a partir do mecanismo da subducção sub-horizontal. Notar a geração de TTGs mais novos, além de sanukitóides na base da crosta e adakitos no fundo oceânico. As foliações com baixo mergulho indicam movimentos sub-horizontais das placas. NM – nível do mar. Fonte: Barbosa et al., (2021).....19

Figura 10. Mapa geológico simplificado do Cráton do São Francisco. GB – Bloco Gavião; SB – Bloco Serrinha – UB – Bloco Uauá. Modificado de Gordilho Barbosa et al. (2021)..... 20
Figura 11. Modelos de geração de crosta TTG no BG em três períodos: 3642-3529 Ma, 3403-3378 Ma e 3259-3240 Ma. Fonte: Barbosa et al., (2021).....21

Figura 12. Modelo simplificado da evolução crustal do BG entre o Eo e o Mesoarqueano com as indicações dos TTG1 e TTG2 (rosa), dos metabasaltos de fundo oceânico (verde), das rochas supracrustais (GBs – verde oliva), dos sanukitóides (ST, azul) e dos adakitos (^^, rosa). Fonte: Barbosa et al., (2021) 23

Figura 13. Migmatito do Complexo Santa Luz, Bloco Serrinha. 26

Figura 14. Ortognaisse do Bloco Uauá com foliação de idade arqueana. 27

Figura 15. Dique de basalto toleiitico indeformado (preto) que intercepta o bandamento gnáissico mesoarqueano do Bloco Uauá. 27

Figure 1. Major tectonic compartments of the northern Sao Francisco Craton. C - Contendas rhyolite; ISC - Itabuna-Salvador-Curaca Belt; JB - Jequie Block; M - Mairi Orthogneiss; MN - Mundo Novo rhyolite; RS - Riacho de Santana TTG; SB - Serrinha Block; SV – Sete Voltas TTG; UB - Uaua Block. Modified from Gordilho-Barbosa et al. (2021)…….32

Figure 2. Comparison of the Archaean crustal evolution of Gavião, Serrinha and Uauá Blocks.……36

Figure 3. Field photos. A – Outcrop of the Mairi orthogneiss. In this photo it is possible to observe the 3.64 Ga granodiorite gneiss paleosome and the 3.55 granodiorite gneiss. B – Outcrop of the Riacho de Santana TTG in which the 3.35 Ga orthogneiss with mafic enclaves occur. C – Outcrop of the Sete Voltas TTG containing both the 3.42 Ga tonalite and the 3.14 Ga granitic leucosome. D – Outrcrop photo of the 3.15-2.82 Ga leucodioritic gneiss from the Uauá Block. The small picture is a detail photo of the same rock. E and F – Sete Voltas TTG. In these photos is possible to notice the 3.42 Ga tonalite, the 3.14 Ga leucosome and the biotite-rich reaction selvedges. ……..……37

Figure 4. εNd(t) vs age diagrams for the Archaean blocks of the northern São Francisco Craton. A - Southern Gavião Block, indicating the occurrence of juvenile and crustal reworking processes. B - Northern Gavião Block, suggesting the occurrence of juvenile and crustal reworking processes in two different periods. C - εNd(t) vs age diagram for the 3.42 Ga Sete Voltas TTG, the 3.30 Ga Contendas rhyolite, the 3.17-3.14 Ga Sete Voltas granitic leucosome and the 3.0 Ga tholeiitic rocks from the Contendas-Mirante metavolcanic-sedimentary sequence, suggesting the occurrence of crustal reworking and juvenile processes. D - Western Gavião Block, indicating the occurrence of different periods of crustal reworking and juvenile processes. E - Uauá Block, suggesting two different periods of juvenile and crustal reworking processes. F - Serrinha Block, indicating essentially juvenile processes for the origin of this crustal segment.……42

Figure 5. Sr isotopic data for the Archean São Francisco blocks. A – Rb/Sr vs age diagram for the northern SFC, suggesting high initial Rb/Sr ratios for the 3.30 Ga rhyolitic-granitic systems, a linear enrichment evolution for the 3.45 Ga TTGs and

low initial Rb/Sr ratios for the 3.1-3.0 Ga tholeiitic rocks. B – 87Sr/86Sr(i) vs age diagram for the rocks of the northern SFC. The lower 87Sr/86Sr(i) for the 3.5-3.4 Ga tonalite residue and 3.2-3.0 Ga granodioritic to granitic leucosome may indicate anatexis of the lower crust, while high 87Sr/86Sr(i) in high-Si granitic magmatism suggest partial melting of high K/Na rocks in the upper continental crust……43

Figure 6. Nd and Sr isotopic data for the Sete Voltas complex. A – 87Sr/86Sr(i) vs age diagram indicating that the 3.42 Ga TTG residue has lower 87Sr/86Sr(i) than the 3.17 Ga Sete Voltas granodiorite and the 3.14 Ga Sete Voltas granitic leucosome. B – Rb/Sr vs age diagram showing that the 3.42 Ga TTG residue has lower Rb/Sr ratio than the 3.17 Ga Sete Voltas granodiorite and the 3.14 Ga Sete Voltas granitic leucosome. C - εNd(t) vs age diagram indicating that the 3.42 Ga TTG residue could have been the source of the 3.17 Ga Sete Voltas granodiorite and the 3.14 Ga Sete Voltas granitic leucosome. D – 143Nd/144Nd vs 87Sr/86Sr diagram suggesting that the 3.17 Ga Sete Voltas granodiorite and 3.14 Ga granitic leucosome are derived from the 3.42 Ga Sete Voltas TTG……..….....44

Figure 7. Archaean Hf isotopic data for the northern São Francisco Craton. A - εHf(t) vs age diagram suggesting that the sources of the 3.64 Ga Mairi orthogneiss, in the northern portion of the GB, is associated to reworking of Hadean crust, while the sources of the 3.42 Ga Sete Voltas TTG; 3.30 Ga Contendas and Mundo Novo rhyolites and 3.15 Ga leucodioritic gneiss of the Uauá Block are related to crustal reworking of Palaeo-to-Mesoarchaean crustal sources. The diagram also suggests that the origin of the 3.15-2.80 Ga mafic granulites of the Uauá Block is associated with a Palaeo-to-Mesoarchaean mantle source. B – Detail εHf(t) vs age diagram showing the evolution of the Gavião Block.…… ……46

Figure 8. Juvenile crust and reworking events for the Archaean blocks of the northern São Francisco Craton (data from Supplementary Material 1). A – Sr vs age diagram indicating that the oldest rocks of the northern SFC have higher Sr contents. B – 87Sr/86Sr(i) vs age diagram showing two groups of rocks, which indicate that crustal reworking and juvenile processes occurred in the northern SFC. C – ƐNd(t) vs age diagram showing the crustal evolution processes that occurred in the northern SFC. D - ƐNd(t) vs 87Sr/86Sr(i) diagram indicating that the crustal evolution of the northern SFC is related to juvenile and crustal reworking processes.……47

Figure 9. Hf isotope data. A – ƐHf(t) vs age diagram showing that the crustal evolution of the northern São Francisco Craton had similarities with that of Kaapvaal, Pilbara and Zimbabwe cratons. This suggests that similar processes occurred in different portions of the early Archaean crust. The data from Kaapvaal and Pilbara cratons were compiled from Gardiner et al. (2021) and the data from Zimbabwe craton were compiled from Hofmann et al. (2022). Crust values of 0.0113

and 0.005 from Bouvier et al. (2008). DM trend from Vervoort and Blichert-Toft (1999) and Vervoort et al. (2017). B – Histogram indicating the distribution of the TDM(Hf) data of the northern São Francisco Craton……49

Artigo 2

Figure 1. Simplified geological map of the northern part of the São Francisco Craton. GB – Gavião Block; JB – Jequié Block; ISC – Itabuna-Salvador-Curaçá Block; SB – Serrinha Block; UB – Uauá Block. Modified from Gordilho-Barbosa et al. (2023)…….57

Figure 2. Field and petrography aspects of the Paleoarchean gneiss of the Uauá Block. A - Outcrop photograph from the migmatite-gneiss showing the hornblende granodioritic residue and the opx-cpx granitic leucosome. B – Outcrop photograph showing the 2.7-2.6 Ga tholeiitic dyke cutting the migmatite-gneiss banding. C – Hand specimen of the migmatite-gneiss, showing the residue and the leucosome. D – Photomicrograph of the Pl+Hbl residue of the migmatite-gneiss in plane-polarized light. E – Photomicrograph of the Cpx + Pl leucosome. F – Photomicrograph of the Opx + Pl leucosome. Abbreviations of the minerals' names after Whitney and Evans (2010)……..58

Figure 3. Geochemical characteristics of the Paleoarchaean Uauá Block migmatite-gneiss. A – Ternary K-Na-Ca diagram showing the calc-alkaline (CA) and trondhjemite (Tdh) trends from Barker and Arth (1976) and the field of Archean TTGs from Martin et al. (2005). B – Ternary (Ba+Sr)/1000-1/Er-Er diagram to distinguish between TTGs and sanukitoids (after Heilimo et al., 2010). C – Sr vs Y diagram to discriminate the TTG types between high, medium, and low pressure (HP, MP and LP – after Moyen, 2011). D – Sr/Y vs La/Yb plot also distinguishing the TTGs as HP, MP and LP (Moyen, 2011). E – Primitive-mantle normalized (Palme and O'Neill, 2014) trace elements diagram for the Uauá Block migmatite-gneiss compared to high, medium and low HREE TTGs (after Moyen, 2011). F – Chondrite-normalized (Palme and O'Neill, 2014) REE diagram for the Uauá Block migmatite-gneiss compared to high, medium and low HREE TTG types (after Moyen, 2011)…….60

Figure 4. Zircon U -Pb ages for the Paleoarchaean Uauá Block migmatite-gneiss. A – LA-ICP-MS results showing all the obtained data. B – Concordia diagram showing the most concordant age data for the UB migmatite-gneiss. C – LA-ICP-MS results for the oldest age cluster. D – LA-ICP-MS results and Concordia age

for the second older age cluster. E – LA-ICP-MS results and Concordia age for the third age cluster. F – LA-ICP-MS results for the youngest age cluster……62

Figure 5. Lu-Hf isotopes and zircon trace elements diagrams for the migmatite-gneiss of the Uauá Block. A – εHf(t) vs age diagram for the UB migmatite-gneiss. The blue dots represent the Archaean zircons data compiled from Maltese et al. (2021). DM – depleted mantle; CHUR – Chondritic Uniform Reservoir (chondritic mantle). B – Chondrite-normalized REE patterns (Palme and O'Neill, 2014) of zircons from the Uauá Block orthogneiss. Both groups (magmatic and metamorphic) have positive Ce and negative Eu anomalies. The grey field represents the pattern of the continental crust defined by Grimes et al. (2007). C-F – Binary zircon trace elements diagrams showing that the magmatic zircons have La/Lu ratio < 0.1 and smaller concentrations of trace elements than the metamorphic ones…….64

Figure 6. Binary diagrams. A – Time composition diagram for the Palaeoarchaean Uauá Block migmatite-gneiss showing the TTG types of Moyen and Laurent (2018). LP – low pressure TTG, MP – médium pressure TTG, HP – high pressure TTG. B – Nb/Hf vs Th/U diagram showing that most of the zircons from the Uauá Block migmatite-gneiss are related to orogenic settings, suggesting the occurence of collisional tectonics within the UB since the Palaeoarchaean……69

LISTA DE ABREVIAÇÕES

BG – Bloco Gavião

BS – Bloco Serrinha

BU – Bloco Uauá

CSF – Cráton do São Francisco

GB – *Greenstone Belt*

OISC – Orógeno Itabuna-Salvador-Curaçá

SMVS – Sequência Metavulcanossedimentar

SUMÁRIO

Lista de Figuras .....

Lista de abreviações 9

1. Introdução.....11
2. Aspectos Geológicos do Eo a Mesoarqueano.....12
   - 2.1. Considerações Iniciais.....12
   - 2.2. Bloco Gavião 20
   - 2.3. Bloco Serrinha.....24
   - 2.4. Bloco Uauá.....26
3. Artigo 1: A review of 3.66 to 2.77 Ga crustal differentiation in the northern São Francisco Craton, Brazil.....28
   - 3.1. Introduction.....30
   - 3.2. Data Compilation 31
   - 3.3. Geological Background 32
   - 3.4. Results and data evaluation 37
   - 3.5. Discussion.....40
   - 3.6. Conclusion.....49
4. Artigo 2: Palaeoarchaean crustal formation in the Uauá Block, northern São Francisco Craton, Brazil: evidence for 3.3 to 3.0 Ga collisional tectonics…..51
   - 4.1. Introduction…….55
   - 4.2. Geological setting and field relations……..55
   - 4.3. Results…….57
   - 4.4. Discussion……65
   - 4.5. Conclusions……..69
5. Conclusão.....71
6. Referências.....73
7. Apêndices.....86

1. Introdução

A antiga e relativamente estável Plataforma Sul Americana é uma parte do núcleo pré-cambriano que escapou dos efeitos da orogênese andina. Por sua vez, os crátons da América do Sul correspondem às porções internas de placas que fizeram parte do *West Gondwana*. São terrenos do continente que atingiram e mantiveram sua estabilidade tectônica pelo menos desde o início do Fanerozoico (Alkmim et al.,1993), que apresentam quilhas espessas e baixo fluxo de calor.

Entre os crátons da América do Sul destaca-se o Cráton do São Francisco (CSF) definido como um segmento crustal não atingido de forma significativa pelos processos neoproterozóicos, incluindo colisões, deformações e metamorfismos. (Almeida et al., 1981). Este representa, desse modo, um relicto da litosfera que preserva substancial parte da memória da Terra.

A parte norte do CSF, quase toda dentro do Estado da Bahia, tem seu alicerce no Paleo e Mesoarqueano constituído basicamente por três segmentos crustais arqueanos mais importantes: o Bloco Gavião (BG),o Bloco Serrinha (BS) e o Bloco Uauá (BU). Antes do Neoarqueano, os dados geológicos, sobretudo os isotópicos, indicam que eles possivelmente formavam um bloco único (Barbosa et al., 2021).

A separação destes blocos ocorreu possivelmente no final do Mesoarqueano deixando uma ampla zona de direção meridiana, que foi preenchida por rochas neoarqueanas. Por sua vez, a colisão que novamente uniu esses blocos teve início no Neoarqueano entre 2,6-2,7 Ga, tendo continuidade no Paleoproterozoico, no período entre 2080-2000 Ma. Essa colisão deu origem ao Orógeno Itabuna-Salvador-Curaçá (OISC) o qual possui eixo que se distribui na parte leste do CSF na Bahia, também de direção próxima à N-S. A colagem ou colisão do BG e BS/BU gerou importante cadeia de montanhas que, embora atualmente erodida, deixou expostas e relativamente bem preservadas suas raízes, deformadas e metamorfisadas em alto e médio grau (Barbosa e Sabaté, 2002; 2004).

Esta monografia visa, então, apresentar os aspectos geotectônicos do Arqueano, bem como caracterizar as unidades geológicas da parte norte do Cráton do São Francisco aonde afloram as rochas de idade eo a mesoarqueana. Este trabalho também objetiva propor, com base na revisão sistemática da

literatura, quais foram, do ponto de vista isotópico, os possíveis processos que contribuíram para a evolução crustal eo a mesoarqueana da região.

2. Aspectos Geológicos do Eo a Mesoarqueano da parte norte do Cráton São Francisco

2.1. Considerações Iniciais

Considera-se que a Terra é o único planeta no sistema solar que possui uma crosta continental bem desenvolvida, com características essencialmente félsicas. Admite-se que esse material félsico foi sendo progressivamente extraído do Manto a partir dos últimos 4,2 ou 4,4 Ga (Wilde et al., 2001;Iizuka et al., 2006).

A crosta continental atual, contém cerca de 70% dos elementos altamente incompatíveis, que foram sendo progressivamente depletados e dirigidos para partes mais superficiais da Terra (Rudnick e Fountain, 1995; Rollinson, 2007). Segundo esses autores, a crosta se desenvolveu a partir da associação de ambientes de arcos de ilhas e margens destrutivas. Nesses locais, nas partes mais profundas ocorreu a fusão parcial do manto, levando à produção de basalto, principal resultado dessa fusão. Por sua vez, através da subducção, as margens destrutivas foram também zonas onde o material crustal, erodido e reciclado, introduziu sedimentos na cunha mantélica (Iizuka et al., 2006) Por sua vez, os estudos experimentais e geoquímicos realizados por Martin et al. (2010) mostraram que esses magmas TTG foram formados a partir da fusão parcial dos basaltos hidratados que entraram em subducção. Os TTGs resultantes da fusão dos basaltos hidratados interagiram e se metassomatizaram com a cunha do Manto e, na subida em direção à crosta, formaram os sanukitóides, em profundidade, e rochas vulcânicas adakíticas, na superfície. Um complemento da produção do magma TTG foi a formação de um resíduo eclogítico que retornou para o Manto durante os processos de subducção.

Sendo assim, a composição média da crosta continental é andesítica-granítica, fortemente enriquecida em elementos incompatíveis como indicado antes. Entretanto, pergunta-se: porque ela não é basáltica? Nos arcos vulcânicos modernos, o principal fluxo de magma entre a crosta e o manto é basáltico e não andesítico. Para explicar esse paradoxo sugere-se: (i) que houve a delaminação

da crosta inferior onde o material ultramáfico, produtor de basalto, é removido constantemente das raízes dos continentes retornando ao Manto, ou (ii) que a composição dos continentes foi sendo modificada pelo intemperismo e pela seletiva reciclagem dos elementos químicos, tornando-a mais félsica (Wilde et al., 2001) Contudo ainda hoje existem dificuldades para se entender ambos os modelos. Assim, alternativamente, admite-se que, ao longo do tempo, houve a mudança da composição da crosta em direção ao andesito, devido à interação entre o magma basáltico e o magma TTG durante o Arqueano (Moyen e Martin, 2012). Isso implica que a crosta continental arqueana foi criada através da subducção e da tectônica de placas, que teriam operado desde os primórdios da Terra.

Outras evidencias vêm sugerir também que, embora a crosta inicial tenha sido básica, ela foi se transformando em crosta continental andesítica-granítica e, que há pelo menos 4,35 Ga já existia crosta continental desse tipo, segundo as idades obtidas em zircões hadeanos (Wilde et al., 2001; Iizuka et al., 2006).

Segundo Martin et al. (2010), esta crosta inicial teria sido basáltica e os primeiros TTGs, constituintes da crosta continental, seriam produtos da fusão desses basaltos. Por outro lado, essa crosta inicial possuía também komatiitos, embora esses representassem apenas 10-20% das lavas, em comparação com as lavas basálticas toleiíticas, que foram de 50-80% (Martin et al., 2010). Os komatiítos não participaram da geração dos TTG visto que para fundir komatiítos as temperaturas requeridas teriam que ser muito mais altas que aquelas dos basaltos, os quais fundiram primeiro. Sendo assim é provável que os komatiítos, muito mais densos, a maioria deles tenham retornado ao Manto pela gravidade, não tendo assim, participado do crescimento da crosta (Martin et al., 2010)

Vale ressaltar que na crosta continental do BG são encontradas rochas portadoras de zircões detríticos datados em 4,1 Ga (Paquette et al., 2015) e, com a maioria dos TTG apresentando valores de εNd(t) negativos (Gordilho Barbosa et al., 2021 – em preparação). Isso sugere que esses TTG são resultantes de retrabalhamento de crosta hadeana/eoarqueana (ver artigo de revisão, Gordilho Barbosa et al.,2023) e com idades pelo menos mais antigas que 4,1 Ga. Também ocorrem valores de εNd(t) positivos, que sugerem a derivação de processos juvenis. Trabalhos de Kearey et al., (2009) e Nebel et al., (2018) apresentam tentativas de explicar a geração da crosta continental arqueana. Baseado nos modelos propostos, Barbosa et al. (2020) propuseram uma alternativa para explicar a formação da crosta continental do BG, inclusive fazendo comparações com outros cratons de similaridades geológicas e geocronológicas, como, por

exemplo, Yilgarn e Pilbara, na Austrália.)

Geralmente a crosta do BG é constituída por terrenos TTG, de alto e médio graus metamórficos, mas que englobam GB e sequências metavulcanossedimentares (SMVS), esses últimos da fácies xisto verde ou anfibolito baixo. Sua origem pode ser considerada através de duas hipóteses: (i) através da sagducção (tectônica vertical) ou (ii) através da tectônica de placas (tectônica sub-horizontal), a mais provável.

O modelo de sagducção, conforme as interpretações de Nebel et al. (2018) e Kearey et al. (2009), considera a existência de quatro estágios para a formação da crosta continental inicial. No primeiro estágio, com a duração de cerca de 200 Ma, ocorre fusão da crosta basáltica (~4,0 Ga) sobre a astenosfera indiferenciada, associada à deposição de rochas supracrustais em uma protoplaca (futuras sequências metavulcanossedimentares e greenstone belts? (Fig. 1)

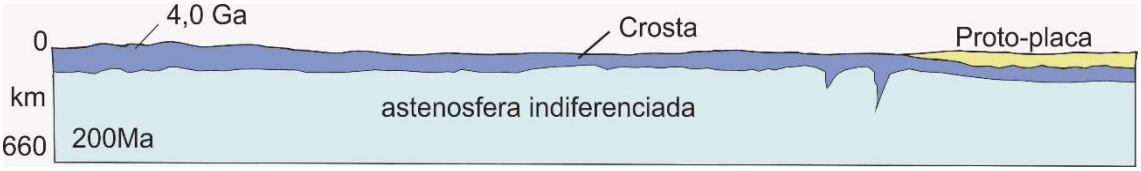

Figura 1 – Primeiro estágio da geração de TTGs, segundo o modelo da sagducção. Fonte: Barbosa et al., (2021).

Posteriormente, ocorre convecção do manto e sagducção mais pronunciada com fusão do material que mergulha incluindo a formação de plutonitos tipo TTG, em uma profundidade de cerca de 250 km (Fig. 2).

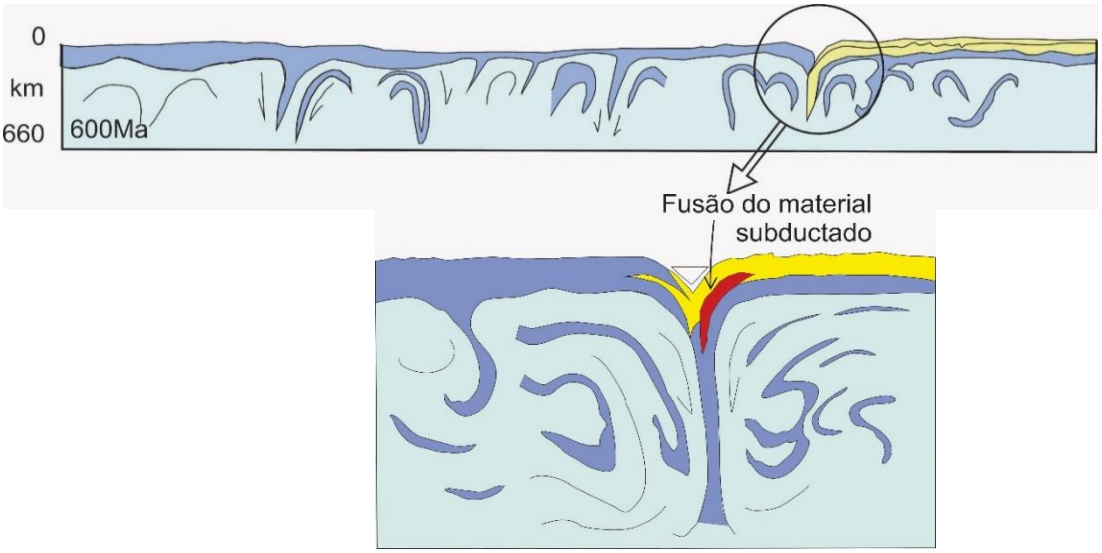

Figura 2 – Segundo estágio de formação de TTGs por sagducção. Fonte: Barbosa et al., (2021).

No terceiro estágio, verifica-se o mergulho da crosta inferior com fusão parcial do manto e formação de TTG devido à convecção. A pluma “erode” a litosfera, com o aparecimento de intrusões acamadadas e lavas komatiíticas Antigos TTGs (baixa razão La/Yb e baixo Sr) se formaram em níveis mais rasos e na presença de plagioclásio. Novos TTGs (alta razão La/Yb e alto Sr) aparecem em níveis mais profundos e na presença de granada (Fig. 3).

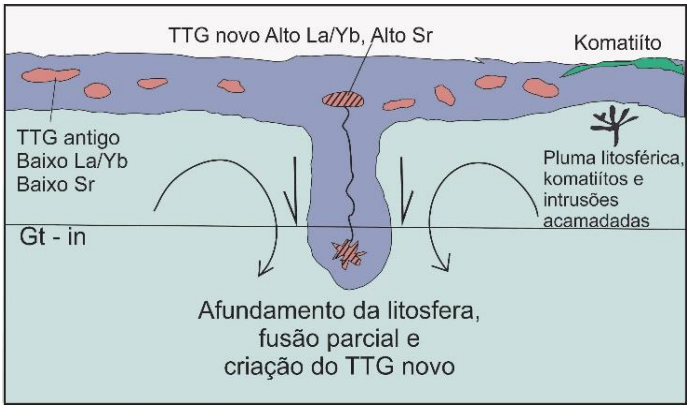

Figura 3 – Terceiro estágio da formação de TTGs pelo processo da sagducção. Fonte: Barbosa et al., (2021).

Por fim, no quarto e último estágio, o material TTG fundido penetra no peridotito do manto formando sanukitoides plutônicos e seus correspondentes vulcânicos adakíticos (SiO_2>60%) (Fig. 4).

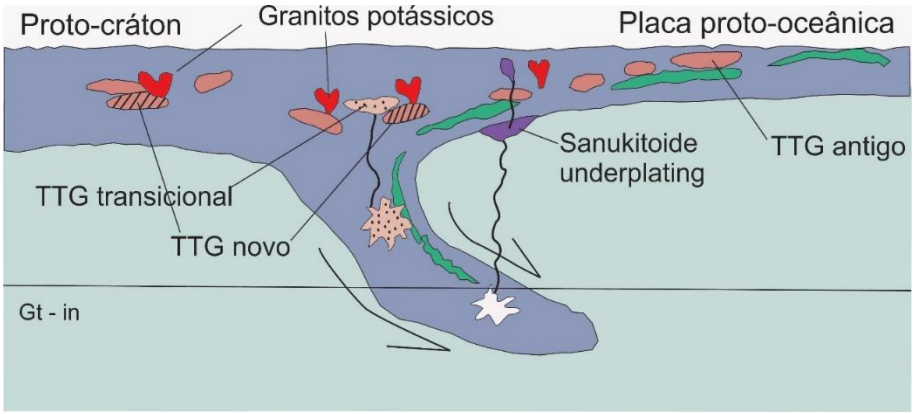

Figura 4 – Quarto estágio da formação de TTGs pelo processo de sagducção. Neste caso, o deslocamento horizontal é necessário para que haja o surgimento do magma TTG, devido ao metassomatismo do mesmo com o peridotito do manto, o que vai formar os sanukitóides e seus correspondentes vulcânicos, os adakitos (SiO_2 > 60%). Fonte: Barbosa et al., (2021).

Verifica-se nos Crátons de Yilgarn e Pilbara, na Austrália, a ocorrência de domos de TTG antigos (2970-2760 e 3484-3462 Ma, respectivamente), rodeados por grandes volumes de TTG mais novos (2760-2740 e 3324-3277 Ma, respectivamente)(Kearey et al., 2009; Nebel et al., 2018). Em ambos os casos ocorrem granitoides (2640 e 2851 Ma) com teores de potássio mais elevados, além de pequenos volumes de sanukitoides (2747 Ma, Cráton Yilgarn), os quais, segundo Nebel et al. (2018), estão também presentes nas margens dos domos (Fig. 5).

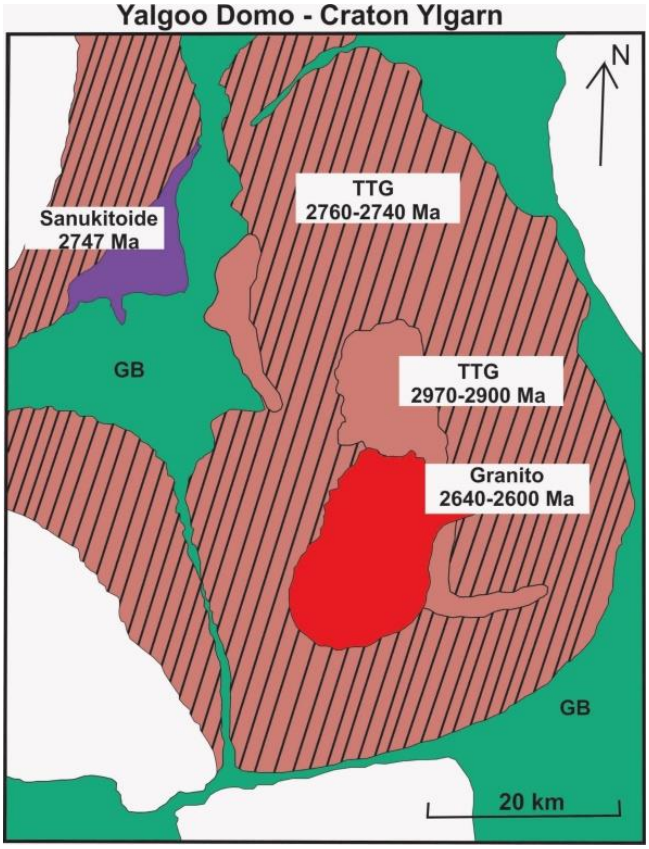

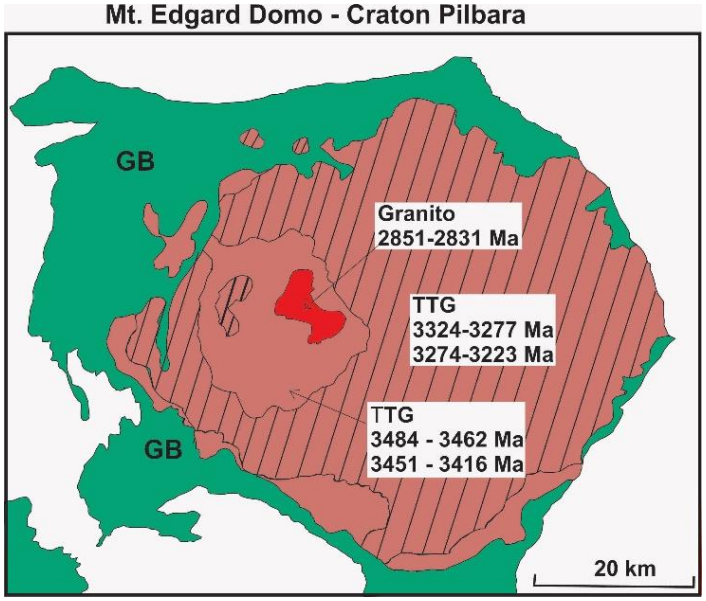

Figura 5 – Mapas simplificados mostrando os domos de TTG dos Cratons arqueanos de Yilgarn e Pilbara na Austrália. Verifica-se a presença de TTGs com idades entre 2970 e 2740 Ma para o Cráton Yilgarn e entre 3484 e 3223 Ma para o Cráton Pilbara. Fonte: Barbosa et al., (2020).

No caso do BG, em sua parte sul, percebe-se um padrão similar ao que foi observado nos crátons australianos anteriormente mencionados. Verifica-se a presença de TTGs antigos (3403-3259 Ma), TTGs mais novos (3378-3158 Ma), ambos paleo a mesoarqueanos, além de granitóides ricos em potássio (2711-2652 Ma). Assim como no Cráton Pilbara, ainda não foram encontrados sanukitoides no BG (Fig. 6).

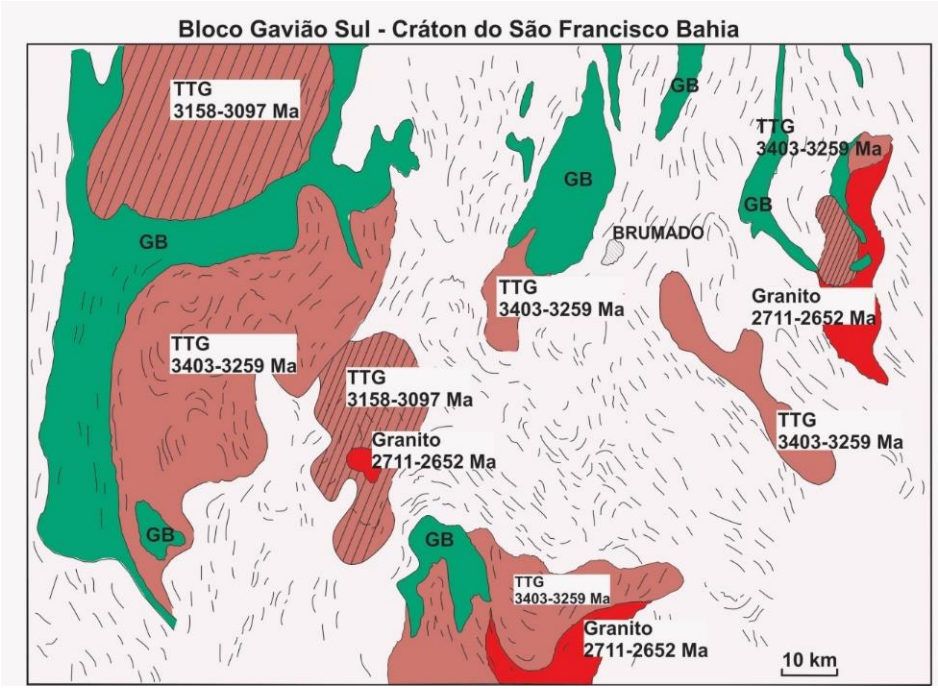

Figura 6 – Mapa geológico simplificado da parte sul do BG indicando a ocorrência de domos de TTG de idades paleo a mesoarqueanas. Fonte: Barbosa et al., (2020).

Modelos tectônicos atuais indicam que o crescimento da crosta foi progressivo, embora episódico, com variados períodos de intenso e rápido crescimento (referência). Entende-se que esse processo aconteceu sobretudo no Arqueano, a partir da crosta oceânica basáltica-komatiitica vinda do manto litosférico (εNd_t positivo) e onde o principal magma resultante foi rico em Si e Na, sendo o responsável pela geração das primeiras associações primitivas do tipo tonalito-trondhjemito-granodiorito (TTG) (εNd_t negativo). Assim, pequenas áreas de crosta continental TTG surgiram nesse “Mar de Basaltos e Komatiitos” desde pelo menos 4,35 Ga (Moyen e Martin, 2012),. Esta crosta inicial deve ter sido reciclada formando pequenas áreas de crosta continental com rochas

andesíticas, associadas a lavas basálticas tholeiíticas e komatiitos todas com εNd(t) negativo. Novos TTGs com idades mais novas que 4,35 Ga apareceram progressivamente ao longo do tempo geológico.

Outro modelo utilizado para explicar a gênese dos TTGs foi o da tectônica sub-horizontal. Os trabalhos de Martin et al. (2010) e Moyen e Martin (2012) sugerem a formação da crosta TTG arqueana em três estágios. No primeiro estágio, considera-se a presença do já mencionado “Mar de Basaltos e Komatiítos” que, durante o seu resfriamento possibilitou a ocorrência de processos primitivos de subducção, conforme esquematizado na figura 7.

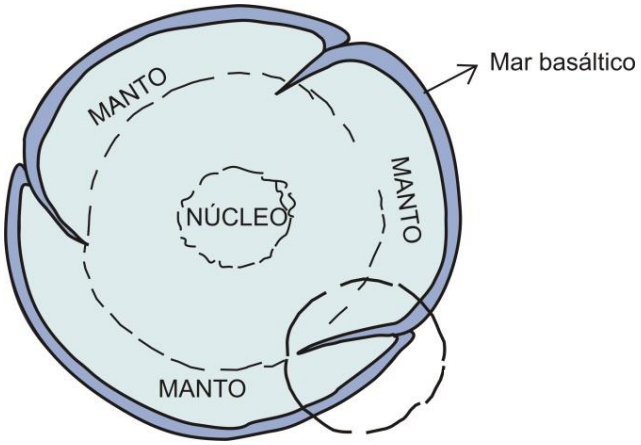

Figura 7 – Representação esquemática do primeiro estágio da geração de crosta TTG arqueana pelo processo de subducção sub-horizontal. Fonte: Barbosa et al., 2021.

No segundo estágio, admite-se que a crosta basáltica primitiva, mais fria e parcialmente solidificada, subductou no manto litosférico, mais quente, tendo daí sofrido refusão e depleção de elementos incompatíveis, gerando os tonalitos primitivos. Estes, através da diferenciação magmática vieram a produzir plútons TTG, em profundidade, e os primeiros adakitos (rochas vulcânicas, ricas em Na, com SiO_2 <60%) no fundo do mar. Com a continuidade do processo de subducção, o magma TTG, ao subir para partes mais superficiais, fundiu a placa litosférica, produzindo plutons sanukitóides profundos (granitóides arqueanos com alto-Mg, encontrado em margens convergentes) além das vulcânicas adakíticas (SiO_2 >60%), também no fundo do mar (Fig. 8).

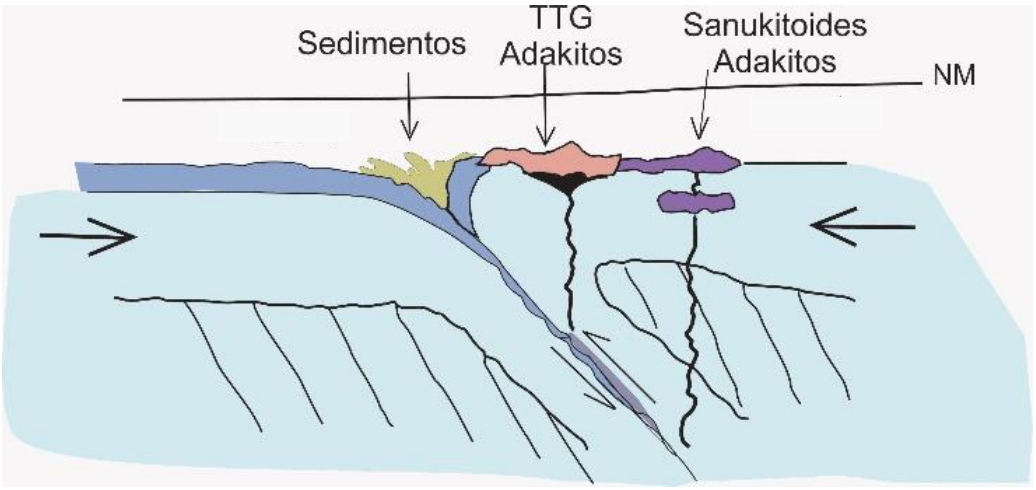

Figura 8 – Representação do segundo estágio de geração de crosta TTG arqueana pelo processo da subducção sub-horizontal. NM – Nível do mar. Fonte: Barbosa et al., 2021.

No terceiro estágio ocorre a colisão de protoplacas continentais e a formação de TTGs mais novos, além de plútons sanukitóides e vulcânicas adakíticas (SiO_2 >60%) no fundo do oceano. Conforme apresentado na figura 9, em função da colisão, a deformação resultante produziu nas rochas, planos penetrativos sub-horizontais, fato que vem a sugerir a presença de placas tectônicas no Arqueano.

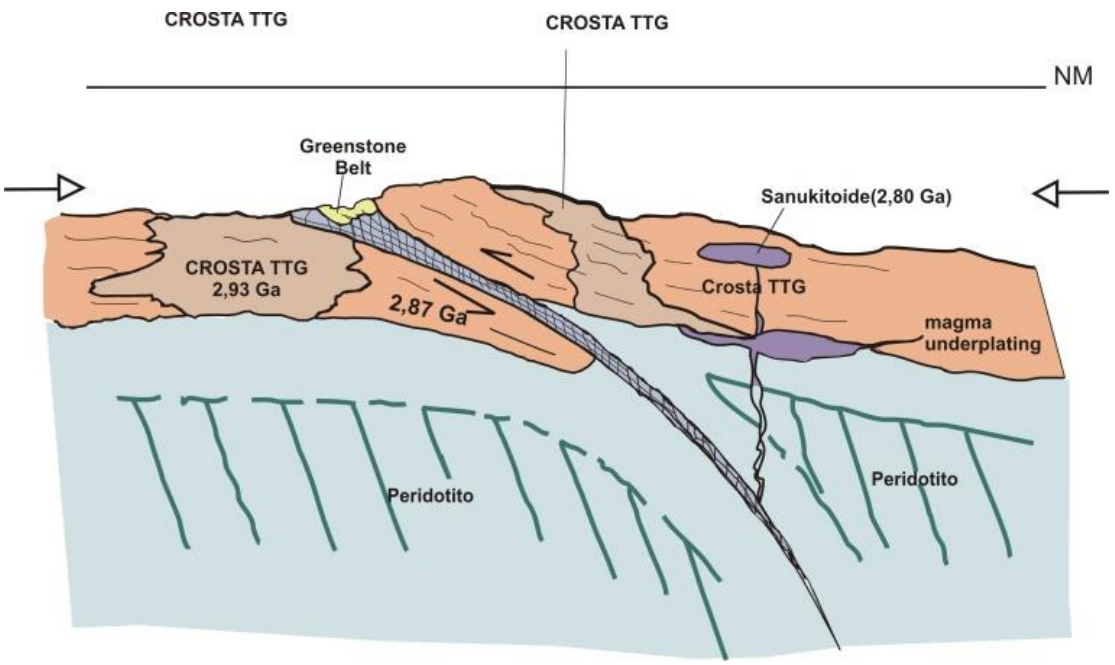

Figura 9 – Modelo esquemático do terceiro estágio da geração de TTGs no Arqueano a partir do mecanismo da subducção sub-horizontal. Notar a geração de TTGs mais novos, além de sanukitóides na base da crosta e adakitos no fundo oceânico. As foliações com baixo mergulho indicam movimentos sub-horizontais das placas. NM – nível do mar. Fonte: Barbosa et al., 2021.

As evidências geológicas mostradas nos próximos itens permitiram a consideração de que na parte norte do CSF predominou a tectônica de placas, sobretudo em função da presença nas rochas estudadas de deformações

(foliação/bandamentos sub-horizontais). Com os dados atualmente disponíveis, é proposta a seguir a evolução crustal do CSF setentrional, levando em conta dados geocronológicos e isotópicos.

2.2. Bloco Gavião (BG)

O BG como um todo (Fig. 10), foi formado essencialmente no Paleo e no Mesoarqueano, sendo considerado um exemplar da crosta continental mais antiga do CSF na Bahia. Esta crosta é constituída por terrenos TTGs, de alto e médio graus metamórficos, mas que englobam, de forma isolada, GB e SMVS, esses últimos dos fácies anfibolito baixo e xisto verde.

Admite-se que as rochas TTGs do BG foram nucleadas pela subducção de crosta oceânica, ou de platôs e arcos de ilhas, hidratadas (Martin et al., 2010; Moyen e Martin, 2012). Considera-se que isso ocorreu, no mínimo, em três etapas, conforme as idades obtidas nestes TTGs, ou seja: 3642-3529 Ma (Oliveira et al., 2020; Werlang, 2019), 3403-3378 (Bastos Leal et al., 2003) e 3259-3240 Ma (Santos Pinto et al., 2012), todas essas idades U-Pb em zircão (Fig. 11).

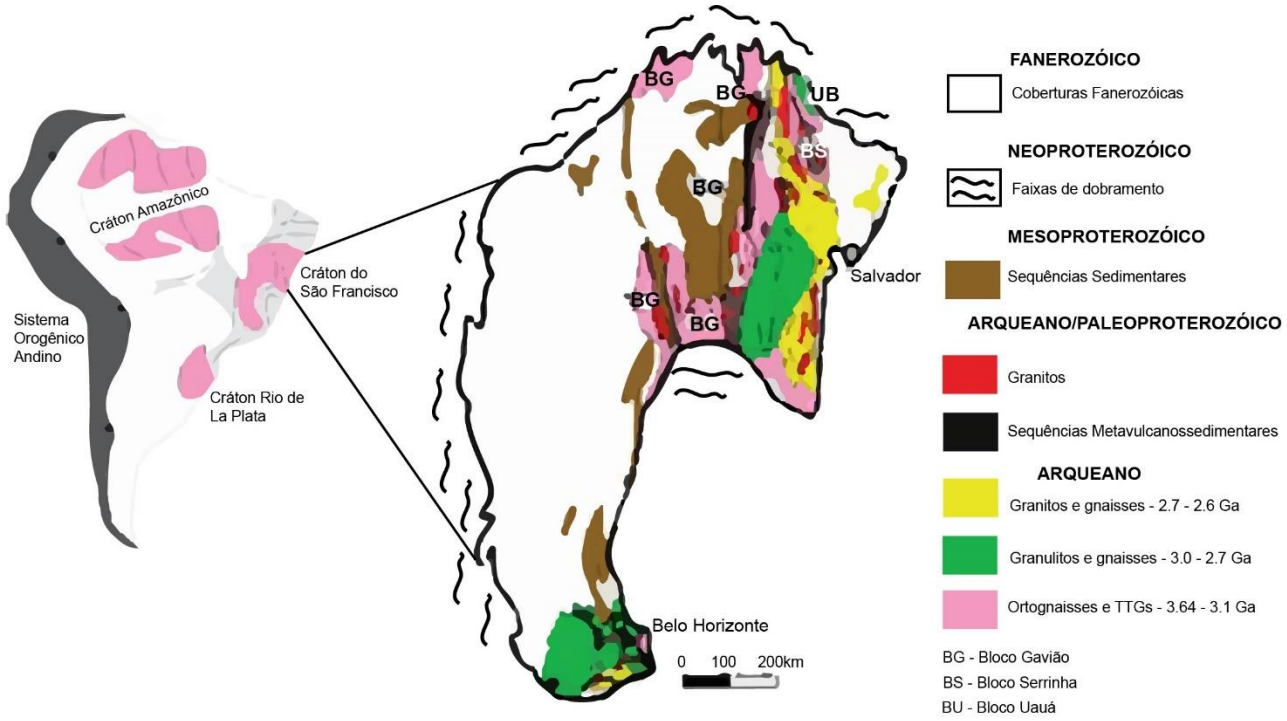

Figura 10 - Mapa geológico simplificado do Cráton do São Francisco. BG – Bloco Gavião; BS – Bloco Serrinha – BU – Bloco Uauá. Modificado de Gordilho Barbosa et al. (2021).

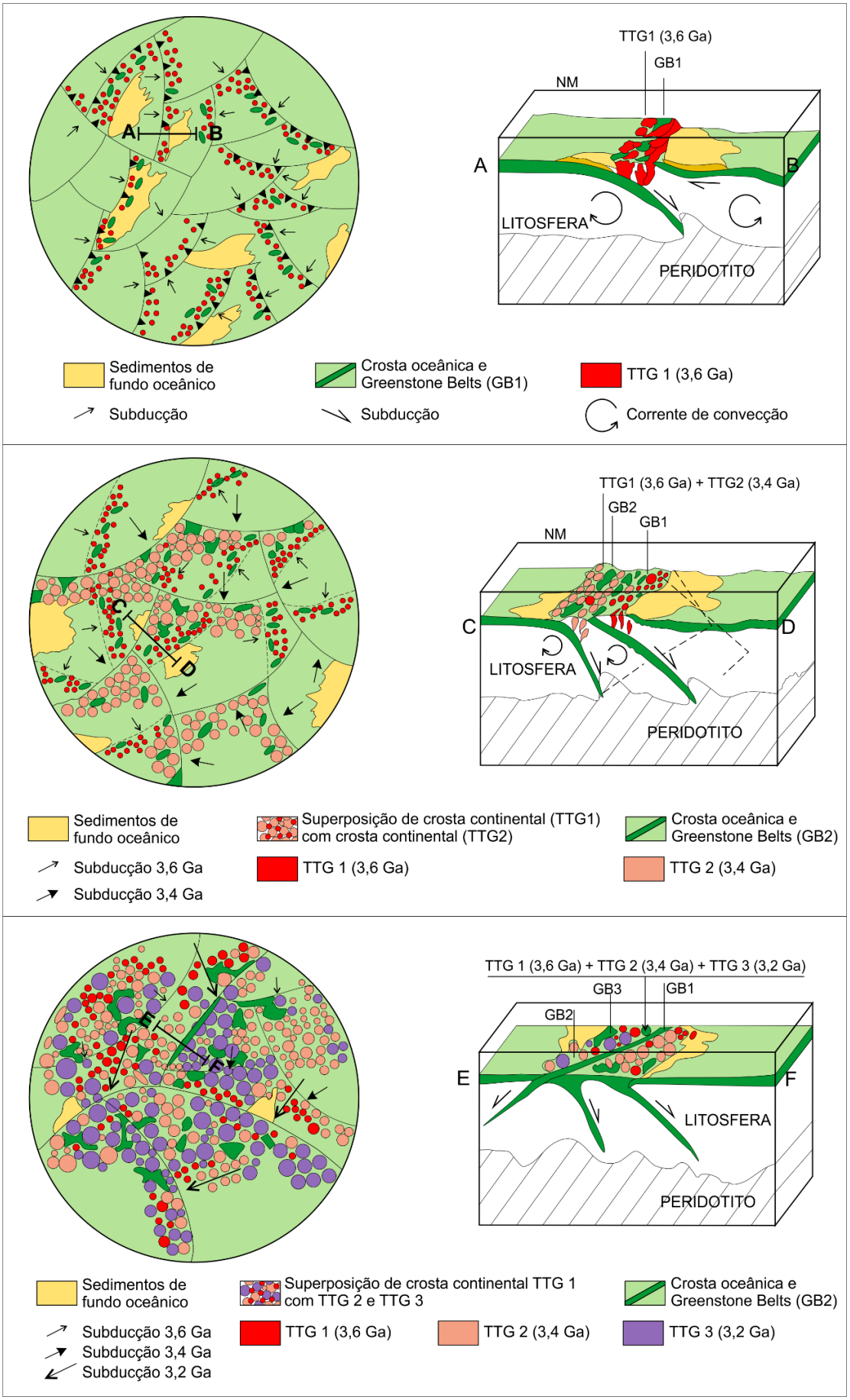

Figura 11 – Modelos de geração de crosta TTG no BG em três períodos: 3642-3529 Ma, 3403-3378 Ma e 3259-3240 Ma. Fonte: Barbosa et al., 2021.

Na primeira etapa (3642-3529 Ma, Oliveira et al., 2020; Werlang, 2019) as crostas oceânicas eram muito quentes e, ao se resfriarem, possibilitaram que partes mais frias, portanto mais pesadas, afundassem em relação às partes mais quentes (Martin et al., 2010; Moyen e Martin, 2012). Admite-se que, cobertas por água (Figs. 8, 11), foi construído na primeira etapa, um mosaico entre as protocrostas oceânicas e seus respectivos sedimentos de fundo. A figura 11 e o bloco diagrama correspondente à seção A-B, exemplifica as primeiras zonas de subducção, que geraram, através da fusão das crostas basálticas tholeiíticas hidratadas, os primeiros TTGs e GBs (TTG1 e GB1), sempre associados. Esses GBs provavelmente correspondem aos representantes das vulcânicas e sedimentos de fundo, em baixo grau. Elas passaram a constituir os *greenstone belts* e/ou as sequências metavulcanossedimentares que resistiram nas partes não subductadas. Essas foram penetradas ao mesmo tempo pelos plutons TTG1 provenientes de partes mais profundas da litosfera (Fig. 11). Na segunda etapa (3403-3378 Ma, Bastos Leal et al., 2003), devido ao resfriamento progressivo do planeta durante o Arqueano, movimentos das correntes de convecção continuaram atuando e promovendo novo quebramento da crosta inicial, incluindo as partes anteriormente subductadas. A figura 11 e o bloco diagrama correspondente à seção C-D, exemplificam o segundo conjunto de subducções ocorrido no intervalo de aproximadamente 200 milhões de anos, em relação ao primeiro.

Surgiram, desse modo, porções de crostas periféricas, mais extensas que as primeiras, constituídas pelos respectivos TTG2 e GB2. Esses foram, também, provenientes da fusão das crostas oceânicas e, talvez, da reciclagem dos TTG1. Como mostra a figura 11 e o bloco diagrama C-D, foram criadas faixas de rochas, com a predominância de plútons TTG1 (3642-3529 Ma) e TTG2 (3403-3378 Ma), com os mais novos penetrando os mais velhos, em alguns casos. Os GB1 e os GB2 também estão presentes nessa nova configuração. Após cerca de 150 milhões de anos, ocorreu a terceira etapa de geração de crosta TTG arqueana no BG (3259-3240 Ma, Santos Pinto et al., 2012). Neste caso, interpreta-se o surgimento de uma nova crosta continental composta por TTG1 (3642-3529 Ma), TTG2 (3403-3378 Ma) e TTG3 (3259-3240 Ma) associados aos GB1, GB2 e GB3. Assim na figura 11 a crosta paleo e mesoarqueana parece ser semelhante à atual.

Durante essas três etapas, devido à ocorrência de basaltos hidratados no fundo dos oceanos, supõe-se que exista água no ambiente desde o paleo e

mesoarqueano, o que pode ser comprovado pela presença metabasaltos de fundo oceânico com estrutura de pillow lavas (Teles, 2013), no lado leste da Serra de Jacobina e, também, no GB Umburanas, representante do GB3 (vulcânicas félsicas, 3147 Ma, intercaladas com basaltos toleiíticos de fundo oceânico) (Bastos Leal et al., 2003). Neste, ocorrem komatiitos com textura *spinifex*, que se cristalizaram no denominado Mar Jacobina-Umburanas (Barbosa et al., 2020). O bloco diagrama da figura 12 representa um modelo que indica as etapas de construção das primeiras crostas continentais no BG.

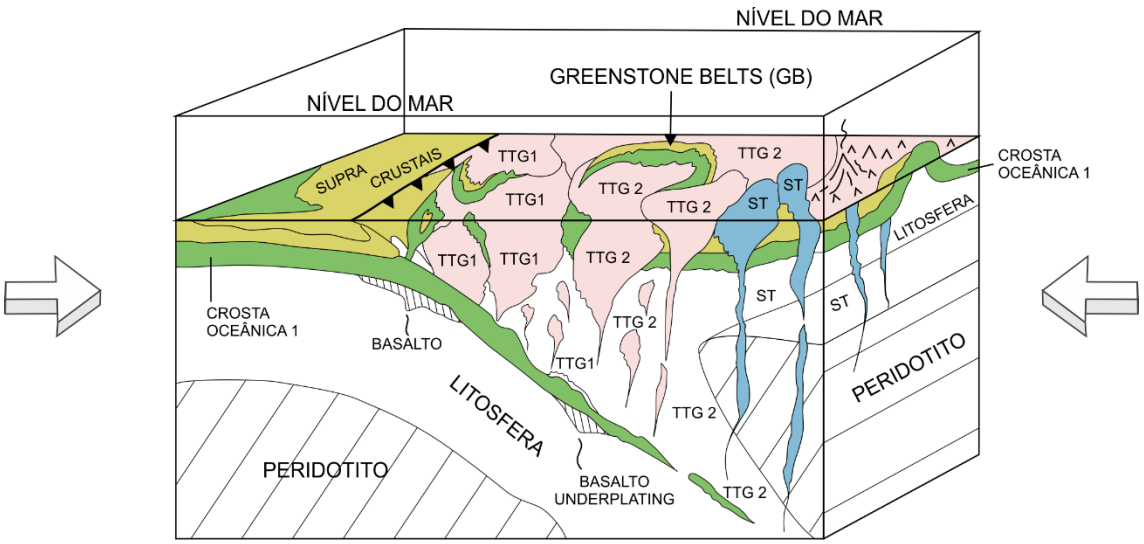

Figura 12 – Modelo simplificado da evolução crustal do BG entre o Eo e o Mesoarqueano com as indicações dos TTG1 e TTG2 (rosa), dos metabasaltos de fundo oceânico (verde), das rochas supracrustais (GBs – verde oliva), dos sanukitóides (ST, azul) e dos adakitos (^^, rosa). Fonte: Barbosa et al., 2021.

Para uma melhor compreensão da origem do BG, optou-se por subdividi-lo em: (i) Bloco Gavião Oeste; (ii) Bloco Gavião Sul e (iii) Bloco Gavião Norte. Vale ressaltar que essa divisão é estritamente geográfica pois, como o BG representa a quase totalidade da parte norte do CSF (Fig. 10), ela facilita a localização do leitor dentro do Bloco. Importante, também, salientar que os dados isotópicos mostrados no artigo incluso neste volume indicam que, ao menos no Arqueano, não é possível dividir geologicamente os diferentes segmentos do BG.

2.2.1. Bloco Gavião Oeste

A parte oeste do BG é composta por rochas Paleo a Neoarqueanas que são intrudidas pelo Batólito Guanambi, de idade Paleoproterozóica, e rochas coetâneas (Barbosa et al., 2012). De acordo com Barbosa et al. (2020), a porção oeste do BG foi acrescida ao BG Sul ao longo do lineamento Igaporã, durante o Paleoproterozóico. Baseado em observações de campo, geocornológicas,

metamórficas e petrogenéticas, o BG Oeste pode ser subdividido em quatro unidades tectônicas: (i) Complexo Favelândia; (ii) Complexo Santa Izabel; (iii) Greenstone Belt Riacho de Santana e (iv) Batólito Guanambi. As duas primeiras unidades são complexos Arqueanos que sofreram múltiplo metamorfismo até condições de fácies granulito (Barbosa et al., 2020; Medeiros et al., 2017).

2.2.2. Bloco Gavião Sul

Esta parte do BG é limitada a leste pela porção sul do Lineamento Contendas-Jacobina (LCJ), de idade Paleoproterozóica (Sabaté et al., 1990) e a sul pela Faixa Araçuaí, de idade Neoproterozóica (Teixeira et al., 2017). De acordo com os mesmos autores, estudos geológico-geocronológicos detalhados nesta parte do BG sugeriram uma evolução prolongada do Paleo ao Neoarqueano. A crosta continental fornada no Paleo-Mesoarqueano sofreu metamorfismo e foi parcialmente reciclada em granitos e migmatitos entre 2.7 e 2.6 Ga (Santos-Pinto et al., 1998). A parte sul do BG abriga ortognaisses TTG que datam até 3.5-3.0 Ga (Nutman e Cordani, 1993; Martin et al., 1997). A maioria destes granitóides Arqueanos intrude ou engloba sequências metavulcanossedimentares e Greenstone Belts que estão dispersos pelo bloco (ex: os Greenstone Belts Ibitira-Ubiraçaba e Guajeru). Alguns exemplos de rochas Paleoarqueanas são os domos gnáissicos Sete Voltas e Boa Vista e rochas vulcânicas félsicas associadas.

2.2.3. Bloco Gavião Norte

Esta parte do BG é limitada a leste pela porção norte do LCJ e a norte pelas Faixas Neoproterozóicas Riacho do Pontal, Rio Preto e Sergipana. O Bloco Gavião Norte é composto por TTGs e ortognaisses, unidades metassedimentares, Greenstone Belts e sequências metavulcanossedimentares que datam entre 3642-2500 Ma (ex: Oliveira et al., 2020; Peucat et al., 2002; Teles et al., 2015). De acordo com Barbosa et al. (2012), as rochas Arqueanas - Paleoproterozóicas da parte mais ao norte do BG estão cobertas por rochas metassedimentares Meso e Neoproterozóicas.

2.3. Bloco Serrinha (BS)

A porção arqueana do BS (Fig. 10), denominada Complexo Santa Luz, é considerada como o embasamento dos greenstone belts Rio Itapicuru e Capim, ambos de idade paleoproterozóica (Barbosa et al., 2020). Trata-se de um conjunto gnáissico-granítico-migmatítico onde quatro associações foram

individualizadas, todas elas equilibradas no fácies anfibolito: (i) a primeira ocorre na parte centro-sul do complexo, sendo formada por ortognaisses bandados, às vezes migmatizados, com mesossoma composto por hornblenda-biotita gnaisses, de composição tonalítica a granodiorítica, possuindo enclaves de anfibolito concordantes ou não com a foliação gnáissica, e que poderiam ter sido diques máficos deformados e metamorfisados (Mello et al., 2006); (ii) a segunda aflora na porção sul do complexo, sendo constituída por biotita gnaisses, com boudins de anfibolito, incluindo kinzigitos e calcissilicáticas, onde o contato entre a primeira e a segunda associação é transicional; (iii) a terceira situa-se na parte centro-norte do complexo, onde predominam ortognaisses bandados migmatíticos, semelhantes àqueles da primeira associação, sendo compostos pela alternância de biotita gnaisse com bandas de anfibolito e de gnaisse granítico, incluindo, também, kinzigitos e metamorfitos calcissilicáticos com diopsídio, plagioclásio, quartzo, tremolita e, às vezes, associado com metabasito e mármore e, (iv) a quarta ocorre à oeste do complexo caracterizando-se pela presença de ortognaisses tonalíticos a granodioríticos, relativamente homogêneos (Barbosa et al., 2020).

Os gnaisses e migmatitos do Complexo Santa Luz (Fig.13) possuem idades U-Pb em zircão variando entre 3162 e 2933 Ma (Oliveira et al., 2002a) tendo sido retrabalhados no paleoproterozoico entre 2080 e 2000 Ma, período em que sofreram deformação, metamorfismo e fusão parcial (Mello et al., 2006). Nas vizinhanças da cidade de Retirolândia, Oliveira et al. (2002a) obtiveram idades U-Pb (SHRIMP) em zircão de 3085 Ma. Rios et al. (2009) encontraram idades de 3102 Ma (Granitóide Valente), 3162 Ma (Granitóide Ambrósio) e 2989 Ma (Granitóide Requeijão). Segundo estes autores, todos eles estão associados aos migmatitos Santa Luz e essas idades mostram a prevalência do mesoarqueano na área.



Figura 13 – Migmatito do Complexo Santa Luz, Bloco Serrinha.

2.4. Bloco Uauá (BU)

De acordo com Oliveira et al. (2019), esse bloco representa um relicto da crosta continental arqueana preservada da tectônica peleoproterozoica (Fig. 10). Nele são encontrados ortognaisses, de uma maneira geral da fácies anfibolito, retrogradada e que encerram áreas menores da fácies granulito progressiva, situadas no norte do bloco. As idades encontradas neste Bloco, por diversos métodos geocronológicos (ex: Pb-Pb, Pb-evaporação, U-Pb LA-ICP-MS) são: (i) 3302 a 3244 Ma para os ortognaisses TTG (Gordilho-Barbosa et al., submetido); (ii) 3161 Ma, para os anortositos Lagoa da Vaca; (iii) 3075 Ma, em lentes gabróicas (Barbosa et al., 2020); (iv) 3072 Ma, em ortognaisses granulitizados (Paixão e Oliveira, 1998); (v) 2993-2991 Ma, em gnaisses granodioríticos e, (vi) 2820 Ma, em granulitos máficos (Oliveira et al., 2019).

Todas essas rochas arqueanas do BU estão fortemente deformadas (Fig. 14) e, o que as tornam interessantes em termos de tectônica, é a presença de um enxame de diques toleíiticos, indeformados ,com idades obtidas em badeleíta variando entre 2624 e 2726 Ma (Oliveira et al., 2013), que cortam as foliações dos TTGs de idade paleoarqueana (Fig. 15). Diferentemente das deformações tectônicas paleoproterozoicas, que rodeiam o BU, as foliações desse bloco são

arqueanas, mais velhas que as idades dos diques (2624 e 2726 Ma) indicando que houve deformações e metamorfismo mais antigos que essas duas últimas idades.



Figura 14 – Ortognaisse do Bloco Uauá com foliação de idade arqueana.



Figura 15 – Dique de basalto toleiitico indeformado (preto) que intercepta o bandamento gnáissico mesoarqueano do Bloco Uauá.

3. Artigo 1: A review of 3.66 to 2.77 Ga crustal differentiation in the northern São Francisco Craton, Brazil.

Este artigo de revisão foi publicado na revista International Geology Review (QUALIS Capes A2, fator de impacto = 3.047) no ano de 2022, sendo incluído no volume 65, número 9, páginas 1541-1557, no ano de 2023. Para sua elaboração foram compilados dados geocronológicos (U-Pb em zircão) e isotópicos (Hf, Nd e Sr) da literatura sobre as rochas eo a mesoarqueanas da parte norte do Cráton do São Francisco.

O artigo, que teve coautoria de Alanielson da Câmara Dantas Ferreira, Felipe Padilha Leitzke, Thaiane Niederauer dos Santos, Rommulo Vieira Conceição e Hervé Martin (in memoriam), indicou que os blocos arqueanos estudados (Gavião, Serrinha e Uauá) possuem idades que variam de 3.66 a 2.77 Ga e que os blocos Gavião e Uauá possuem padrões semelhantes de evolução crustal relacionados tanto ao retrabalhamento de crosta antiga, quanto a processos de origem juvenil, o que é evidenciado pelos valores tanto positivos quanto negativos de ƐNd e de ƐHf. Já o Bloco Serrinha possui evolução crustal arqueana diferente dos outros dois blocos visto que é caracterizado por valores positivos de ƐNd, indicando origem juvenil. Essa caracterização geocronológica e isotópica permitiu, por fim, comparar a evolução crustal arqueana da parte norte do Cráton do São Francisco com aquela dos crátons Kaapvaal e Zimbabwe no sul da África e Pilbara, na Austrália.

INTERNATIONAL GEOLOGY REVIEW
2023, VOL. 65, NO. 9, 1541–1557
https://doi.org/10.1080/00206814.2022.2098542

Taylor & Francis
Taylor & Francis Group

Check for updates

A review of 3.66 to 2.77 Ga crustal differentiation in the northern São Francisco Craton, Brazil

Rafael Gordilho Barbosa[a,b], Alanielson Ferreira[c], Felipe P. Leitzke[b], Thaiane N. Dos Santos[d], Rommulo V. Conceição[a] and Hervé Martin[e†]

[a]Programa de Pós-Graduação em Geociências, Universidade Federal do Rio Grande do Sul, Campus do Vale, Porto Alegre, Brazil; [b]Laboratório de Geologia Isotópica, Universidade Federal do Rio Grande do Sul, Campus do Vale, Porto Alegre, Brazil; [c]Department of Earth Sciences, Stellenbosch University, Matieland, South Africa; [d]Instituto de Geociências, Universidade Federal do Rio Grande do Sul, Campus do Vale, Porto Alegre, Brazil; [e]Laboratoire Magmas et Volcans, Campus Universitaire des Cézeaux, Aubiere Cedex, France

ABSTRACT

The Archaean crustal evolution of the northern São Francisco Craton (SFC) reveals significant similarity with Kaapvaal-Zimbabwe and Pilbara, cratons, especially before 3.0 Ga. Likewise, compiled geochronological and Nd-Sr-Hf isotope data suggest that the Archaean blocks of the northern part of SFC (e.g. Gavião, Uauá and Serrinha) shared similar crustal evolution since 3.15 Ga. The 3.42–3.35 Ga TTGs of the southern and western Gavião Block have negative and slightly positive $\varepsilon_{Nd(t)}$ and $\varepsilon_{Hf(t)}$ values and $T_{DM(Hf)}$ ages between 3.50 and 3.90 Ga, indicating that they were produced by partial melting of Eoarchaean to Palaeoarchaean crust, with minor mantle sources. The ca. 3.30 Ga high-silica plutonic-volcanic system, which is related to intraplate magmatism and intracrustal differentiation processes, would represent processes of continental rifting and break-up. In the northern Gavião Block, the 3.64 Ga migmatite-gneiss paleosomes with negative $\varepsilon_{Hf(t)}$, $^{176}Hf/^{177}Hf$ ratio between 0.2802 and 0.2805 and $T_{DM(Hf)}$ ages between 3.75 and 4.15 Ga of the Mairi Complex represent the oldest dated rocks of the whole São Francisco Craton, suggesting late Hadean and Eoarchaean sources. The 3.15 and 3.00 Ga rocks of the Serrinha Block have positive $\varepsilon_{Nd(t)}$ values, suggesting a predominant juvenile source. Likewise, coeval 3.15 and 3.00 Ga Uauá Block rock assemblage has slightly positive to negative $\varepsilon_{Nd(t)}$ values, which indicate mixing of crustal and juvenile sources. The 2.90 to 2.77 Ga period in the SFC is characterized by pervasive crustal anatexis with high-K granite generation, similar to Kaapvaal and Pilbara cratons. Therefore, Archaean migmatite-gneiss terrains recorded four crustal differentiation intervals (e.g. 3.66–3.51, 3.45–3.30, 3.15–3.00 and 2.90–2.77 Ga) in the São Francisco Craton.

ARTICLE HISTORY
Received 29 September 2021
Accepted 03 July 2022

KEYWORDS
Eoarchaean sources; Palaeoarchaean crustal evolution; northern São Francisco Craton; Hf-Nd-Sr isotopes; crustal reworking and juvenile processes

A review of 3.66 to 2.77 Ga crustal differentiation in the northern São Francisco Craton, Brazil.

Rafael Gordilho-Barbosa[1,2], Alanielson C. D. Ferreira[3], Felipe P. Leitzke[2], Thaiane N. dos Santos[5], Rommulo V. Conceição[1], Hervé Martin[4†]

[1]Programa de Pós-Graduação em Geociências, Universidade Federal do Rio Grande do Sul, Campus do Vale, prédio 43113, Av. Bento Gonçalves, 9500, Porto Alegre, RS, Brazil. CEP: 91501-970.
[2]Laboratório de Geologia Isotópica, Universidade Federal do Rio Grande do Sul, Campus do Vale, prédio 43129, Av. Bento Gonçalves, 9500, Porto Alegre, RS, Brazil. CEP: 91501-970.
[3]Department of Earth Sciences, Stellenbosch University, Private Bag X1, Matieland, 7602, Stellenbosch, South Africa.
[4]Laboratoire Magmas et Volcans. Campus Universitaire des Cézeaux, 6 Av. Blaise Pascal, TSA 60026 – CS 60026, 63178 Aubiere Cedex, France
[5]Universidade Federal do Rio Grande do Sul, Av. Bento Gonçalves, 9500, Porto Alegre, RS, Brazil. CEP: 91501-970.
† - in memoriam
Corresponding author: Rafael Gordilho-Barbosa (rafael.gordilho@ufrgs.br)

Abstract

The Archaean crustal evolution of the northern São Francisco Craton (SFC) reveals significant similarity with Kaapvaal-Zimbabwe and Pilbara, cratons, especially before 3.0 Ga. Likewise, compiled geochronological and Nd-Sr-Hf isotope data suggest that the Archaean blocks of the northern part of SFC (e.g., Gavião, Uauá and Serrinha) shared similar crustal evolution since 3.15 Ga. The 3.42-3.35 Ga TTGs of the southern and western Gavião Block, have negative and slightly positive $\varepsilon_{Nd(t)}$ and $\varepsilon_{Hf(t)}$ values and $T_{DM(Hf)}$ ages between 3.50 and 3.90 Ga indicating that they were produced by partial melting of Eoarchaean to Palaeoarchaean crust, with minor mantle sources. The ca. 3.30 Ga high-silica plutonic-volcanic system, which is related to intraplate magmatism and intracrustal differentiation processes would represent processes of continental rifting and break-up. In the northern Gavião Block, the 3.64 Ga migmatite-gneiss paleosomes with negative $\varepsilon_{Hf(t)}$, $^{176}Hf/^{177}Hf$ ratio between 0.2802 and 0.2805 and $T_{DM(Hf)}$ ages between 3.75 and 4.15 Ga of the Mairi Complex represent the oldest dated rocks of the whole São Francisco Craton,

suggesting late Hadean and Eoarchaean sources. The 3.15 and 3.00 Ga rocks of the Serrinha Block have positive $\varepsilon_{Nd(t)}$ values, suggesting a predominant juvenile source. Likewise, coeval 3.15 and 3.00 Ga Uauá Block rock assemblage has slightly positive to negative $\varepsilon_{Nd(t)}$ values, which indicate mixing of crustal and juvenile sources. The 2.90 to 2.77 Ga period in the SFC is characterized by pervasive crustal anatexis with high-K granites generation, similar to Kaapvaal and Pilbara cratons. Therofore, Archaean migmatite-gneiss terrains recorded four crustal differentiation intervals (e.g. 3.66-3.51, 3.45-3.30, 3.15-3.00 Ga and 2.90-2.77 Ga) in the São Francisco Craton.

Keywords: Eoarchaean sources, Paleoarchaean crustal evolution, northern São Francisco Craton, Hf-Nd-Sr isotopes, crustal reworking and juvenile processes

3.1. Introduction

The Earth's oldest cratons represent the relicts of Eoarchaean to Palaeoarchaean continental crust formed by tonalite-trondhjemite-granodiorite (TTG) series associated with Na-rich granites (e.g. Zeh et al. 2009; Kemp et al. 2015; Petersson et al. 2019; Chaudhuri, 2020). In this context, the major question is how early plate tectonics and crustal generation processes operated (e.g., Petersson et al. 2020; Gardiner et al. 2021). The early Archaean crustal fragments have been well studied for decades (e.g. Condie, 1989; Teixeira et al. 2000; Moyen et al. 2021). Some of the most well-known cratons are the Kaapvaal and Zimbabwe cratons, in southern Africa, and the Pilbara Craton, in western Australia (e.g. Smithies et al. 2007; Zeh et al. 2009; Jelsma et al. 2021; Mühlberg et al. 2021) that, similarly to the São Francisco Craton, host rocks with ages between 3.45 Ga and 3.65 Ga. In South America, the São Francisco Craton (Almeida et al. 1981) is one of the largest cratonic areas and its northern portion contains the ca. 3.66 Ga TTG orthogneisses related to early crustal differentiation, which are the oldest dated rocks in the continent. (e.g., Oliveira et al. 2020; Moreira et al. 2022; Santos et al. 2022).

Despite a long history of geologic research, there are still uncertainties about the sources and crustal mechanisms that contributed to the evolution of the São Francisco Craton (SFC) throughout Archaean times (e.g., Martin et al. 1997; Guitreau et al. 2012; Lana et al. 2013; Teixeira et al. 2017; Oliveira et al. 2020). Thus, more work is needed to understand the timing, mechanisms and conditions of the 3.66 to 2.77 Ga geological processes, by studying the exposed Archaean

rocks formed at different crustal levels, such as: (i) high-grade metamorphic terranes of TTG's, which represent Archaean mid-continental crust; (ii) low-grade granite-greenstone belts related to Archaean upper continental crust and (iii) medium-high grade metamorphic rocks, re-equilibrated at amphibolite- to granulite facies.

Therefore, to obtain a better understanding of the northern SFC crustal evolution zircon U-Pb and Hf, Nd and Sr isotope data available in the literature from 1985 to 2021 were compiled. This allowed us to compare the nature of the three blocks in which Eo to Mesoarchaean rocks crop out (i.e. Gavião, Serrinha and Uauá blocks). In order to place the SFC in a global context of Archaean crustal evolution, a comparison between São Francisco (Brazil), Pilbara (western Australia), Kaapvaal and Zimbabwe (southern Africa) cratons was established, which have similarities that will be further discussed.

3.2. Data compilation

A comprehensive literature review was undertaken in order to identify geochronological and isotopic studies performed in the Eo- to Mesoarchaean rocks of the northern SFC. The systematic quantitative approach presented by Pickering and Byrne (2014) was utilized, since this method is reproducible, explicit and presents few biases in comparison with traditional review systematics (de Brito and Evers, 2016). To make sure that relevant papers were not missed, different databases such as Science Direct, Web of Science, Periódicos CAPES, Scopus, Springer Link and ProQuest were systematically searched. Publications such as book chapters, conference proceedings and reports, peer-reviewed articles, doctoral dissertations and masters theses written in English, French and Portuguese were included. As a result, 23 references about the São Francisco Craton published over more than three decades (between 1985 and 2021) were compiled, including a total of 284 Hf, Nd and Sr isotope data. The main geochronological and isotope data and their references are presented in supplementary materials 1 to 3. Furthermore, Hf isotope data of the SFC were plotted together with data from Pilbara (western Australia), Kaapvaal and Zimbabwe cratons (southern Africa) in time-integrated diagrams, in order to build a global appraisal of Eo to Mesoarchaean crustal growth intervals.

3.3. Geological background

The São Francisco Craton (SFC) (Fig.1) is constituted by distinct Archaean granitic-gneissic complexes. In the south, the craton is composed of the Belo Horizonte, Campo Belo, Passa Tempo and Santa Bárbara complexes, which comprise medium to-high grade metamorphic terranes. They are composed of TTG rocks, K-rich granitic plutons and migmatites (Teixeira et al. 2017). Remnants of supracrustal rocks, as well as mafic dykes and layered mafic-ultramafic bodies also occur in the Quadrilátero Ferrífero region (e.g., Machado et al. 1992; Pinese et al. 1995; Teixeira et al. 2000; Alkmim and Noce, 2006; Goulart et al. 2013; Lana et al. 2013; Romano et al. 2013; Teixeira et al. 2017). In the northern portion of the SFC, the Gavião, Serrinha, Jequié and Itabuna-Salvador-Curaçá blocks represent the main Archaean units, which are comprised of metamorphosed rocks from granulite (TTG terranes) to greenschist facies (supracrustal sequences) (e.g., Barbosa and Sabaté 2002, 2004; Barbosa and Barbosa, 2017). This article focuses on the northern SFC comprising the Gavião, Serrinha and Uauá blocks.

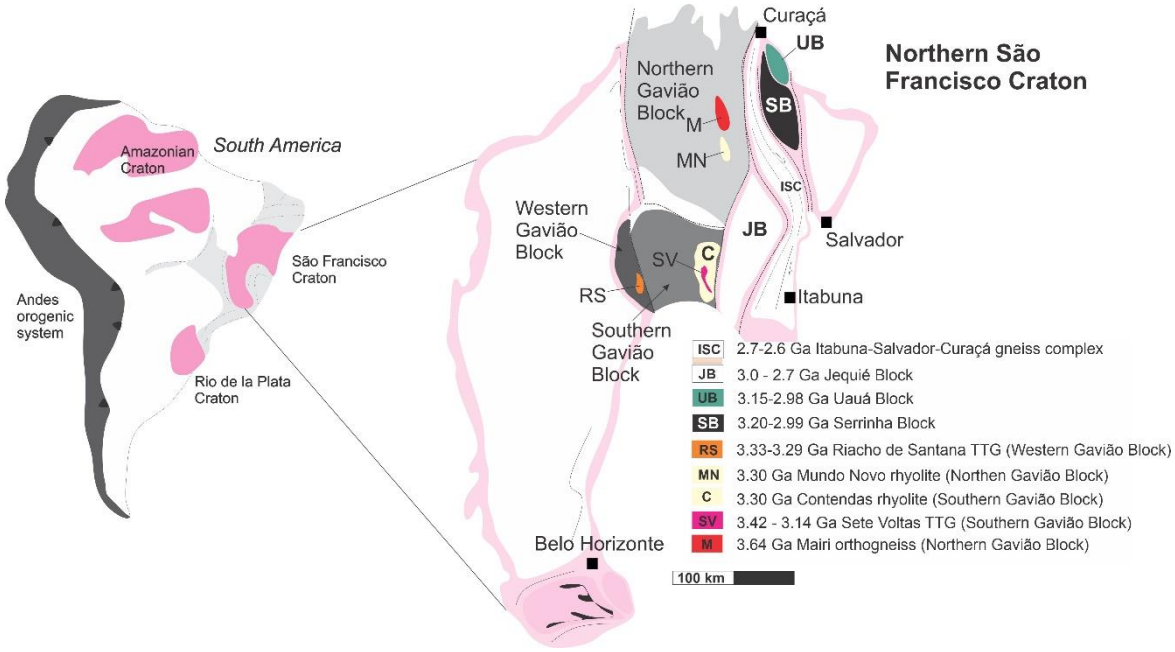

Figure 1 - Major tectonic compartments of the northern Sao Francisco Craton. C - Contendas rhyolite; ISC - Itabuna-Salvador-Curaca Belt; JB - Jequie Block; M - Mairi Orthogneiss; MN - Mundo Novo rhyolite; RS - Riacho de Santana TTG; SB - Serrinha Block; SV – Sete Voltas TTG; UB - Uaua Block. Modified from Gordilho-Barbosa et al. (2021).

3.3.1. Gavião Block (GB)

The GB comprise a variety of TTGs, migmatites, gneisses and granites as well as greenstone belts (e.g., Barbosa et al. 2012; Barbosa et al. 2020). Specifically, older TTG orthogneisses were dated between 3654 – 3260 and 3180 – 3000 Ma (e.g., Nutman and Cordani, 1993; Martin et al. 1997; Peucat et al. 2002; Dantas et al. 2013; Barbosa et al. 2020; Oliveira et al. 2020; Moreira et al. 2022) (Figs.2 and 3). Most of these TTGs and migmatites are associated with older metavolcanic-sedimentary sequences that occur scattered within the block. An age of 4.15 Ga was obtained from a detrital zircon of the Ibitira-Ubiraçaba metavolcanic-sedimentary sequence within the southern GB, which can be considered as indirect evidence of Hadean crust in the area (e.g., Paquette et al. 2015). Since the GB represents most of the area of the northern SFC, as shown in Fig. 1, we present through this article a geographical subdivision, into Northern, Southern and Western Gavião Block. This eases the orientation of the reader within the craton, despite of the isotope data showing that the GB was a single tectonic unit during Archaean times.

3.3.1.1. Northern Gavião Block

This part of the GB is bounded to the east by the northern portion of the Contendas-Jacobina Lineament (CJL) (Sabaté et al. 1990) and to the north by the Neoproterozoic Riacho do Pontal, Rio Preto and Sergipano Belts. According to Barbosa et al. (2012), the Archaean-Palaeoproterozoic rocks of the northernmost GB are, largely, covered by Meso-and-Neoproterozoic meta-sedimentary rocks. The northern GB is constituted of TTGs and orthogneisses, meta-sedimentary units, greenstone belts and metavolcano-sedimentary sequences dated between 3.65 and 2.50 Ga (e.g., Moreira et al. 2022; Oliveira et al. 2020; Peucat et al. 2002; Teles et al. 2015) (Fig. 3A) (Supplementary material and references therein). In the northernmost part of the GB, gneisses and migmatites contain rare gabbro-diorite enclaves, in which Dantas et al. (2010) found a zircon population dated at ca. 3.53 Ga. These rocks have Sm-Nd TDM model ages up to 3.70 Ga, while the zircon Hf TDM ages vary between 3.70 and 3.90 Ga (Dantas et al. 2010,2013). Thus, these data indicate that Eoarchaean components occur in this part of GB, which is similar to the Riacho de Santana region in the western Gavião Block.

3.3.1.2. Western Gavião Block

The western part of the GB is composed of Palaeo-to-Neoarchaean rocks that are intruded by the Palaeoproterozoic Guanambi batolith and coeval rocks (e.g. Barbosa et al. 2012; Barbosa et al. 2013; Cordani et al. 1985; Rosa et al. 2000). The western GB, in the Riacho de Santana region, is divided into two tectonic units, which are gneiss-migmatite Archaean complexes that underwent a complex metamorphic evolution highlighted by granulite facies rocks (e.g., Barbosa et al. 2013; Barbosa et al. 2020; Medeiros et al. 2017; Rosa et al. 2000). Rosa (1999) reported an U-Pb crystallization age of 3.35 Ga for a gneiss xenolith in the Palaeoproterozoic Cara Suja granite. A LA-ICP-MS zircon U-Pb age of ca. 3.35 Ga is considered as representative of the crystallization of the Riacho de Santana TTG (Barbosa et al. 2013; 2020) (Fig. 3B). It has TDM ages between 3.91 – 3.59 Ga and εNd(t) varying from -7.0 to -0.1, (Barbosa et al. 2013; Teixeira et al. 2017; Barbosa et al. 2020).

3.3.1.3. Southern Gavião Block

This part of the GB is bounded to the east by the southern portion of the Palaeoproterozoic Contendas-Jacobina Lineament (CJL) (Sabaté et al. 1990) and to the south by the Neoproterozoic Araçuaí Belt (e.g., Teixeira et al. 2017). Detailed geologic-geochronological studies in the GB have suggested a protracted evolution from the Palaeoarchaean to the Neoarchaean (e.g., Teixeira et al. 2017). The continental crust formed in the Palaeo-Mesoarchaean underwent metamorphism and partial recycling into granites and migmatites between 2.70 and 2.60 Ga (Santos-Pinto et al. 2012). The southern GB hosts TTG orthogneisses dated between 3.45-3.20 Ga (e.g. Nutman and Cordani, 1993; Martin et al. 1997). Most of these granitoids intrude or encompass metavolcanic-sedimentary sequences and greenstone belts that are scattered over the block, (e.g., Nutman and Cordani, 1993; Leal et al. 1996). Some examples of the Palaeoarchaean rocks are the Sete Voltas (Fig.3C, E, F) and Boa Vista gneissic domes and associated felsic volcanics (Supplementary material and references therein).

3.3.2. Serrinha Block (SB)

The SB is the smallest Mesoarchaean unit in the northern SFC (Teixeira et al. 2017) but is one of the best-known areas of the craton. It represents an approximately N-S elongated segment that is limited to the west and to the south by the Palaeoproterozoic Itabuna-Salvador-Curaçá Block (e.g., Barbosa and

Sabaté, 2002,2004). The oldest rocks of the SB are Mesoarchaean (3.08-2.98 Ga) migmatites, TTGs, banded gneisses, mafic-ultramafic complexes and mafic dykes of the Santa Luz Complex (Oliveira et al. 2010). According to Oliveira (2011), the banded gneiss unit represents the end product of the deformation of migmatites and mafic dykes during the accretion of the Palaeoproterozoic Rio Itapicuru Greenstone Belt onto the Archaean basement. Palaeoproterozoic intrusions related to the Itabuna-Salvador-Curaçá orogen (Barbosa and Sabaté, 2002, 2004) intrude the Archaean basement. Remnants of ~3.10 Ga migmatitic enclaves are found within the Ambrósio dome (Mello et al. 2006), and the Palaeoproterozoic Quijingue trondhjemite contains 3.31 and 3.62 Ga old, inherited zircons (Rios et al. 2008). This suggests that Palaeo-to Mesoarchaean material formed the precursor crust of the Serrinha Block. From a geochronological and isotopic perspective, the Santa Luz Complex can be divided into two domains of grey gneisses (i.e. the Retirolândia – ca. 3.08 Ga and the Jacurici – ca. 2.98 Ga domains; Oliveira et al. 2010). Both of these domains are constituted of TTG suites respectively with Sm-Nd TDM model ages between 3.2-3.1 Ga and 3.20-2.90 Ga and the εNd(t) values varying between 0 and +1.1 and 0 and +4.9 respectively, suggesting a predominant juvenile origin (Table 1).

3.3.3. Uauá Block (UB)

The UB is bordered to west by the Archaean-Palaeoproterozoic Caldeirão Belt, to the east by the Palaeoproterozoic Rio Capim Greenstone Belt (Oliveira et al. 2011; 2013) and to the south by the Serrinha Block. The oldest rocks in the UB are banded gneisses of 3.15-3.12 Ga (Oliveira et al. 2019) (Fig. 3D), intruded by Mesoproterozoic layered anorthosite, peridotite and diorite complexes, pre-metamorphic mafic dykes and tonalite-granodiorite bodies. Neoarchaean non-metamorphic norite-tholeiite dykes crosscut the country rocks in some places (Oliveira, 2011; Oliveira et al. 2013 and references therein) (Supplementary material and references therein). With exception of the Neoarchaean noritic (2.73 Ga) and tholeiitic (2.62 Ga) dykes (Oliveira et al. 2013), much of the basement rocks underwent granulite facies metamorphism and were later retrogressed to amphibolite facies. The felsic granulitic bodies, with interspersed garnet-bearing mafic granulites, are strongly foliated, frequently with horizontal or south-dipping low-angle foliation. The available isotopic data from the rocks of UB (Table 1) show εNd(t) between -6.6 and +1.6, indicating an origin associated with juvenile and crustal reworking processes. Cordani et al. (1999) obtained ages between 3.12 and 3.13 Ga for the Capim tonalite, whereas Oliveira et al. (2010) reported

felsic igneous bodies with ages between 3.07 and 2.99 Ga. According to Oliveira et al. (2011, 2013), the younger tholeiitic dyke swarm (2.62 Ga), which crosscuts the gneisses of the basement, may represent a failed arm of a Neoarchaean rift system.

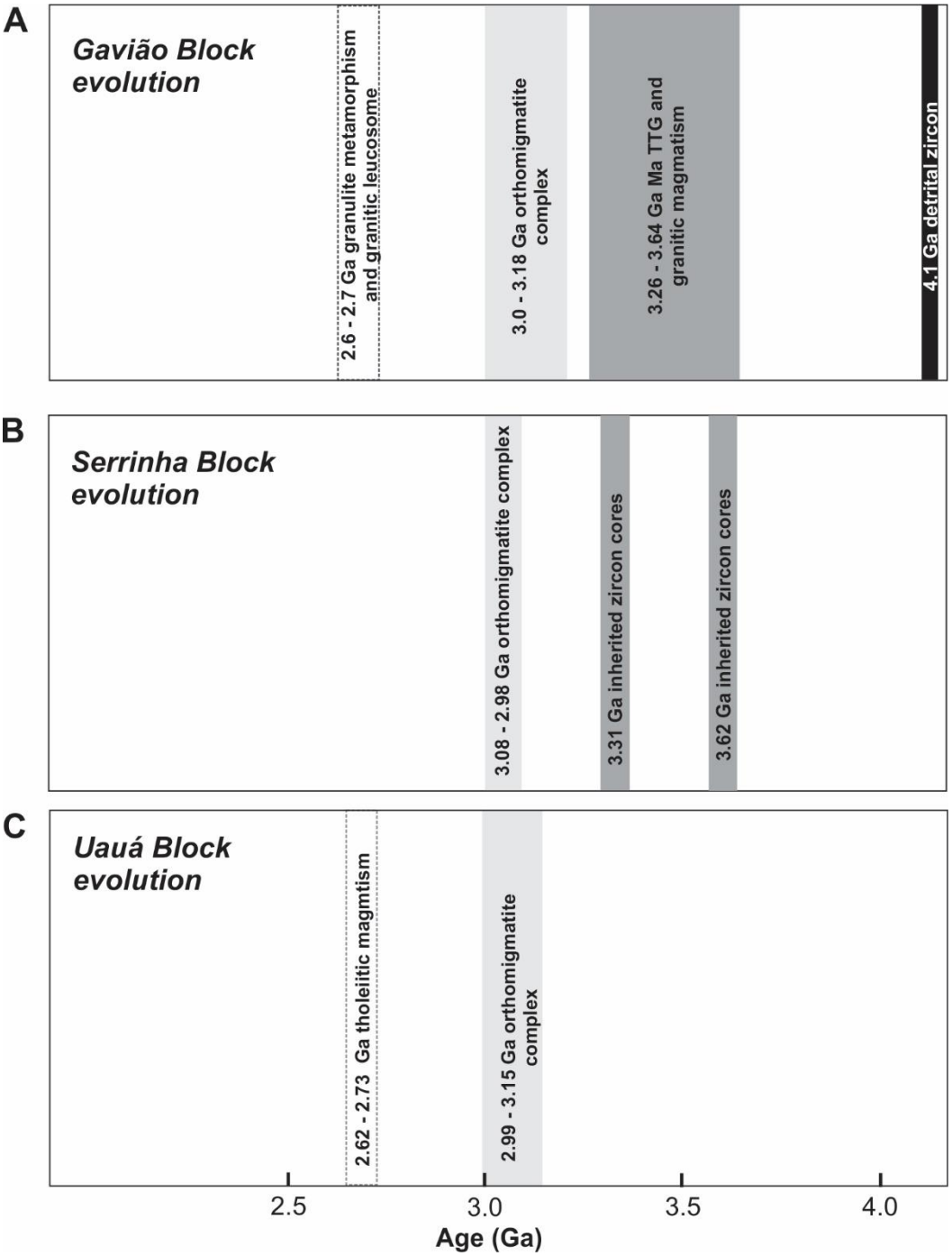

Figure 2 – Comparison of the Archaean crustal evolution of Gavião, Serrinha and Uauá Blocks.

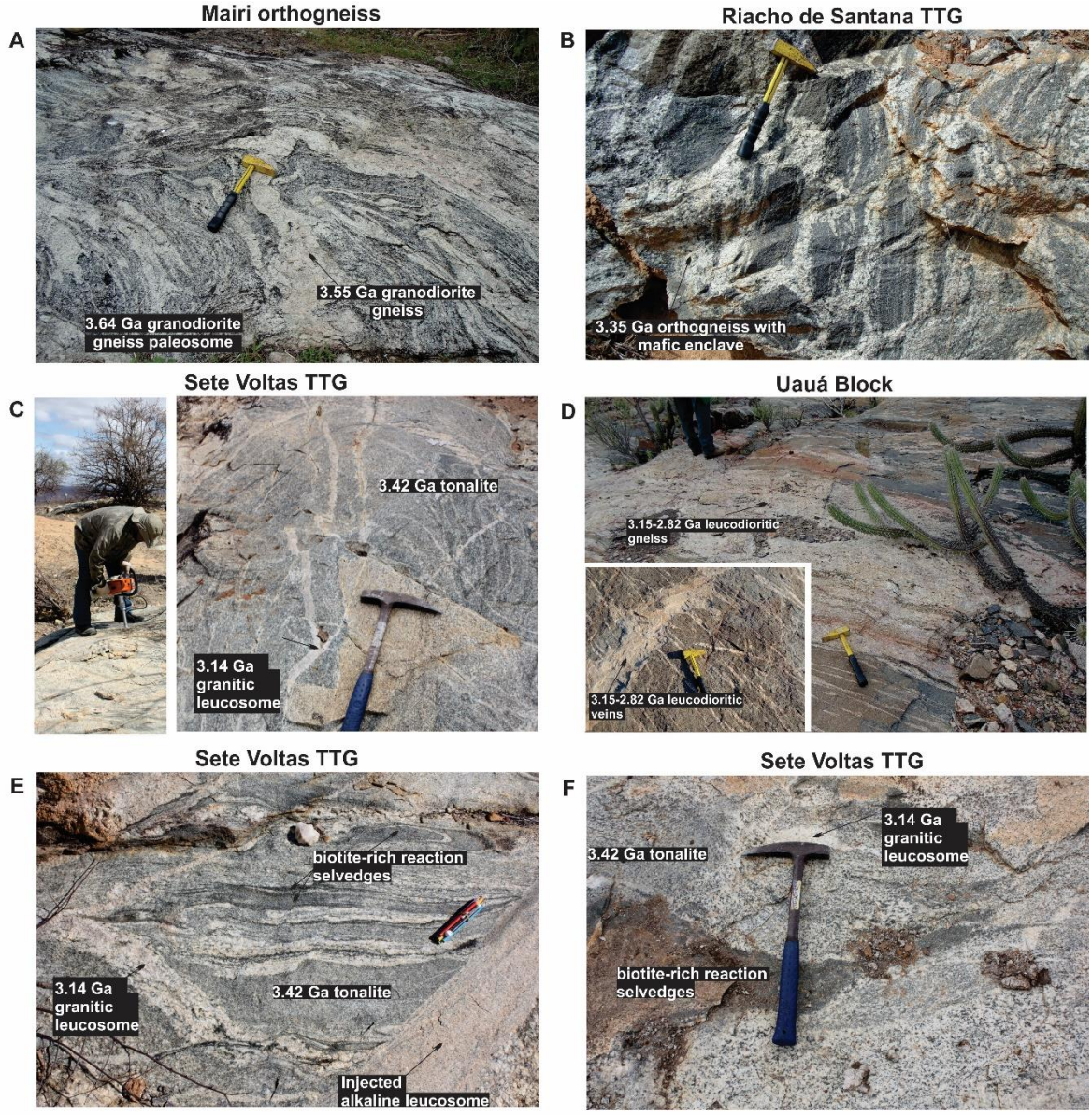

Figure 3 – Field photos. A – Outcrop of the Mairi orthogneiss. In this photo it is possible to observe the 3.64 Ga granodiorite gneiss paleosome and the 3.55 granodiorite gneiss. B – Outcrop of the Riacho de Santana TTG in which the 3.35 Ga orthogneiss with mafic enclaves occur. C – Outcrop of the Sete Voltas TTG containing both the 3.42 Ga tonalite and the 3.14 Ga granitic leucosome. D – Outrcrop photo of the 3.15-2.82 Ga leucodioritic gneiss from the Uauá Block. The small picture is a detail photo of the same rock. E and F – Sete Voltas TTG. In these photos is possible to notice the 3.42 Ga tonalite, the 3.14 Ga leucosome and the biotite-rich reaction selvedges.

3.4. Results and data evaluation

The geochronological and isotopic data that were compiled from the literature are summarized in Table 1 and allowed the observation of four different crustal differentiation events in the northern SFC with ages of 3.66-3.51 Ga; 3.45-3.30 Ga; 3.10-3.00 Ga and 2.90-2.80 Ga. The Hf, Nd and Sr isotopes data suggest that crustal reworking and juvenile processes contributed to the evolution of this

part of the craton.

Block	U-Pb age (zircon - Ga)	$^{87}Sr/^{86}Sr(i)$	$^{143}Nd/^{144}Nd(i)$	εNd(t)	$T_{DM(Nd)}$ - Ga	$^{176}Hf/^{177}Hf(i)$	εHf(t)	$T_{DM(Hf)}$ - Ga
Gavião	3.66 to 2.77	0.7006 to 0.7296	0.5079 to 0.5093	-8.8 to +11.6	2.84 to 4.22	0.2802 to 0.2806	-9.2 to +0.6	3.46 to 4.15
Serrinha	3.16 to 2.98	0.6302 to 0.6999	0.5086 to 0.5089	0.01 to 4.9	2.71 to 3.19	n.a	n.a	n.a
Uauá	3.15 to 2.80	n.a	0.5083 to 0.5088	-6.6 to 1.0	2.99 to 3.62	0.2807 to 0.2809	-8.5 to +3.6	3.06 to 3.43

Table 1 – Summary of the zircon U-Pb ages and Hf, Nd, Sr isotopes data of the northern SFC.

3.4.1. U-Pb zircon ages

The compiled zircon U-Pb ages presented in Table 1 and supplementary material 1 indicate that during the Eo-to Mesoarchaean, four different crustal differentiation periods occurred in the northern SFC. The Gavião Block hosts units with ages between 3.65 Ga (e.g. Mairi orthogneisses, northern GB – Oliveira et al. 2020; Moreira et al. 2022), and 2.83 Ga (e.g. granite from Umburanas Massif, southern GB – Santos Pinto et al. 2012). The Serrinha and Uauá Blocks have Mesoarchaean ages, varying between 3.16 Ga (e.g. orthogneiss from Ambrósio Dome – Lacerda, 2000; Mello et al. 2006) and 2.98 Ga (e.g. orthogneiss from Jacurici domain – Oliveira et al. 2010) for the SB, and ages between 3.15 Ga (e.g. metapelite from Caldeirão Belt – Oliveira et al. 2002a) and 2.80 Ga (e.g. granitoids from Rio Capim greenstone belt and Uauá Block – Sato,1998) for the UB.

3.4.2. Sr isotopes

According to Rollinson and Pease (2021), the Rb-Sr isotope system has the largest compatibility difference among parent and daughter elements, resulting in easy separation and fractionation of Rb and Sr between crust and mantle. This leads into a fast evolution of Sr isotopes in the continental crust relative to the mantle (with time, $^{87}Sr/^{86}Sr$ ratios in the crust will be greater than in the primitive mantle). However, one of the main drawbacks when applying this method is that both Rb and Sr are relatively mobile elements, which may affect the quality of the data when a sample has experienced interaction with fluids or thermal events (Rollinson and Pease, 2021). The compiled $^{87}Sr/^{86}Sr_{(i)}$ data presented in Table 1 and in supplementary material 1 indicate that these ratios for the Gavião Block vary between 0.7002 (e.g. Lagoa do Morro granitoid, southern GB – Nutman and

Cordani, 1993) and 0.7296 (e.g. granite from Umburanas Massif, southern GB – Santos Pinto et al. 2012). For the Serrinha Block, only disturbed $^{87}Sr/^{86}Sr_{(i)}$ values are available in the literature and, for the Uauá Block there are no available $^{87}Sr/^{86}Sr_{(i)}$ data in the literature.

3.4.3. Nd isotopes

The available $^{143}Nd/^{144}Nd_{(i)}$, $\varepsilon Nd_{(t)}$ and $T_{DM(Nd)}$ data are very useful in the determination of the petrogenetic processes that contributed to the crustal evolution of the northern SFC, because they can be utilized as indicators of the sources of the studied Archaean blocks (Zindler and Hart, 1986).

For the Gavião Block, the $^{143}Nd/^{144}Nd_{(i)}$ varies between 0.5079 (e.g. migmatite/orthogneiss from the Riacho de Santana Complex, western GB – Barbosa et al. 2013) and 0.5093 (e.g. metakomatiite from the Umburanas greenstone belt, southern GB – Leal et al. 1998). The $\varepsilon Nd_{(t)}$ values range from -8.8 (e.g. gneiss from the Aracatu massif, southern GB – Santos Pinto, 1996) and +11.6 (e.g. metakomatiite from the Umburanas greenstone belt, southern GB – Leal et al. 1998). The $T_{DM(Nd)}$ values vary between 2.84 Ga (e.g. tholeiitic volcanic from the Contendas-Mirante metavolcanic-sedimentary sequence, southern GB – Marinho, 1991) and 4.22 Ga (e.g. gneiss from the Aracatu Massif, southern GB – Santos Pinto, 1996).

In the Serrinha Block the $^{143}Nd/^{144}Nd_{(i)}$ ratio varies between 0.5086 (e.g. trondhjemite from the Pedra Alta massif – Rios, 2002a) and 0.5089 (e.g. migmatite/orthogneiss from the basement of the Rio Itapicuru greenstone belt – Lacerda, 2000). The $\varepsilon Nd_{(t)}$ values range from 0.01 (e.g. migmatite/orthogneiss of the basement of the Rio Itapicuru greenstone belt – Lacerda, 2000) to +4.9 (e.g. diorite from the Santa Luz Complex – Rios et al. 2009). The TDM(Nd) values vary between 2.71 Ga (e.g. diorite from the Santa Luz Complex – Rios et al. 2009) and 3.19 Ga (e.g. trondhjemite from the Pedra Alta massif – Rios, 2002a).

For the Uauá Block the $^{143}Nd/^{144}Nd_{(i)}$ ratio ranges between 0.5083 (e.g. tonalite from the Rio Capim greenstone belt – Sato, 1998) and 0.5088 (e.g. gneiss from Uauá Block – Oliveira et al. 2000). The $\varepsilon Nd_{(t)}$ values vary from -6.6 (e.g. tonalite from Rio Capim greenstone belt – Sato, 1998) to +1.6 (e.g. gneiss from the Uauá Block – Oliveira et al. 2000). The compiled $T_{DM(Nd)}$ ages for the Uauá Block are between 2.99 Ga (e.g. gneiss from Uauá Block – Oliveira et al. 2000) and 3.62 Ga (e.g. tonalite from Rio Capim greenstone belt – Sato, 1998).

3.4.4. Hf isotopes

The compiled $^{176}Hf/^{177}Hf_{(i)}$, $\varepsilon Hf_{(t)}$ and $T_{DM(Hf)}$ data are a very useful tool in the determination of the petrogenetic processes that contributed to the crustal evolution of the northern SFC because as the Nd isotopes, they can be utilized as indicators of the sources of the studied Archaean blocks.

For the Gavião Block the $^{176}Hf/^{177}Hf_{(i)}$ ratio varies between 0.2802 (e.g. TTG from the Piritiba region, northern Gavião Block – Oliveira et al. 2020) and 0.2806 (e.g. rhyolite from the Contendas-Mirante region, southern Gavião Block – Zincone et al. 2016). The $\varepsilon Hf_{(t)}$ values range from -9.2 (e.g. TTG from the Piritiba region, northern Gavião Block – Oliveira et al. 2020) to +0.65 (e.g. rhyolite from the Contendas-Mirante region, southern Gavião Block – Zincone et al. 2016). The compiled $T_{DM(Hf)}$ data vary between 3.46 Ga (e.g. rhyolite from the Contendas-Mirante region, southern Gavião Block – Zincone et al. 2016) and 4.15 Ga (e.g. TTG from the Piritiba region, northern Gavião Block – Oliveira et al. 2020). For the Uauá Block, the $^{176}Hf/^{177}Hf_{(i)}$ ratio ranges between 0.2806 (e.g. leucodioritic gneiss – Oliveira et al. 2019) and 0.2809 (e.g. mafic granulite – Oliveira et al. 2019). According to the same authors, the $\varepsilon Hf_{(t)}$ vary between -8.53, obtained for the leucodioritic gneiss, and +3.56, for the mafic granulite and the $T_{DM(Hf)}$ data of the UB varies between 3.43 and 3.08 Ga. Up-to-present-day there are no available Hf isotope data from the Serrinha Block. The Hf isotope data are shown in supplementary material 2.

3.5. Discussion

3.5.1 Zircon U-Pb age and isotopic constraints

Geochronological data compiled in this article suggest the occurrence of four episodes of crust formation in the northern São Francisco Craton (e.g. 3.66-3.51 Ga, 3.45-3.30 Ga, 3.20-3.00 Ga and 2.90-2.77 Ga). The ca. 3.42 Ga TTG's (e.g., Sete Voltas TTG) produced by partial melting of Archaean mantle sources, with hornblende garnet residue, represent the more pervasive magmatic precursors to the São Francisco Craton (e.g., Martin et al. 1997; Guitreau et al. 2012; Teixeira et al. 2017). The 3.33 to 3.29 high-silica rhyolitic-granitic systems have formed after a period of crustal growth and stabilization of a thick continental

litosphere and are related to intraplate magmatism and intracrustal differentiation processes (e.g., Zincone et al. 2016). The igneous protoliths of the 3.17 - 3.15 Ga migmatite-gneiss and porphyritic granodiorites were produced by new partial melting of an already differentiated crust at depths of ~ 30-45 km (e.g., Martin et al. 1997). Lastly, ~2.60 Ga high-K granites (e.g. Caraguataí syenitic suite – Cruz et al. 2012; also referred as Caraguataí granitic suite by Lopes et al. 2021), Fe-Ti-V-rich mafic dykes (e.g. Rio Jacaré Sill – Brito, 2000) and alkaline granitic intrusions (e.g. Pé de Serra granite – Marinho, 1991) related to the late-stage collisional event were emplaced along the ca. 3.40 and ca. 3.15 Ga high-grade migmatite-gneiss terranes (e.g., Martin et al. 1997). According to Lopes et al. (2021) the ocurrence of the ca. 2.70 Ga high-K granites of the Caraguataí suite suggests that the southern part of the GB was already stabilized at this period. Likewise, 3.64 Ga Palaeoarchaean gneisses have negative εHf(t) values and TDM(Hf) ages between 3.75 and 4.15 Ga, indicating late Hadean to Eoarchaean sources or contamination by older Eoarchaean continental crust The 3.10-3.00 Ga rocks of the Serrinha Block have slightly positive εNd(t) values and TDM ages between 3.10-3.20 Ga, suggesting that their sources may have been of juvenile origin while in the Uauá Block shows slightly positive and negative εNd(t) values and TDM ages between 3.20 and 3.30 Ga, indicating Palaeoarchaean sources and some amounts of juvenile contribution during its evolution, which is different to what occurs in the GB. The 2.90-2.77 Ga period is characterized by widespread anatexis, and the 2.70-2.60 Ga period is related to the occurrence of granitic magmatism in the southern GB (e.g. Barbosa et al. 2012).

3.5.2. Nd and Sr isotopic data

The Nd T_{DM} ages and negative to positive $\varepsilon Nd_{(t)}$ for the SFC blocks confirm a complex Archaean history with multiple crustal reworking stages associated with mantle sources (Fig. 4A to F) (e.g., Martin et al. 1997; Guitreau et al. 2012; Zincone et al. 2016; Teixeira et al. 2017). The Northern and Southern Gavião blocks share ca. 3.50 and 3.30 Ga juvenile sources with pervasive crustal partial melting at 3.42-3.45 and 3.20-3.30 Ga (Fig. 4A,B). Specifically, the Sete Voltas complex records complementary Nd isotopic patterns, indicating that the ca. 3.15-3.17 Ga granodioritic to granitic rocks were generated by partial melting of the ca. 3.42 Ga TTGs (Fig. 4C). A ca. 3.00 Ga accretionary process with juvenile and reworked sources is recorded in the Brumado Complex and in the Contendas-Mirante metavolcanic-sedimentary sequence in the Southern Gavião Block (Fig. 4A,C). The Western Gavião Block presents a ca. 3.30 Ga crustal accretion event

with mixed 3.30 Ga juvenile and ca. 3.50-3.60 Ga crustal sources and younger ca. 3.00 Ga partial melting of the previous ca. 3.10 Ga continental crust (Fig.4D). Likewise, the Uauá Block displays 3.10 Ga and 2.90 Ga juvenile rocks with 3.00 and 2.80 Ga crustal reworking (Fig.4E). Lastly, the Serrinha Block presents positive $\varepsilon Nd_{(t)}$ values with similar evolution to Uauá indicating some contribution from 3.10 - 3.00 Ga components of mantle-derived and minor 3.00 Ga crustal reworking sources (Fig.4F).

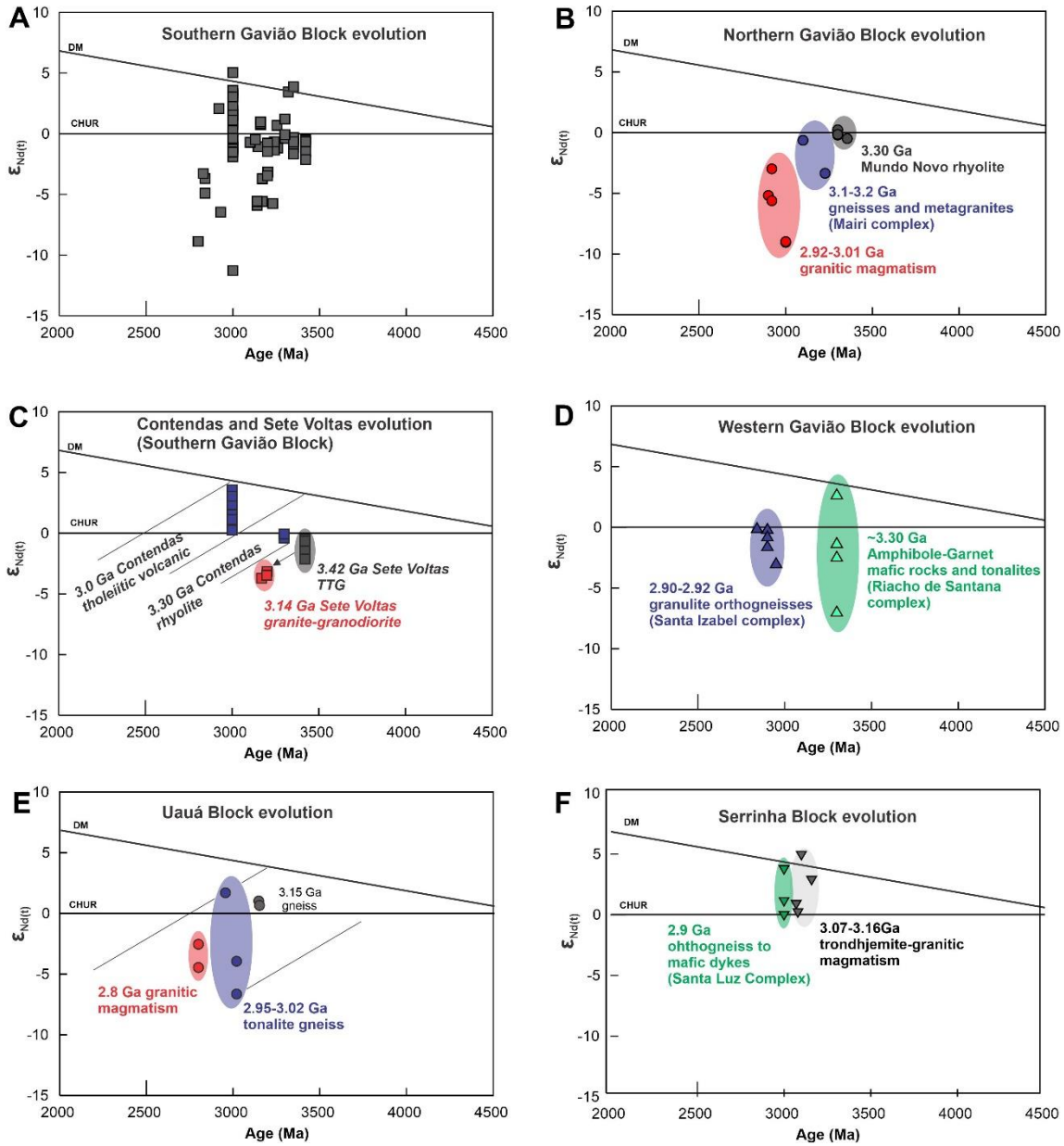

Figure 4 – $\varepsilon Nd_{(t)}$ vs age diagrams for the Archaean blocks of the northern São Francisco Craton. A - Southern Gavião Block, indicating the occurrence of juvenile and crustal reworking processes. B - Northern Gavião Block, suggesting the occurrence of juvenile and crustal reworking processes in two different periods. C - $\varepsilon Nd_{(t)}$ vs age diagram for the 3.42 Ga Sete Voltas TTG, the 3.30 Ga Contendas rhyolite, the 3.17-3.14 Ga Sete Voltas granitic leucosome and the 3.0 Ga tholeiitic rocks from the Contendas-Mirante metavolcanic-sedimentary sequence, suggesting the occurrence of crustal reworking and juvenile processes. D - Western Gavião Block, indicating the occurrence of different periods of crustal reworking and juvenile processes. E - Uauá Block, suggesting two different periods of juvenile and crustal reworking processes. F - Serrinha Block, indicating essentially juvenile processes for the origin of this crustal segment.

The lower initial $^{87}Sr/^{86}Sr$ and Rb/Sr ratios, relative to the 3.30 Ga high-Si plutonic-volcanic system, of both the 3.50-3.40 Ga TTGs and the 3.20 to 3.00Ga granodioritic to granitic rocks, (Fig. 5A,B) could indicate that these rocks are generated by anatexis of the lower continental crust (e.g., White and Powell, 2010). In contrast, high initial $^{87}Sr/^{86}Sr$ and Rb/Sr ratios associated with the high-Si granitic magmatism (Fig. 5A,B) could have originated by partial melting of high K/Na rocks in the upper continental crust (e.g., Zincone et al. 2016). In addition, Rb/Sr ratios vs U-Pb zircon diagram (Fig. 5A) suggest a linear enrichment evolution for the ca. 3.40 Ga TTGs, high initial Rb/Sr ratios for the ca. 3.30 Ga high-Si granitic magmatism and lower ratios for the ca. 3.00 Ga tholeiitic rocks.

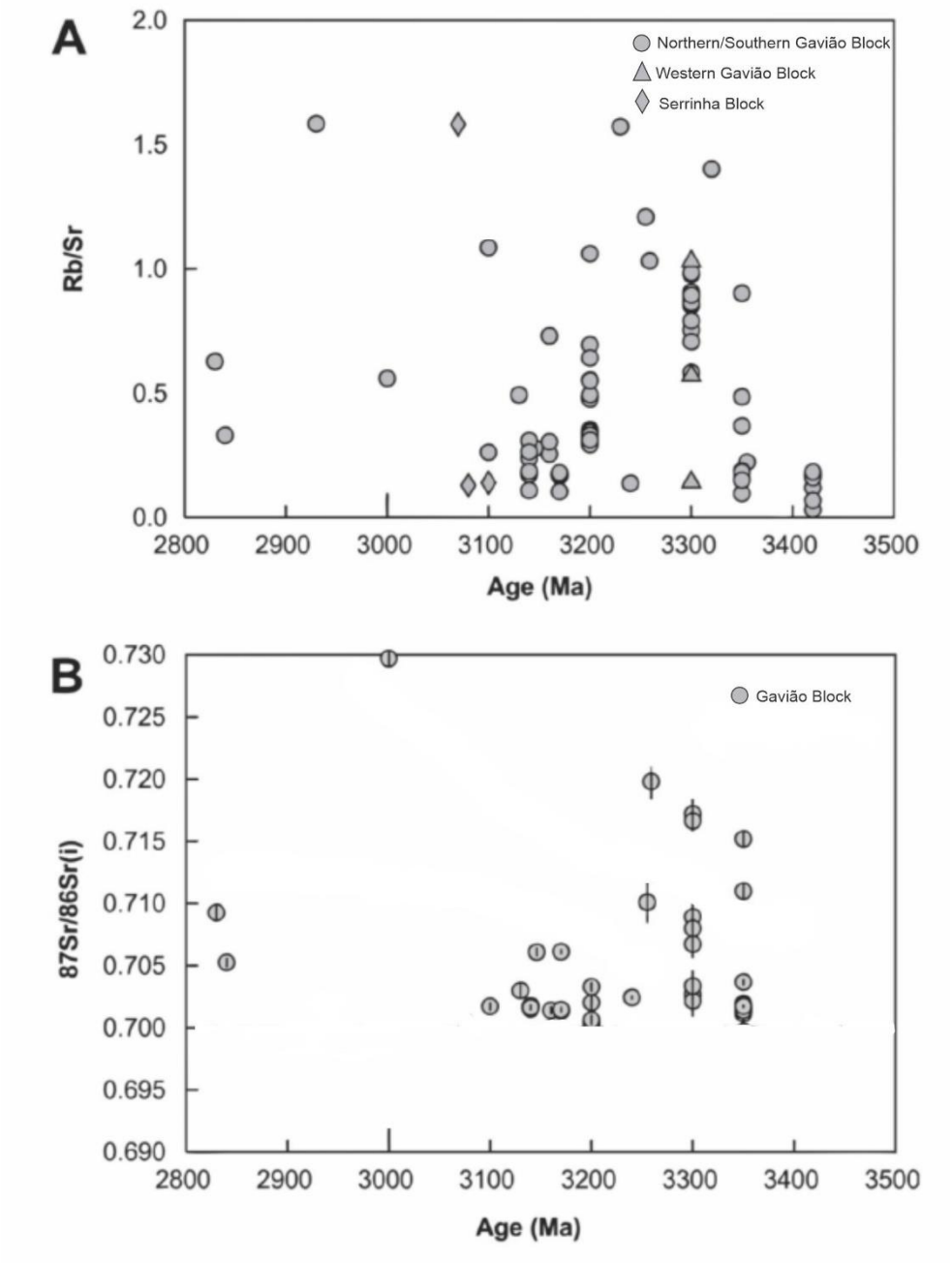

Figure 5 – Sr isotopic data for the Archean São Francisco blocks. A – Rb/Sr vs age diagram for the northern SFC, suggesting high initial Rb/Sr ratios for the 3.30 Ga rhyolitic-granitic systems, a linear enrichment evolution for the 3.45 Ga TTGs and low initial Rb/Sr ratios for

the 3.1-3.0 Ga tholeiitic rocks. B – $^{87}Sr/^{86}Sr_{(i)}$ vs age diagram for the rocks of the northern SFC. The lower $^{87}Sr/^{86}Sr_{(i)}$ for the 3.5-3.4 Ga tonalite residue and 3.2-3.0 Ga granodioritic to granitic leucosome may indicate anatexis of the lower crust, while high $^{87}Sr/^{86}Sr_{(i)}$ in high-Si granitic magmatism suggest partial melting of high K/Na rocks in the upper continental crust.

The Sete Voltas complex is the best example to understand the Palaeoarchaean crustal evolution of the São Francisco Craton. The ca. 3.42 Ga TTG rocks have low initial $^{87}Sr/^{86}Sr$ and Rb/Sr ratios, whereas 3.15 to 3.17 Ga granitic to granodioritic rocks have higher initial $^{87}Sr/^{86}Sr$ and Rb/Sr ratios (Fig. 6A,B). Moreover, $T_{DM(Nd)}$ ages and $\varepsilon Nd_{(t)}$ values show progressive evolution and fractionation from the 3.42 Ga TTG's towards the 3.17-3.15 Ga granites and granodiorites (Fig. 6C). Therefore, combined whole-rock Nd and Sr isotopic patterns indicate that the ca. 3.17 Ga Sete Voltas granodiorite and the 3.14 Ga granite are derived from the 3.42 Ga Palaeoarchaean TTGs (e.g. Martin et al. 1997) (Fig. 6D).

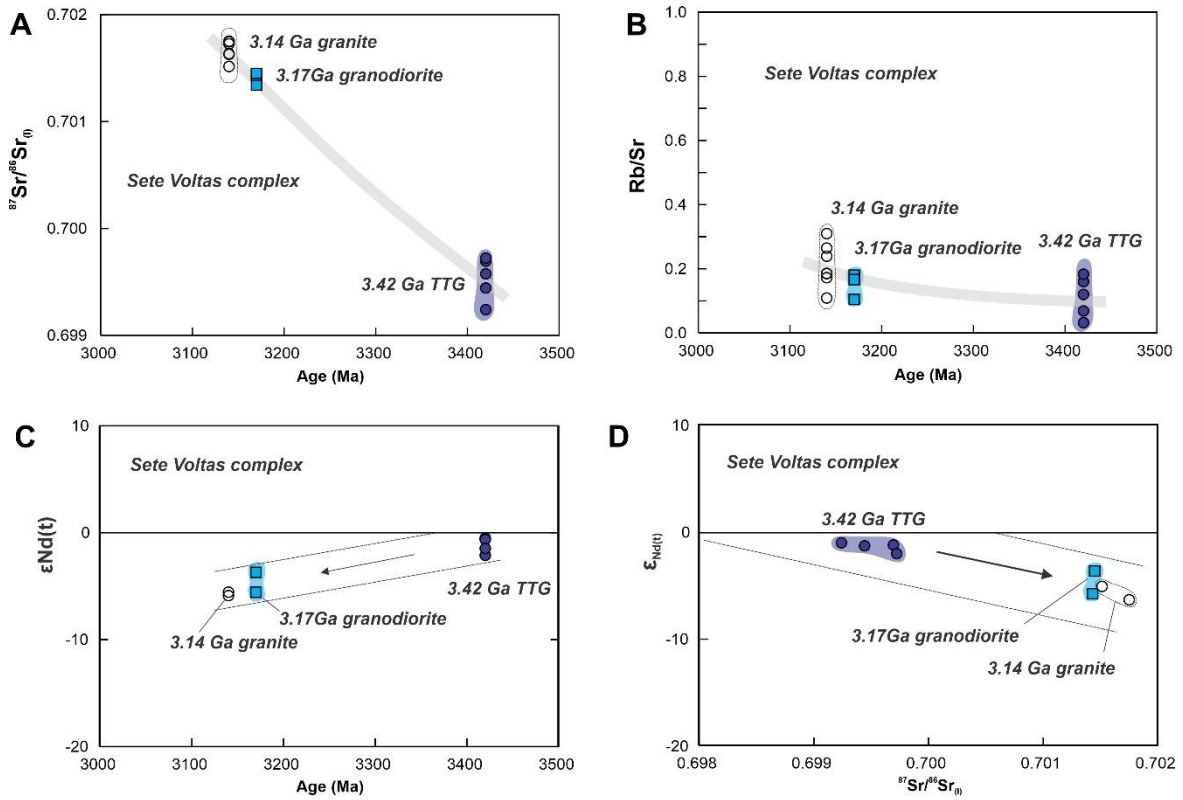

Figure 6 – Nd and Sr isotopic data for the Sete Voltas complex. A – $^{87}Sr/^{86}Sr(i)$ vs age diagram indicating that the 3.42 Ga TTG residue has lower $^{87}Sr/^{86}Sr_{(i)}$ than the 3.17 Ga Sete Voltas granodiorite and the 3.14 Ga Sete Voltas granitic leucosome. B – Rb/Sr vs age diagram showing that the 3.42 Ga TTG residue has lower Rb/Sr ratio than the 3.17 Ga Sete Voltas granodiorite and the 3.14 Ga Sete Voltas granitic leucosome. C - $\varepsilon Nd_{(t)}$ vs age diagram indicating that the 3.42 Ga TTG residue could have been the source of the 3.17 Ga Sete Voltas granodiorite and the 3.14 Ga Sete Voltas granitic leucosome. D – $^{143}Nd/^{144}Nd$ vs $^{87}Sr/^{86}Sr$ diagram suggesting that the 3.17 Ga Sete Voltas granodiorite and 3.14 Ga granitic leucosome are derived from the 3.42 Ga Sete Voltas TTG.

3.5.3. Hf isotopic data

The compiled Hf isotopes data do not allow the division of the GB in Northern, Southern and Western Gavião blocks in the Archaean; thus it is merely geographical (Fig. 7A,B). The integrated Hf isotopic dataset suggests that an ancient crust with TDM(Hf) between 3.75 and 4.15 Ga reworked at 3.64 - 3.55 Ga for the Mairi orthogneiss, in the northern portion of the SFC, which is evidenced by the εHf(t) values between -9.3 and -0.3 (Fig. 7A,B) (supplementary material 2) (e.g., Oliveira et al. 2020). New crust generation, with TDM(Hf) between 3.50 and 3.90 Ga, and reworking at 3.40 and 3.30 Ga, associated with minor juvenile contributions is represented by the 3.42 Ga Sete Voltas TTG (e.g. Martin et al. 1997; Guitreau et al. 2012) and the 3.30 Ga Mundo Novo and Contendas rhyolites (Figs. 6A,B) (e.g., Zincone et al. 2016).

The older ca. 3.64 Ga TTG series from the northern São Francisco Craton have negative εHf(t) values and are less geochemically enriched, indicating reworked sources (e.g., Oliveira et al. 2020). In contrast, the 3.50 to 3.20 Ga TTG (e.g., Guitreau et al. 2012; Zincone et al. 2016) and granodioritic magmatism present negative and positive εHf(t) values, enriched trace element compositions and inherited zircon grains and cores (e.g., Oliveira et al. 2020). The 3.66 and ca. 3.45 - 3.15 Ga SFC terranes experienced several partial melting events with multiple magmatic pulses, which have obliterated the original protolith signatures. Furthermore, it also reflects a variable mixing of TTG crust and juvenile sources during the Palaeoarchaean (Fig. 8). Specifically, the Hf isotopic data support a predominantly reworked crustal source to the 3.64 Ga Mairi orthogneiss; evolved crust and limited juvenile contribution to the 3.45 Ga TTGs; felsic protolith to ~3.30 Ga high-silica magmatism and significant assimilation of Eoarchaean/Palaeoarchaean precursors for the 3.17 - 3.15 Ga migmatite-gneiss and granodiorites (e.g., Zincone et al. 2016; Oliveira et al. 2020). This scenario is similar to the Hf evolution documented in the Kaapvaal, Pilbara and Zimbabwe cratons (e.g., Kemp et al. 2015; Petersson et al. 2019; Gardiner et al. 2021; Hofmann et al. 2022 Lastly, different structures, ages and geochemical profiles support that the 3.60 to 3.10 Ga Palaeo- to Mesoarchaean terrane recorded in São Francisco craton were formed from heterogeneous sources with distinct crustal anatexis paths.

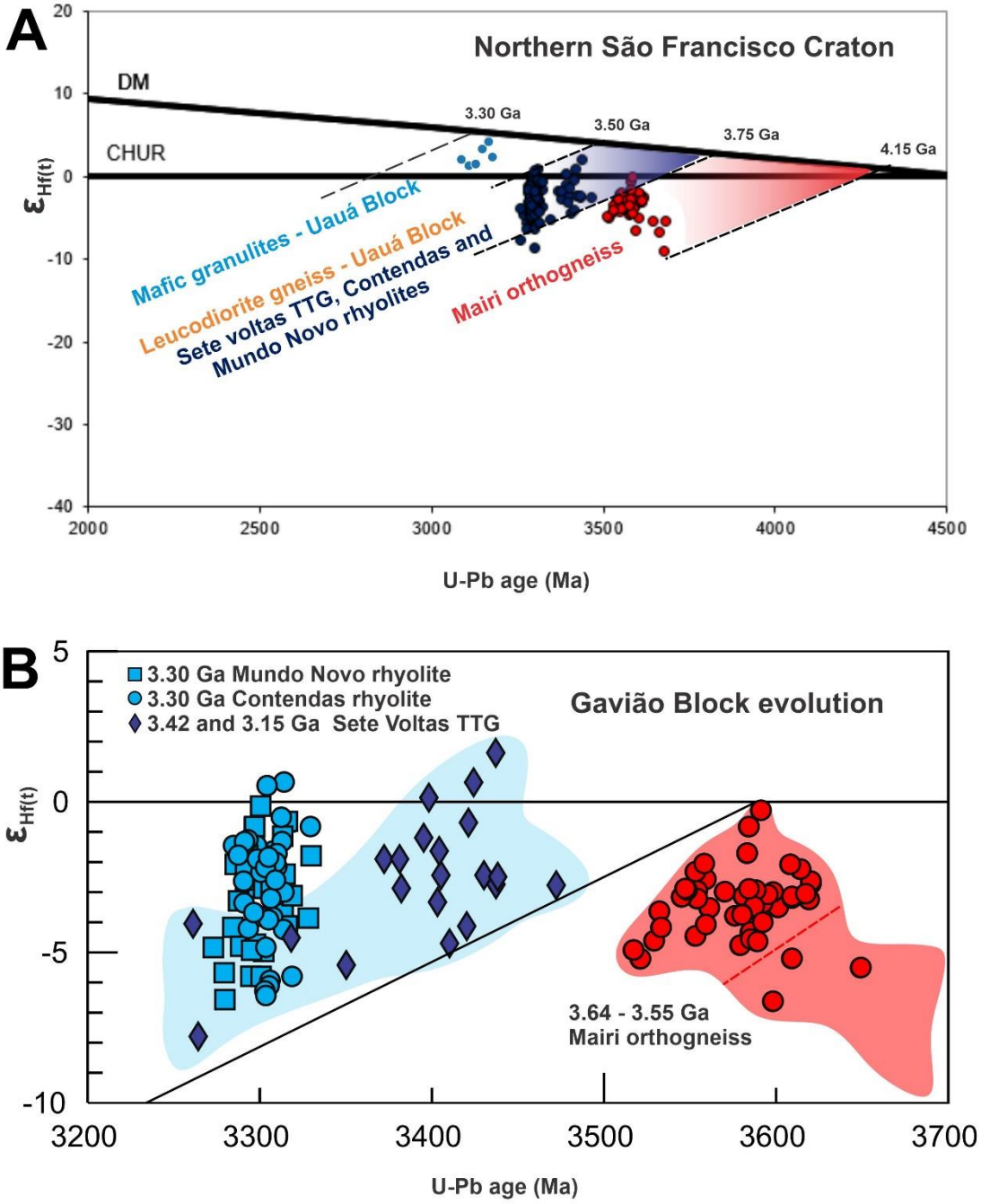

Figure 7 – Archaean Hf isotopic data for the northern São Francisco Craton. A - $\varepsilon Hf_{(t)}$ vs age diagram suggesting that the sources of the 3.64 Ga Mairi orthogneiss, in the northern portion of the GB, is associated to reworking of Hadean crust, while the sources of the 3.42 Ga Sete Voltas TTG; 3.30 Ga Contendas and Mundo Novo rhyolites and 3.15 Ga leucodioritic gneiss of the Uauá Block are related to crustal reworking of Palaeo-to-Mesoarchaean crustal sources. The diagram also suggests that the origin of the 3.15-2.80 Ga mafic granulites of the Uauá Block is associated with a Palaeo-to-Mesoarchaean mantle source. B – Detail $\varepsilon Hf_{(t)}$ vs age diagram showing the evolution of the Gavião Block.

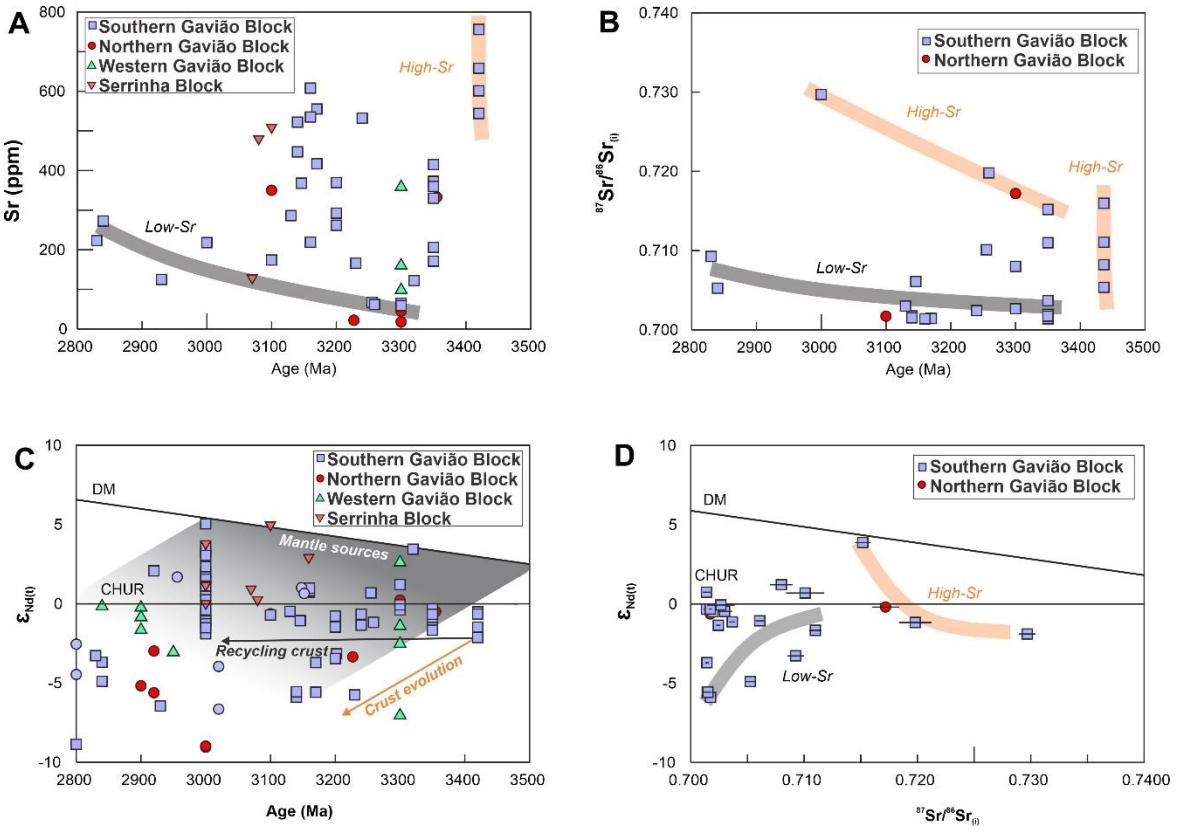

Figure 8 – Juvenile crust and reworking events for the Archaean blocks of the northern São Francisco Craton (data from Supplementary Material 1). A – Sr vs age diagram indicating that the oldest rocks of the northern SFC have higher Sr contents. B – $^{87}Sr/^{86}Sr_{(i)}$ vs age diagram showing two groups of rocks, which indicate that crustal reworking and juvenile processes occurred in the northern SFC. C – $\varepsilon Nd_{(t)}$ vs age diagram showing the crustal evolution processes that occurred in the northern SFC. D - $\varepsilon Nd_{(t)}$ vs $^{87}Sr/^{86}Sr_{(i)}$ diagram indicating that the crustal evolution of the northern SFC is related to juvenile and crustal reworking processes.

3.5.4. Crustal differentiation evolution and Archaean correlations

The comparison among Archaean cratons requires understanding that they have evolved by multiple ways of crustal differentiation and recycling (e.g., Moyen et al. 2021). Kaapvaal, Singhbhum and Pilbara cratons are classic Palaeoarchaean cratons, which stabilized much earlier than most other cratons (e.g., Chaudhuri, 2020; Hofmann et al. 2022). The orthogneiss terrains have zircon ages of ca. 3.66-3.63, 3.52-3.51, and ca. 3.30 Ga that also support the existence of Eo- to Palaeoarchaean crust in the São Francisco and Zimbabwe cratons (e.g., Santos et al. 2022; Hofmann et al. 2022). Specifically, the SFC presents multiple continental crust growth peaks at 3.30 and 3.00 Ga combined with moderate peaks at ca. 3.66-3.55, 3.45-3.42, and 3.17-3.15 Ga. It is similar to Pilbara (Western Australia) and Kaapvaal-Zimbabwe cratons (southern Africa) (e.g., Zeh et al. 2009; Petersson et al. 2019; Chaudhuri, 2020; Gardiner et al.

2021; Hofmann et al. 2022). The similarities between these cratons are observed in their εHf(t) values which are superimposed (Fig. 9A).

The systematic U-Pb zircon ages in the São Francisco and other cratons indicate that 3.66-3.55 Ga and 3.45 Ga constituted a period of significant Eo-to-Palaeoarchaean crustal growth marked by TTG magmatism, while the TDM(Hf) values obtained suggest the occurrence of reworking of Hadean to Eoarchaean crust (Figs. 9A,B) (e.g., Martin et al. 1997; Horstwood et al. 1999; Guitreau et al. 2012; Petersson et al. 2020; Santos et al. 2022). The older crustal differentiation is represented by the 3.65 - 3.55 Ga Mairi TTG complex derived from high-Sr protoliths in the northern GB (Figs. 5A,B and 6A). In contrast, in the southern GB, the 3.45-3.42 and 3.35 Ga Sete Voltas complex represented the partial melting of Eoarchaean crust with minor juvenile contribution (e.g., Martin et al. 1997). Indeed, the 3.55 to 3.42 Ga rocks were the main sources for Mesoarchaean rocks generated by partial melting (e.g., Horstwood et al. 1999; Kemp et al. 2015; Chaudhuri, 2020; Gardiner et al. 2021). The 3.33 to 3.29 Ga high-Si volcanism would represent the continental rifting for the SFC (e.g., Zincone et al. 2016) while 3.53 to 3.17 Ga volcanic-sedimentary successions and autochthonous groups followed by 3.20 to 3.10 Ga continental break-up are recorded in the Pilbara Craton (e.g., Smithies et al. 2007).

The northern and southern portions of the Gavião Block recorded similar geological evolution since ca. 3.30 Ga, which is evidenced by high-Si magmatism with mixed reworked and juvenile sources (Fig. 8B-D). The 3.20, 3.10 and 3.00 Ga pervasive crustal recycling events are also documented in all of the northern SFC blocks. Moreover, the isotopic and chemistry data support that the 3.10 to 3.20 Ga granites and porphyritic granodiorites, from Kaapvaal, Pilbara and São Francisco cratons were derived from the Palaeoarchaean crustal sources compatible with the 3.40 - 3.50 Ga TTG rocks (e.g. Martin et al. 1997; Smithies et al. 2007; Zeh et al. 2009; Petersson et al. 2020; Mühlberg et al. 2021). Moreover, combined positive and negative εHf(t) and εNd(t) values support mantle and crustal sources during 3.15 - 3.00 Ga northern SFC and Pilbara craton crustal evolution (e.g. Martin et al. 1997; Smithies et al. 2007). Lastly, the 2.95 to 2.77 Ga high-K granitic magmatism occur in a thicker and stabilized continental crust (e.g., Lana et al. 2013). Overall, emplacement of younger (<2.9 Ga) high-K granitic and sanukitoid magmas, followed by crustal stabilization is a pervasive phenomenon in Archaean terrains (e.g., Moyen and Martin, 2012; Laurent et al. 2020; Ferreira et al. 2021).

Compiled geochronological and Nd-Sr-Hf isotope data suggest that the

northern part of the SFC developed into stable crustal blocks since ca. 3.15 Ga (Figs. 8, 9A). Moreover, these data reveal that the Archaean high- and low-grade metamorphic terranes of the northern SFC were formed from distinct parental magmas and have complex and different early to mid-Archean histories (Fig. 8A-D; Gavião, Serrinha and Uauá blocks) (e.g., Martin et al. 1997; Guitreau et al. 2012; Teixeira et al. 2017; Oliveira et al. 2020; Moreira et al. 2022; Santos et al. 2022). Therefore, isotope and geochemical data support multiple recycling processes, including pervasive crustal differentiation of mantle-derived melts during the formation of the proto-São Francisco Craton. However, complementary studies are necessary to better understand the Eo- to Palaeoarchaean crustal differentiation and juvenile magma addition in the SFC.

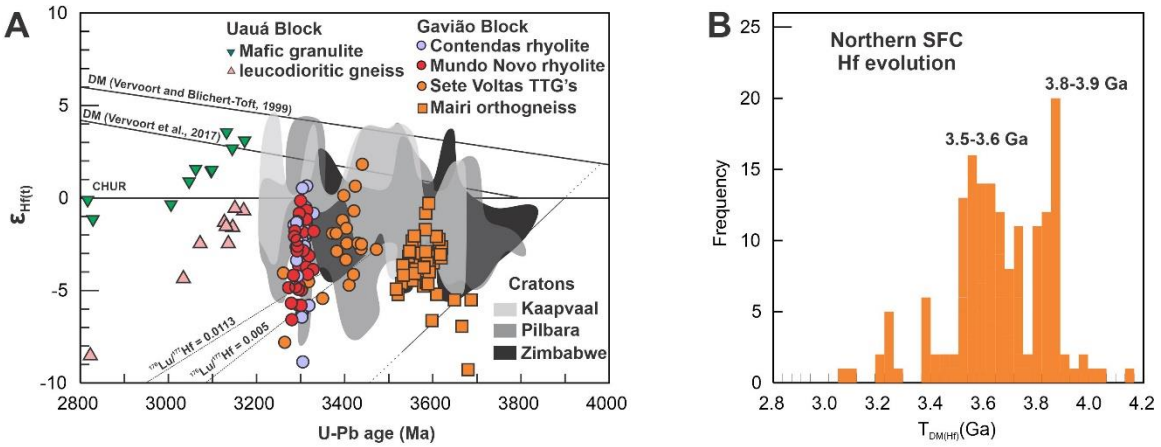

Figure 9 – Hf isotope data. A – $\varepsilon Hf_{(t)}$ vs age diagram showing that the crustal evolution of the northern São Francisco Craton had similarities with that of Kaapvaal, Pilbara and Zimbabwe cratons. This suggests that similar processes occurred in different portions of the early Archaean crust. The data from Kaapvaal and Pilbara cratons were compiled from Gardiner et al. (2021) and the data from Zimbabwe craton were compiled from Hofmann et al. (2022). Crust values of 0.0113 and 0.005 from Bouvier et al. (2008). DM trend from Vervoort and Blichert-Toft (1999) and Vervoort et al. (2017). B – Histogram indicating the distribution of the $T_{DM(Hf)}$ data of the northern São Francisco Craton.

3.6. Conclusion

The continental growth of the SFC occurred by the combination of diverse crustal components via sporadic contribution of juvenile sources and prolonged reworking of the Haden to Palaeoarchaean crust associated with multiple deformations and partial melting events during the 3.65 to 2.80 Ga period. Thus, based on the compiled data, it is possible to conclude that:

- The Nd isotope data suggest that the Eo-to-Mesoarchaean crustal evolution of the northern SFC was associated with juvenile and crustal reworking processes.
- The lower $^{87}Sr/^{86}Sr_{(i)}$ for the 3.50-3.40 Ga tonalite and 3.20-3.00 Ga granodiorites to granites suggest anatexis of the lower crust, while high $^{87}Sr/^{86}Sr_{(i)}$, for the 3.30 Ga, high-Si granitic magmatism suggests partial melting of high K/Na rocks in the upper continental crust.
- The Hf isotope data suggest the occurrence of ca. 4.15-3.90 Ga crustal sources to the Mairi orthogneiss (northern Gavião Block) and a second large period of crust generation between 3.75 and 3.50 Ga, with restricted contribution of juvenile sources. At 3.30 Ga and, mainly, at 3.00 Ga occurs an intense mixing of older crusts with juvenile magmas.
- The northern part of the SFC shows similar crustal evolution with Kaapvaal and Zimbabwe Cratons, in southern Africa and with Pilbara Craton, in western Australia, at least until 3.00 Ga, suggesting that, in the Archaean, the same processes occurred in different parts of Earth's primitive crust.
- Despite these conclusions, some questions about the early evolution of the northern São Francisco Craton remain unanswered. For instance: i) what is the nature of the source(s) of the 3.65-3.42 Ga TTG gneisses? ii) which early-Earth processes did give rise to the parental magmas of the gneisses' protoliths?

4. Artigo 2 : Palaeoarchaean crustal formation in the Uauá Block, northern São Francisco Craton, Brazil: evidence for 3.3 to 3.0 Ga collisional tectonics

Este artigo foi submetido à revista Geoscience Frontiers (QUALIS Capes A1, fator de impacto = 8.9) no ano de 2023. Para sua elaboração foram obtidos dados petrográficos, geoquímicos de rocha total, geocronológicos (U-Pb em zircão), isotópicos (Lu-Hf) e de elementos traço em zircão de um gnaisse migmatítico que aflora no Bloco Uauá, na borda nordeste do Cráton do São Francisco.

O artigo, que teve coautoria de Alanielson da Câmara Dantas Ferreira, Felipe Padilha Leitzke, Ísis Cortez, Cristiano Lana, Rommulo Vieira Conceição e Johildo Salomão Figueiredo Barbosa, indicou que o gnaisse migmatítico possui um resíduo composto por hornblenda + plagioclásio + quartzo e um leucossoma constituído por plagioclásio + quartzo + clinopiroxênio + ortopiroxênio + hornblenda e que a ocorrência de ortopiroxênio no resíduo indica a ocorrência de metamorfismo de alta temperatura, enquanto que a hornblenda sugere retrogressão para o fácies anfibolito. Geoquimicamente, em termos de elementos maiores e traços, o gnaisse migmatítico possui composição similar às rochas da suite tonalito-trondhjemito-granodiorito (TTG), mais especificamente aqueles de baixa a média pressões. Foram identificados dois tipos de zircão no gnaisse migmatítico e eles apresentam morfologia externa e feições internas que possibilitaram classificá-los como ígneos e metamórficos. Em termos de idade, os zircões ígneos apresentaram dois conjuntos de idades ^{207}Pb-^{206}Pb em zircão: i) 3320 Ma (intercepto superior) e ii) 3245 Ma (idade Concordia) o que torna o gnaisse migmatítico a rocha mais antiga datada no Bloco Uauá até então. Já os zircões metamórifcos apresentam idades de 3099 Ma, relacionada ao metamorfismo de alta temperatura (fácies granulito) e de 2989 Ma, possivelmente relacionado à retrogressão para o fácies anfibolito. Os zircões ígneos possuem εHf(t) variando entre -4,85 e 1,55, sugerindo a ocorrência de processos tanto de retrabalhamento de crosta antiga quanto processos de natureza juvenil na sua geração, enquanto que os zircões metamórficos possuem εHf(t) variando entre -7.06 e -0,39, evidenciando sua natureza crustal. Os valores de T_{DMHf} encontrados variam de 3,76 a 3,53 Ga, sugerindo a existência de crosta do

Eoarqueano ao início do Paleoarqueano no Bloco Uauá. Os dados de elementos traço em zircão permitiram identificar o ambiente tectônico de geração do gnaisse migmatítico como sendo colisional.

De modo geral a evolução crustal paleo a mesoarqueana do Bloco Uauá se deu da seguinte maneira: um protólito ígneo de 3320 Ma foi retrabalhado em um ambiente tipo arco em 3245 Ma e foi submetido a metamorfismo de alta temperatura (fácies granulito) em 3099 Ma, sendo por fim, retrogradado ao fácies anfibolito em 2989 Ma.

Geoscience Frontiers

Palaeoarchaean crustal formation in the Uauá Block, northern São Francisco Craton, Brazil: evidence for 3.3 to 3.0 Ga collisional tectonics

--Manuscript Draft--

Manuscript Number:	
Article Type:	Research Paper
Keywords:	Paleoarchaean migmatite-gneiss; continental accretion; early arc magmatism; , Pb-Hf-REE in zircon; Uauá Block
Corresponding Author:	Rafael Gordilho-Barbosa Universidade Federal do Rio Grande do Sul Porto Alegre, RS BRAZIL
Suggested Reviewers:	Axel Hofmann, PhD Prof, University of Johannesburg Department of Geology ahofmann@uj.ac.za Prof. Hofmann has been studying Archean crustal evolution for the past decades.
	Tim Johnson, PhD Prof, Curtin University Faculty of Science and Engineering Tim.Johnson@curtin.edu.au Prof. Johnson is an expert on the field of Archean crustal evolution
	Renato Moraes, PhD Prof, University of Sao Paulo Institute of Geosciences rmoraes@usp.br Prof. Moraes is an expert in the field of high grade metamorphism.
	Cristopher Spencer, PhD Prof, Queen's University cs252@queensu.ca Prof. Spencer is an expert on Precambrian crustal evolution
First Author:	Rafael Gordilho-Barbosa, MSc
Order of Authors:	Rafael Gordilho-Barbosa, MSc
	Alanielson Ferreira, PhD
	Felipe Padilha Leitzke, PhD
	Ísis de Moraes Cortez
	Cristiano Lana, PhD
	Rommulo Vieira Conceição, PhD
	Johildo Salomão Figueiredo Barbosa, PhD

Palaeoarchaean crustal formation in the Uauá Block, northern São Francisco Craton, Brazil: evidence for 3.3 to 3.0 Ga collisional tectonics

Rafael Gordilho-Barbosa[a,d*], Alanielson Ferreira[b], Felipe P. Leitzke[c,d], Ísis M. Cortez[d], Cristiano Lana[e], Rommulo V. Conceição[a], Johildo S.F. Barbosa[f]

[a]Programa de Pós-Graduação em Geociências, Universidade Federal do Rio Grande do Sul. Campus do Vale, prédio 43113, Av. Bento Gonçalves, 9500, Porto Alegre-RS, Brazil. CEP: 91501-970.
[b]Instituto de Geociências, Universidade de Brasília. Campus Universitário Darcy Ribeiro, ICC – Ala Central, Brasília-DF, Brazil. CEP: 70919-970.
[c]Institut für Geologie und Mineralogie, Universität zu Köln, Zülpicher Straße 49b, 50674 Cologne, Germany.
[d]Centro de Engenharias, Universidade Federal de Pelotas. Rua Benjamin Constant, 989, Pelotas-RS, Brazil. CEP: 96010-020
[e]Applied Isotope Research Group, Departamento de Geologia, Escola de Minas, Universidade Federal de Ouro Preto, Campus Universitário Morro do Cruzeiro, s/n, Ouro Preto-MG, Brazil. CEP: 35400-000
[f]Núcleo de Geologia Básica, Universidade Federal da Bahia. Av. Barão de Jeremoabo, s/n, Ondina, Salvador-BA, Brazil. CEP: 40170-110.
*Corresponding author – rafael.gordilho@ufpel.edu.br; +5571 99974-4545

Abstract

It is widely debated when crustal growth and reworking through arc magmatism first operated on Earth. Here we report Archean rocks that can be best explained to be formed at convergent plate boundaries. Research was conducted in the Uauá Block, northeastern edge of the São Francisco Craton, Brazil, in order to investigate the petrogenesis of an migmatite-gneiss that is part of the block's basement, at the Uauá Complex. Field and petrographic descriptions allowed the identification of a migmatite-gneiss composed essentially of a Hbl+Pl+Qz residue and a Pl+Qz+Cpx+Opx+Hbl leucosome. The opx-bearing leucosome indicates high temperature metamorphism, whereas pervasive Hbl suggests retrogressed conditions under amphibolite facies. The migmatite-gneiss geochemically resemble the low-pressure (LP) to medium-pressure (MP) Tonalite-Trondhjemite-Granodiorite (TTG) suites in their major and trace element signatures. Cathodoluminescence (CL) images show that the cores of both prismatic (igneous)

and rounded (metamorphic) zircons present well-defined oscillatory zoning and homogeneous unzoned overgrowth and recrystallization rims. Besides that, some zircon grains have inclusions of quartz, plagioclase, and rutile. Most of the zircons exhibit cores with magmatic texture and recrystallized rims, which can be interpreted as generated during metamorphic events. Even among those zircons that preserved the prismatic shape, rare were the ones that preserved the magmatic textures beyond their core. The presence of both kinds of textures in the zircons evidence the ocurrence of tectono-magmatic and metamorphic processes within this portion of the São Francisco Craton. This result served as a confirmation for the field, petrographic and whole-rock geochemical observations: an igneous rock that was reworked by high temperature metamorphism (granulite facies). We acquired new LA-ICP-MS U-Pb zircon data which yield rock crystallization ages from 3320 to 3245 Ma, and metamorphic ages from 3099 to 2989 Ma, indicating a Paleoarchaean origin for this terrane. Zircon grains show significantly sub chondritic to chondritic initial ƐHf(t) values (-7.06 to 1.55) and two-stage model ages from 3.53 to 3.76 Ga, which may indicate either the existence of a reworked Eoarchaean to early Paleoarchaean crust or melting of the mantle in this region. The values of the Th/U and Nb/Hf ratios of the zircons (between 0.12 and 2.14 and between 0.0007 and 0.01, respectively) from the migmatite-gneiss indicate that it is associated with an orogenic setting. The obtained results are thus relevant to constrain the composition of the Uauá Block's first continental crust. The Palaeo-to-Mesoarchaean crustal evolution of the Uauá Block can be summarized as follows: a 3320 Ma igneous protolith was reworked on an arc-like setting at 3245 Ma and was submitted to high temperature metamorphism (granulite facies) at 3099 Ma, which was retrogressed to amphibolite facies at 2989 Ma, all that evidenced by field and petrography features, whole-rock geochemistry, zircon textures, U-Pb ages, Hf isotopes and zircon trace elements.

Keywords: Paleoarchean migmatite-gneiss, continental accretion, early arc magmatism, Pb-Hf-REE in zircon, Uauá Block.

4.1. Introduction

The nature of Earth's early crust and the processes that are associated with its formation and evolution are fundamental in the understanding of the origin and differentiation of the continental crust and Earth's mantle, as well as the formation of the first cratons and the beginning of plate tectonics on Earth, so it is widely debated when crustal growth and reworking through arc magmatism first operated on Earth. The oldest known rocks on our planet are essentially orthogneisses that occur in cratons worldwide, within high-grade terranes of Eoarchean age (> 3600 Ma; Condie, 2019). These gneisses are predominantly sodic and belong to the tonalite-trondhjemite-granodiorite (TTG) series, a distinguishing feature of the Archean, and are regarded to have formed at high, medium and low pressures (Moyen, 2011). However, due to the scarce exposure and highly deformed nature of these extremely old rocks, their study is still a topic of great interest to the geosciences (Dey et al., 2017).

So far, the oldest rocks dated in the northern São Francisco Craton are the 3642 Ma Mairi orthogneisses (Oliveira et al., 2020), the 3537 Ma TTG gneisses from the Petrolina region (Werlang, 2020) and the 3420 Ga TTG from the Sete Voltas region (Martin et al., 1997). Thus, this part of the craton has a high potential to allow the understanding of the mechanisms of early crust formation. In this context, the current study reports new petrography, whole-rock geochemistry, zircon U-Pb ages, in-situ Hf isotope data, and zircon trace-elements data for migmatite-gneisses from the Uauá Block, located in the northeastern edge of the São Francisco Craton, which was found to be over 100 Ma older than the current literature suggests. Here we report Archaean rocks that can be best explained to be formed at convergent plate boundaries. Thus, this article has as objective to constrain the Palaeoarchaean crustal evolution of the Uauá Block based on field, petrography, whole-rock geochemistry, zircon textures, LA-ICP-MS U-Pb ages, Lu-Hf isotopes and trace-elements composition.

4.2. Geological setting and field relations

The São Francisco Craton (SFC) (Almeida et al., 1981) (Fig.1) is constituted by distinct Archean granitic-gneissic complexes. In the south, the craton is composed of the Belo Horizonte, Campo Belo, Passa Tempo and Santa Bárbara complexes, composed of TTG rocks, K-rich granitic plutons and migmatites

(Teixeira et al., 2017). Remnants of supracrustal rocks, as well as mafic dykes and layered mafic-ultramafic bodies also occur in the Quadrilátero Ferrífero region (e.g., Machado et al., 1992; Pinese et al., 1995; Teixeira et al., 2000; Alkmim and Noce, 2006; Goulart et al., 2013; Lana et al., 2013; Romano et al., 2013; Teixeira et al., 2017). In the northern portion of the SFC, the Gavião, Serrinha, Uauá, Jequié and Itabuna-Salvador-Curaçá blocks represent the main Archean units, which are comprised of metamorphosed rocks from granulite (TTG terranes) to greenschist facies (supracrustal sequences) (e.g., Barbosa and Sabaté 2002, 2004; Barbosa and Barbosa, 2017; Teixeira et al., 2017). This article focuses on the Uauá Block (UB), located in the northeastern edge of the craton.

The UB is bordered to west by the Archean-Paleoproterozoic Caldeirão Belt, to the east by the Paleoproterozoic Rio Capim Greenstone Belt (Oliveira et al., 2011; 2013) and to the south by the Serrinha Block. Until the present work, the oldest rocks dated in the UB were banded gneisses of 3.15-3.12 Ga (Oliveira et al., 2019). According to these authors, the Mesoarchean gneisses rocks serve as basement to Mesoproterozoic layered anorthosite, peridotite and diorite complexes, pre-metamorphic mafic dykes and tonalite-granodiorite bodies. Neoarchean non-metamorphosed norite-tholeiite dykes crosscut the country rocks in some places (Oliveira, 2011; Oliveira et al., 2013 and references therein). With exception of the Neoarchean noritic (2.73 Ga) and tholeiitic (2.62 Ga) dykes (Oliveira et al., 2013), much of the basement rocks underwent granulite facies metamorphism and were later retrogressed to amphibolite facies (Oliveira et al., 2019). The felsic granulite bodies, with interspersed garnet-bearing mafic granulites, are strongly foliated, frequently with horizontal or south-dipping low-angle foliation (Oliveira et al., 2019). The available isotopic data from the rocks of UB show εNd(t) between -6.6 and +1.6 (e.g. Sato, 1998; Oliveira et al., 1999; Oliveira et al., 2002a). More recently, Oliveira et al., (2019) investigated the 2.82 Ga high-pressure mafic granulites of the Uauá Block and obtained Hf isotopes data suggesting both crustal and juvenile origins for these rocks. Cordani et al., (1999) obtained ages between 3.12 and 3.13 Ga for the Capim tonalite, whereas Oliveira et al., (2010) reported felsic igneous bodies with ages between 3.07 and 2.99 Ga. According to Oliveira et al. (2011, 2013), the younger tholeiitic dyke swarm (2.62 Ga), which crosscuts the gneisses of the basement, may represent a failed arm of a Neoarchaean rift system.

The migmatite-gneiss rocks described here occur in an area located to the south of the town of Uauá. They are composed of a hornblende (Hbl) granodioritic

residue and a Opx-Cpx granodioritic leucosome (Fig. 2a-f). This location was chosen due to the lack of data, as well as because of interesting field features, such as 2.7-2.6 Ga mafic dykes (Oliveira et al., 2013) cutting the orthogneiss banding (Fig. 2c), which makes the Uauá Block one of the few places in the northern SFC in which preserved Archaean deformation was found, making this area an important place for the study of the early crustal evolution of the northern São Francisco Craton, since the Palaeoproterozoic collision did not affect this portion of the UB.

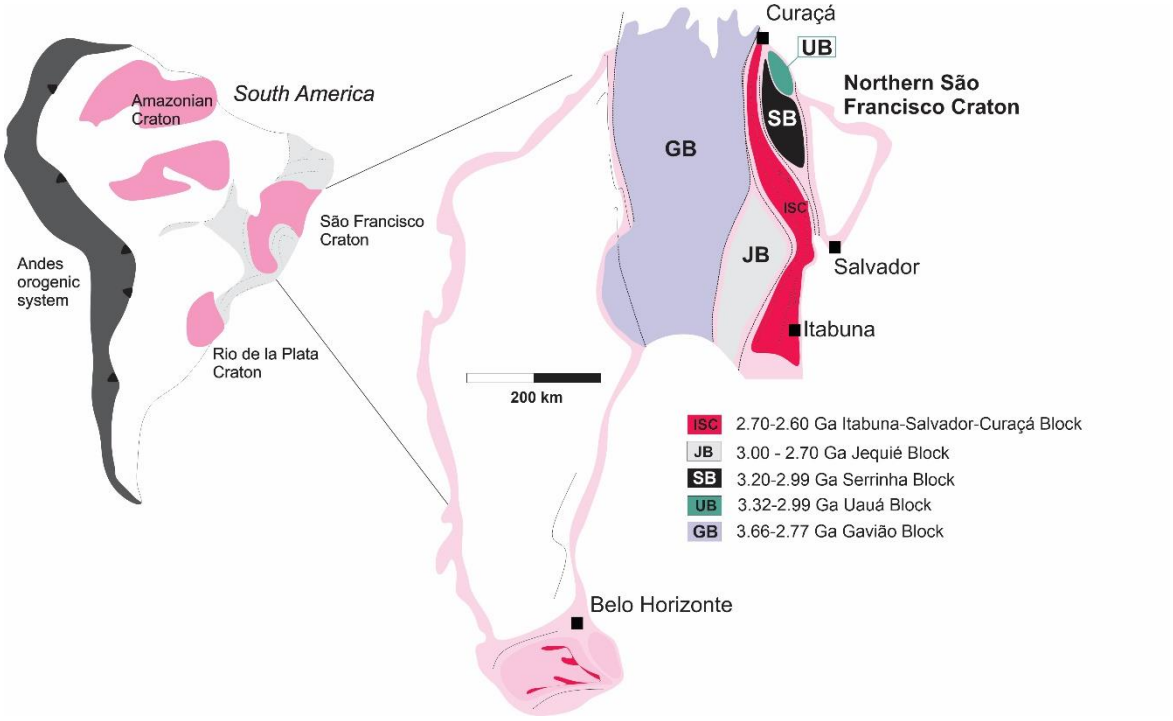

Figure 1 – Simplified geological map of the northern part of the São Francisco Craton. GB – Gavião Block; JB – Jequié Block; ISC – Itabuna-Salvador-Curaçá Block; SB – Serrinha Block; UB – Uauá Block. Modified from Gordilho-Barbosa et al. (2023).

4.3. Results

A detailed description of the analytical methods employed in our research are presented in Supplementary Material S1 (ICP-AES, Q-ICP-MS, LA-MC-ICP-MS). Whole-rock geochemistry data are shown in Supplementary Material S2, representative zircon CL images are in Supplementary Figure 1 and results tables for LA-ICP-MS U-Pb geochronology, Hf isotopes and trace elements in zircon are shown in Supplementary Materials S3, S4 and S5 respectively.

4.3.1. Petrography

The petrographic characterization of the migmatite-gneiss allowed to

determine its mineralogy as well as its fabric elements. The rock's residue is constituted of inequigranular granoblastic texture, with the following paragenesis: hornblende+plagioclase+quartz and small amounts of biotite (Fig. 2c-f) whereas the leucosome is dominated by inequigranular granoblastic texture, with amphibole, plagioclase, and minor amounts of orthopyroxene, clinopyroxene, biotite and quartz (Fig. 2c-f). The clinopyroxene seems to be cutting grains of plagioclase, which suggests that it is related to the high-grade metamorphic event (granulitization) that occurred in this part of the Uauá Block. Zircon, apatite, allanite, rutile, titanite occur as accessories.

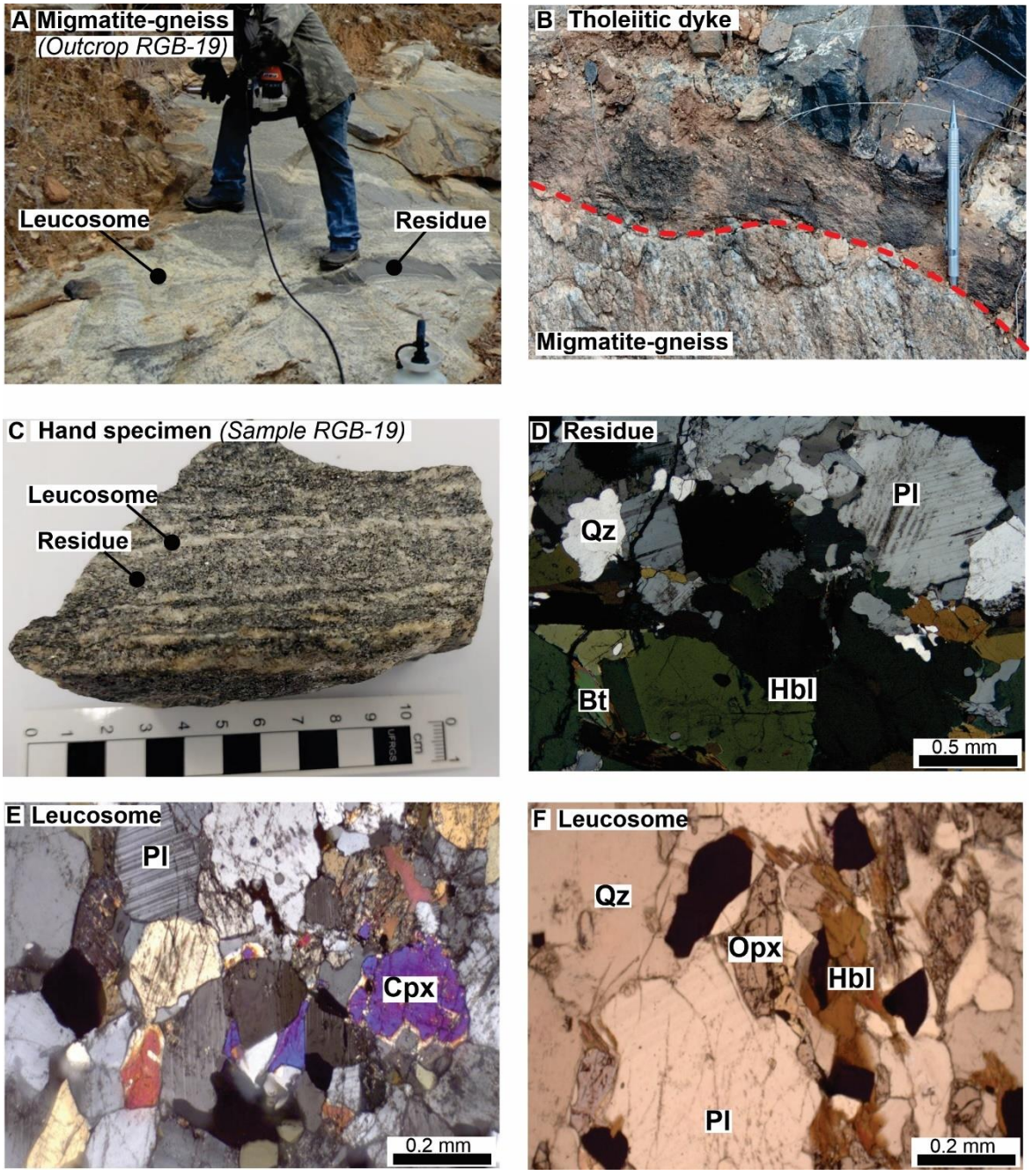

Figure 2 – Field and petrography aspects of the Paleoarchean gneiss of the Uauá Block. A - Outcrop photograph from the migmatite-gneiss showing the hornblende granodioritic residue and the opx-cpx granitic leucosome. B – Outcrop photograph

showing the 2.7-2.6 Ga tholeiitic dyke cutting the migmatite-gneiss banding. C – Hand specimen of the migmatite-gneiss, showing the residue and the leucosome. D – Photomicrograph of the Pl+Hbl residue of the migmatite-gneiss in plane-polarized light. E – Photomicrograph of the Cpx + Pl leucosome. F – Photomicrograph of the Opx + Pl leucosome. Abbreviations of the minerals' names after Whitney and Evans (2010).

4.3.2. Whole-rock geochemistry

Major element composition from the migmatite-gneiss samples (Supplementary Material S2) indicate intermediate (SiO_2 = 64.0-64.7 wt.%) rocks with a sodic affinity, with Na_2O contents ranging from 4.62-4.67 wt.% and Na_2O/K_2O ratios between 3.25 and 4.49, closely matching the Archaean TTG field suggested by Martin et al. (2005) (Fig. 3a). Figure 3b-d show that the migmatite-gneiss has trace elements contents that also suggest its TTG-like composition, while figures 3e, f indicate that it exhibits light rare earth element-enriched (LREE), heavy rare earth element-depleted (HREE) chondrite-normalized patterns (Palme and O'Neill, 2014) with almost no Eu anomaly (Eu/Eu^* = 0.90-0.97) while its primitive mantle-normalized spider diagrams show negative Nb and Ta anomalies.

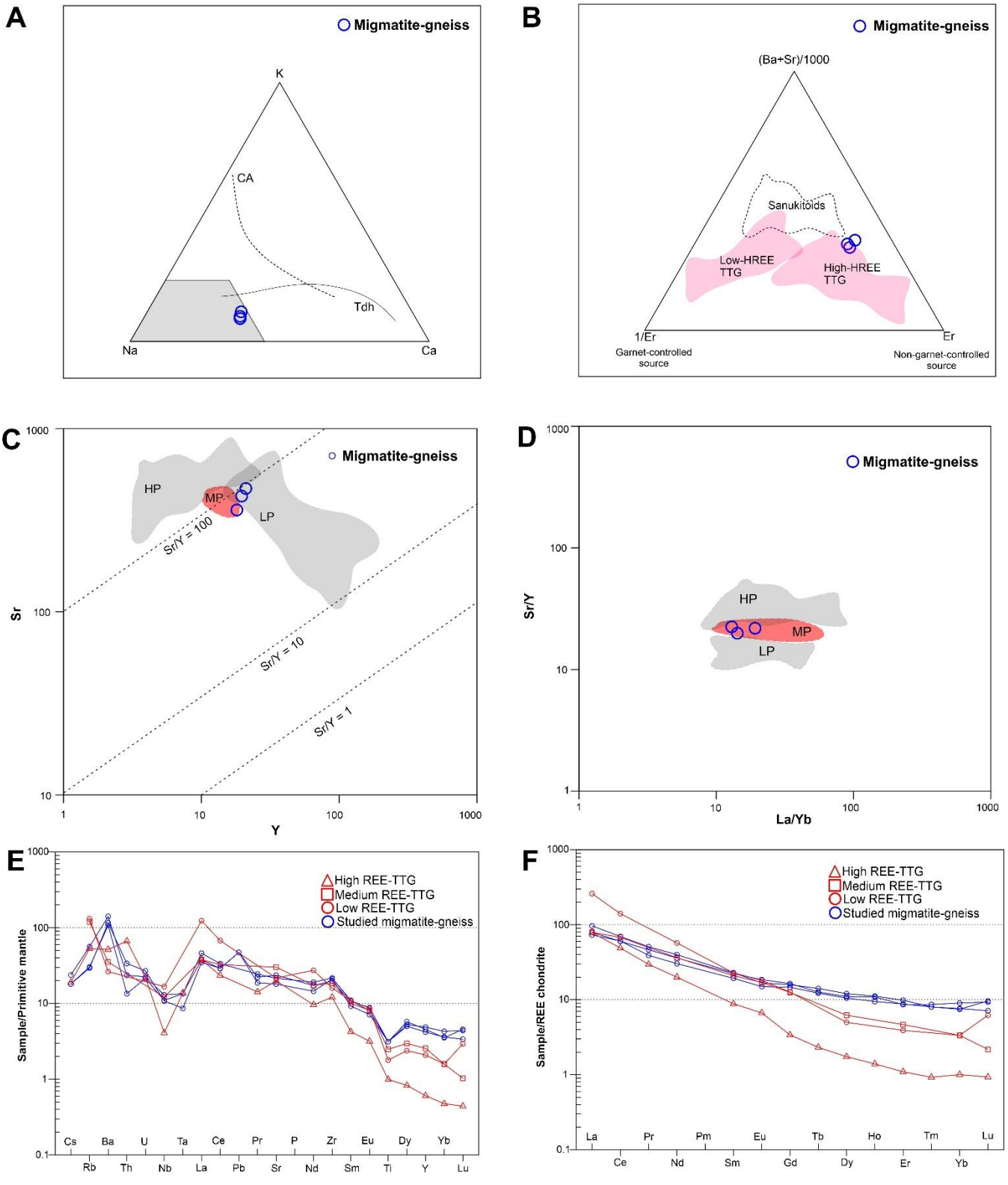

Figure 3 – Geochemical characteristics of the Paleoarchaean Uauá Block migmatite-gneiss. A – Ternary K-Na-Ca diagram showing the calc-alkaline (CA) and trondhjemite (Tdh) trends from Barker and Arth (1976) and the field of Archean

TTGs from Martin et al. (2005). B – Ternary (Ba+Sr)/1000-1/Er-Er diagram to distinguish between TTGs and sanukitoids (after Heilimo et al., 2010). C – Sr vs Y diagram to discriminate the TTG types between high, medium, and low pressure (HP, MP and LP – after Moyen, 2011). D – Sr/Y vs La/Yb plot also distinguishing the TTGs as HP, MP and LP (Moyen, 2011). E – Primitive-mantle normalized (Palme and O'Neill, 2014) trace elements diagram for the Uauá Block migmatite-gneiss compared to high, medium and low HREE TTGs (after Moyen, 2011). F – Chondrite-normalized (Palme and O'Neill, 2014) REE diagram for the Uauá Block migmatite-gneiss compared to high, medium and low HREE TTG types (after Moyen, 2011).

4.3.3. Zircon U-Pb Geochronology

Cathodoluminescence (CL) images of the zircons and location of spots are presented in Supplementary Figure 1, while the zircon U-Pb geochronology data are in Supplementary Material S3.

We divided the zircons into igneous or magmatic and metamorphic due to their external and internal features (e.g. Corfu et al., 2003). Only a few of our zircon grains are doubly terminated prisms or pyramids and are dark in the CL images (Supplementary Fig. 1). They present internal features such as oscillatory zoning and xenocrystic cores, which are typical features of igneous or magmatic zircons (Corfu et al., 2003). Externally, most of our grains show ovoid or rounded shapes and internally, these zircons, which are bright in the CL images, present features such as metamorphic growth zones, preserved igneous cores and recrystallized domains (Hoskin and Schaltegger, 2003). Since our zircons present the aforementioned characteristics, we defined them as metamorphic zircons.

The analyses were performed by LA-SF-ICP-MS and the most concordant of them (< 5% discordance) spread along the concordia and can be grouped in four age clusters (Fig. 4a,b). The oldest cluster contains 9 core analyses, yielding a regression with an upper intercept age of 3320.0 ± 11.9 Ma (MSWD = 2.2; 2s; ρ = 0.11) (Fig. 4c). The second older cluster contains 13 core and rim analyses and yields an upper intercept age of 3244.42 ± 0.25 Ma (MSWD = 9.1; 2s; ρ = 0.84) and a Concordia age of 3245.91 ± 3.09 (n = 7, MSWD = 0.97; 2s; ρ = 0.32) (Fig. 4d). The third one has 12 core and rim analyses, yielding a regression with an upper intercept age of 3105.62 ± 0.16 Ma (MSWD = 6.9; 2s; ρ = 0.43) and a Concordia age of 3099.25 ± 4.29 Ma (n = 9, MSWD = 8.5) (Fig. 4e) and the youngest cluster has 4 rim analyses, which yield an upper intercept age of

2989.74 ± 0.21 (MSWD = 4.7; 2s; ρ = 0.47) (Fig. 4f).

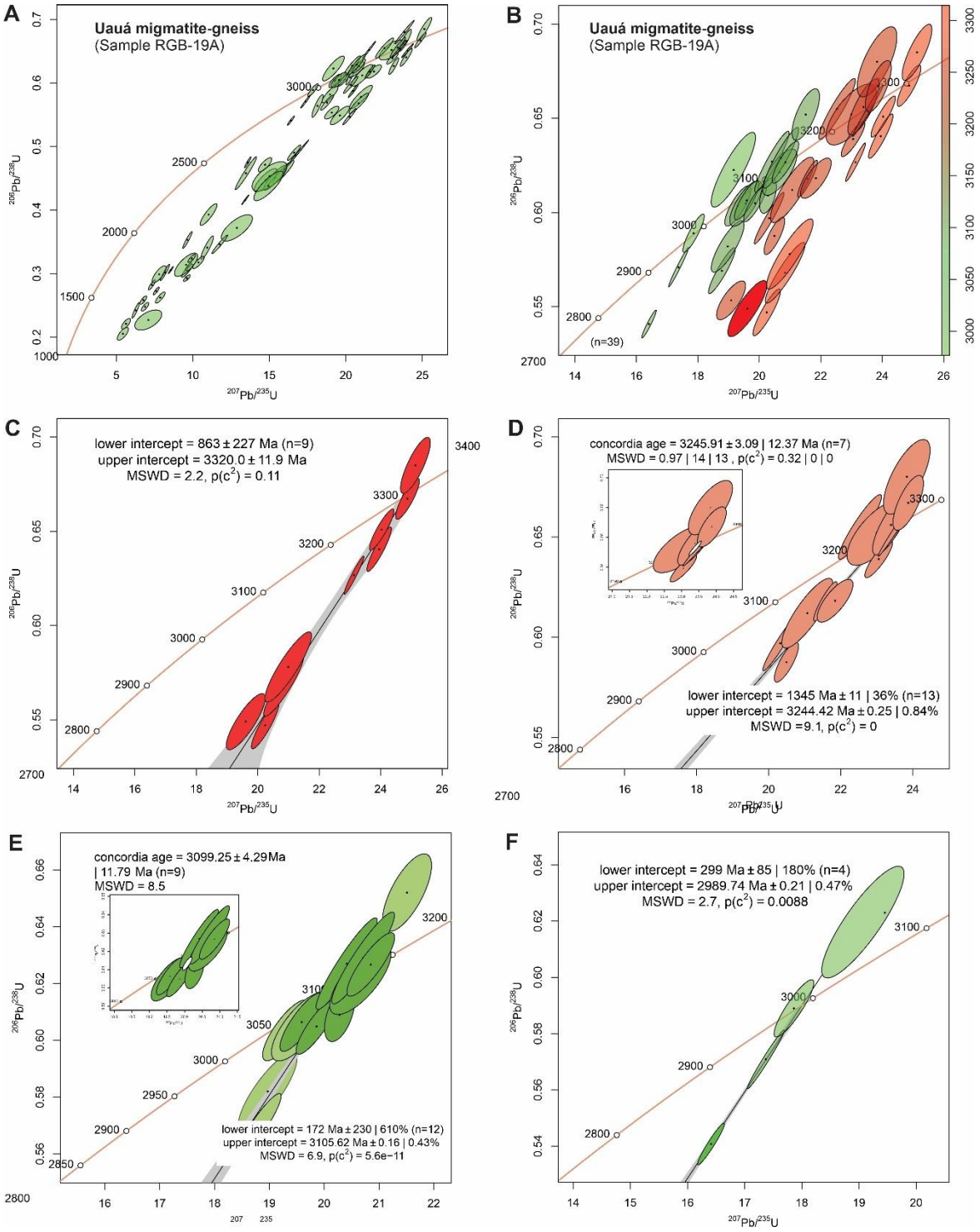

Figure 4 – Zircon U -Pb ages for the Paleoarchaean Uauá Block migmatite-gneiss. A – LA-ICP-MS results showing all the obtained data. B – Concordia diagram showing the most concordant age data for the UB migmatite-gneiss. C – LA-ICP-MS results for the oldest age cluster. D – LA-ICP-MS results and Concordia age for the second older age cluster. E – LA-ICP-MS results and Concordia age for the third age cluster. F – LA-ICP-MS results for the youngest age cluster.

4.3.4. Zircon Lu-Hf isotopes and REE

The zircon Hf isotope data of sample RGB-19A are presented in Supplementary Material S4 and in Figure 5a. The igneous zircons, characterized by oscillatory zoning and dark luminescence on CL images, have $^{207}Pb/^{206}Pb$ ages between 3320 and 3245 Ma and εHf(t) values varying between -4.85 and 1.55, while the metamorphic zircons are characterized by bright luminescence on CL images and by overgrowth features. These zircons have $^{207}Pb/^{206}Pb$ ages between 3099 and 2989 Ma and εHf(t) values varying between -7.06 and -0.39.

A total of twenty-two zircon crystals were analyzed regarding their trace elements content and the zircon geochemistry dataset is shown in supplementary material S5. Most of the magmatic zircons display positive Ce anomalies (15.7 – 78.9 ppm) as well as negative Eu anomalies (Eu/Eu* = 0.28 – 0.46). As shown in figure 5b, the patterns are characterized by a steep slope from the LREE to the HREE with positive Ce and negative Eu anomalies and the magmatic zircons are also characterized by very low La/Lu ratios (0.009-0.07). Most of the metamorphic zircons present depletion in LREE and enrichment in HREE, with slightly positive Ce anomalies and negative Eu anomalies. The metamorphic zircons from the migmatite-gneiss are enriched in all trace-elements when compared with the magmatic groups and their La/Lu ratio is considerably higher than that of the magmatic zircons, varying from 0.20 to 2.22 (Fig. 5c-f).

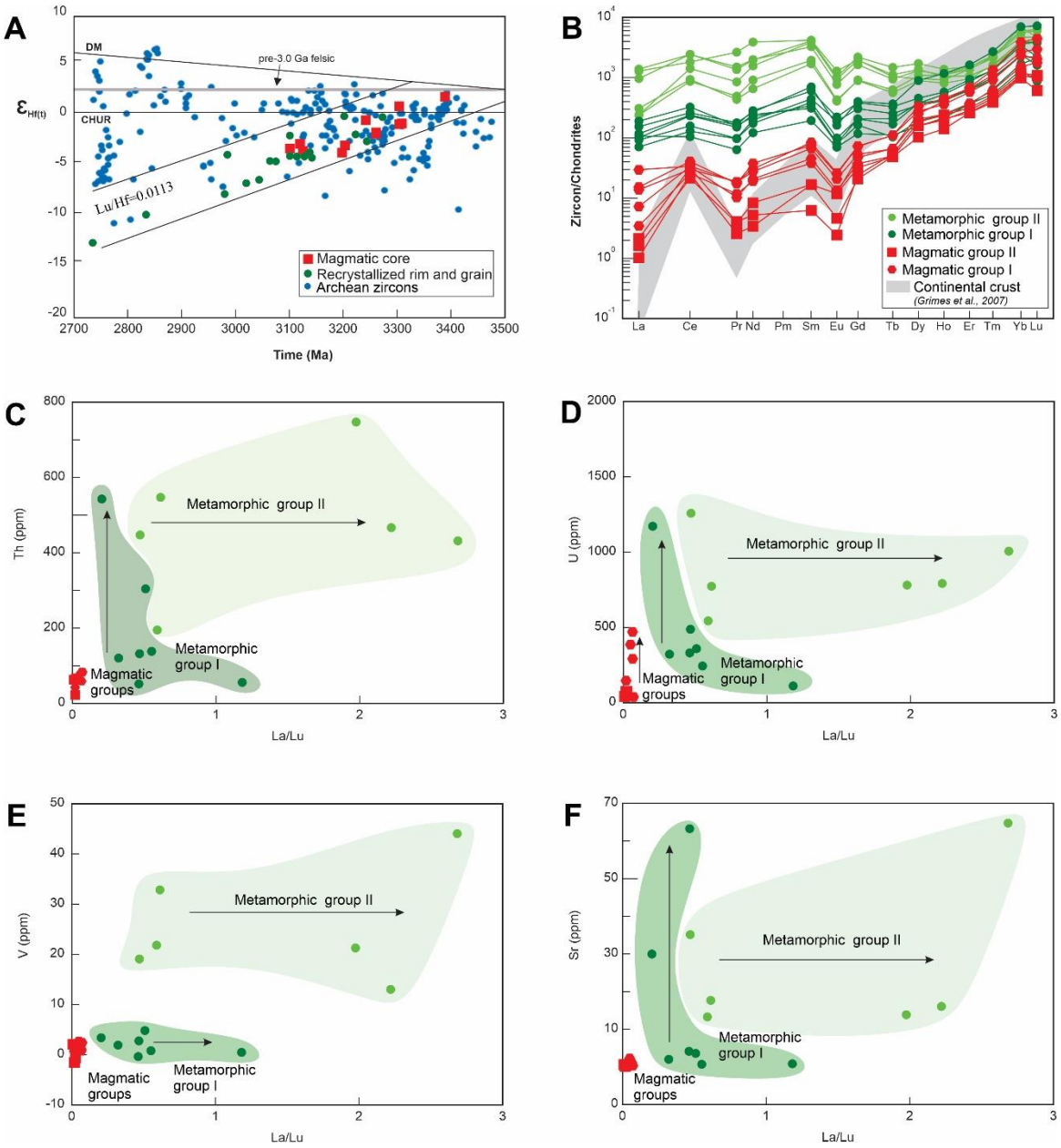

Figure 5 – Lu-Hf isotopes and zircon trace elements diagrams for the migmatite-gneiss of the Uauá Block. A – εHf(t) vs age diagram for the UB migmatite-gneiss. The blue dots represent the Archaean zircons data compiled from Maltese et al. (2021). DM – depleted mantle; CHUR – Chondritic Uniform Reservoir (chondritic mantle). B – Chondrite-normalized REE patterns (Palme and O'Neill, 2014) of zircons from the Uauá Block orthogneiss. Both groups (magmatic and metamorphic) have positive Ce and negative Eu anomalies. The grey field represents the pattern of the continental crust defined by Grimes et al. (2007). C-F – Binary zircon trace elements diagrams showing that the magmatic zircons have La/Lu ratio < 0.1 and smaller concentrations of trace elements than the metamorphic ones.

4.4. Discussion

4.4.1. Crustal origin

The Archean continental crust is normally composed by different rock types, such as grey gneisses and Na-rich granitoids a and a maximum of 50% of it comprises rocks that fit into the so-called tonalite-trondhjemite-granodiorite (TTG) series (e.g. Moyen, 2011). The Uauá Block orthogneiss samples yield Na2O, Fe2O3+MgO+MnO+TiO2 and K2O/Na2O values (Supplementary Material S2) that are characteristic of TTG suites (e.g. Moyen, 2011; Moyen and Martin, 2012). Noteworthy, the samples plot in the TTG field of the ternary K-Na-Ca diagram (Martin, 1994) (Fig. 3a). In addition, The UB orthogneiss-migmatite samples show LREE enrichment and HREE impoverishment such as TTG rocks (Martin, 1994) (Fig. 3e, f).

Moyen (2011) defined three types of TTGs based on the pressure of their genetic tectonic setting, the so-called low (LP), medium (MP) and high pressures (HP) TTGs. This author defined these types based on the contents of incompatible trace elements such as Sr and Y, which occurrence reflect the presence of residual mineral phases during the partial melting process. The HP TTGs are formed in settings which pressure is above 20 kbar (i.e. “hot” subduction zones, similar to modern adakite formation zones, Martin et al., 2014), the MP TTGs are related to settings with pressure around 15 kbar (i.e. the initial stages of a continental collision, Moyen, 2011) and the LP TTGs are generated in settings with pressures below 10 kbar (i.e. orogen collapse post-collisional settings or the base of oceanic plateaus, Moyen, 2011). The studied migmatite-gneiss has geochemical characteristics similar to LP-and-MP TTGs, such as: i) Sr content ranging between 359.34 and 471.00 ppm; ii) Y content between 18.08 and 21.00 ppm; and iii) Sr/Y ratios between 19.88 and 22.43 (Fig. 3) (Supplementary Material S2).

4.4.2. Zircon archive of continent formation through time

Internally, the igneous zircons are characterized by oscillatory zoning as well as by the presence of xenocrystic cores, which are typical features of this kind of zircon (Corfu et al., 2003). Only a few of our zircons have these characteristics, which allow us to define them as igneous or magmatic zircons. In contrast, according to Hoskin and Schaltegger (2003), zircons from low-grade metamorphic rocks are usually inherited from their protolith and may show signs

of resorption or metamorphic overgrowth. High-grade metamorphic rocks such as granulites may contain zircon that grew during metamorphism, associated or not with the presence of an anatectic melt (Fraser et al., 1997, Roberts and Finger, 1997).

Externally, metamorphic zircons show ovoid or rounded shapes, which are interpreted to be formed by resorption by a zircon-undersaturated intergranular fluid (Hoskin and Black, 2000). Internally, these zircons present features such as metamorphic growth zones, preserved igneous cores and recrystallized domains (Hoskin and Schaltegger, 2003). Most of our zircons present the aforementioned characteristics, which led us to define them as metamorphic zircons. The studied zircons were dated via LA-ICP-MS and the obtained U-Pb ages varied between ca. 3320 Ma and ca. 2989 Ma and the igneous and metamorphic zircons presented distinct ages. Our igneous zircons presented ages between ca. 3320 and ca. 3245 Ma, obtained in their cores, with younger ages (mostly between ca. 3140 and ca. 3060 Ma) obtained in their rims. The metamorphic ones presented ages between ca. 3099 and ca. 2989 Ma, in both cores and rims, which is consistent with the regional magmatic and metamorphic history. Also, the igneous zircons have εHf(t) values varying between -4.85 and 1.55, while the metamorphic ones have $^{207}Pb/^{206}Pb$ ages between 3099 and 2989 Ma and εHf(t) values varying between -7.06 and -0.39.

4.4.3. Magmatism and metamorphism constraints

The Palaeoarchaean ages (ca. 3300-3244 Ma) for the Uauá Block migmatite-gneiss indicate that it is the block's oldest rock so far. Even older rocks might be found in the region as evidenced by two-stage zircon Hf model ages between 3530 and 3760 Ma.

The UB comprises NW-trending banded gneisses of Palaeoarchaean age that served as basement to layered anorthosite, peridotite and diorite complexes, and tonalite-granodiorite plutons (e.g., Oliveira et al., 1999). These rocks recorded at least two metamorphic events, with the first occurring under granulite-facies conditions and being later overprinted by the second event, associated with amphibolite facies retrograde metamorphism (e.g., Oliveira et al., 1999; 2013;2019). This is consistent with our data since we obtained ages between ca. 3099 and 2989 Ma in the rims of the metamorphic zircons.

A whole-rock Pb-Pb age of 3161 ± 65 Ma was obtained for an anorthosite layer (Paixão and Oliveira, 1998) and slightly younger U-Pb zircon ages between

3130 and 3120 Ma are associated with the Capim tonalite (e.g., Cordani et al., 1999). The zircon LA-ICP-MS U-Pb ages obtained for the UB orthogneiss in our work (ca. 3302 to 3244 Ma) confirm that the basement of the block is older than these events. At the same time, an orogenic metasedimentary sequence (i.e., Caldeirão belt) formed by quartzites, sillimanite-cordierite-garnet gneisses, granodioritic orthogneisses, mafic rocks and migmatites, accretioned to the west of the Uauá Block, recording amphibolite facies conditions at ~3150 Ma (e.g., zircon U-Pb; Oliveira et al., 2002a). After this timespan (~3161 to 3120 Ma) characterized by magmatism in the Uauá Block, high-temperature metamorphism, related to granulite rocks of 207Pb/206Pb zircon age of 3072 ± 20 Ma, occurred in the UB (e.g., Paixão and Oliveira, 1998). This is consistent with the ca. 3105-2989 Ga ages we found in the rims of the zircons of the UB orthogneiss. Lastly, orthopyroxene-bearing granulite and gneissic granodiorite leucosome veins and small plutons, mainly in the southeast of Uauá, were respectively dated (U-Pb zircon) at 2933±3 Ma and 2991±22 Ma (e.g., Oliveira et al., 2002a). Therefore, 3072 ± 20 to 2933 ± 3 Ma can be interpreted as a period of high-temperature metamorphism and partial melting of older crust in the Uauá Block.

Our data indicate ca. 3320 Ma as the crystallization age of the gneiss protolith, at 3245 Ma a magmatic event reworked the 3320 Ma protolith. The younger ages (ca. 3099 and ca. 2989 Ma) might be related to Pb loss due to a local or regional event (e.g., regional high-grade metamorphism or emplacement of other igneous bodies between ca. 3150 and ca. 2820 Ma).

4.4.4. Considerations on the sources of the orthogneiss

According to Moyen and Martin (2012), the Archaean continental crust is dominated by TTGs, and these rocks differ in mineralogy and chemical composition from post-Archaean granitoids. These differences may suggest that TTGs were generated in tectonic environments that are unique to the Archaean (e.g. Maltese et al., 2021). Thus, constraining the petrogenesis and sources of the TTGs is fundamental to addressing this issue and Lu-Hf systematics can be used to investigate it.

Worldwide, the majority of the initial εHf values of Archaean zircon range between about -10 and +2, with a median of -0.9 about 3.0 Ga (median of ~270 analyses, e.g. Maltese et al., 2021 and references therein). The data obtained for the Uauá Block are consistent with the global record, lying closer to both the

primitive-mantle and crustal compositions, which can be interpreted by different petrogenetic models such as: i) derivation of TTGs from parent-melts related to primitive-mantle slightly super chondritic Hf isotopic compositions and ii) derivation of TTGs from parental-melts associated with crustal sub-chondritic Hf isotopic compositions.

Since Hf partitions preferentially into the melts when compared to Lu, crustal materials tend to evolve with a sub-chondritic Lu/Hf ratio, developing less radiogenic Hf over time when compared with the bulk-silicate Earth (BSE) (Maltese et al., 2021). Negative εHf(t) values may indicate reworking of older crust (e.g. Zeh et al., 2009), long-lived interactions between crust and enriched-mantle sources (e.g. Laurent and Zeh, 2015) or mixing of melts derived from an older crust and a near-primitive mantle (e.g. Kröner et al., 2013a;2014, Bauer et al., 2017).

The data obtained in our study also reveal the definition of an array that trends towards negative εHf(t) values with the decrease of the ages and that the oldest samples, of Palaeoarchaean age (ca. 3320 Ma), have super-chondritic Hf isotopic compositions, which is consistent with the global distribution (Fig. 5a). The slope of the array is consistent with a 176Lu/177Hf ratio of 0.0113, which is typical of the average continental crust (e.g. Taylor and McLennan, 1985; Wedepohl, 1995), suggesting that the Uauá Block orthogneiss formed by reworking of an older crust. This is corroborated by our Hf model ages between 3.76 and 3.53 Ga, which indicate the presence of an Eoarchean to early Paleoarchean crust in the UB.

4.4.5. Palaeoarchaean tectonic setting

Continental arc zircons have U/Yb ratios mostly between 0.1 and 4.0, with higher values possibly indicating a great influence from mature, large-ion lithophile (LIL)-enriched crust during the formation of the parental melts (Grimes et al., 2015). The zircons from our study have U/Yb ratios between 0.22 and 1.33 (mostly between 0.59 and 1.04), suggesting that they can be either related to primitive arcs or to lower and upper continental crust (Fig. 5b). High contents of U relative to Th (Th/U ratios) are features of zircons that crystallized from magma at low temperatures (e.g. Gagnevin et al., 2010; Wang et al., 2011). Igneous zircons have Th/U ratios between 0.2 and 4.0 (Hoskin and Schaltegger, 2003) and metamorphic zircons have Th/U ratios lower than 0.07 (Rubatto, 2002).

According to Grimes et al. (2015), petrogenetic-based proxies such as Th-Nb

become more effective when normalized to the least incompatible element (Yb), aiding on the visualization of deviations from the respective elements in different tectonic settings. For zircon-based proxies U is preferred over Th due to its capacity of providing a greater separation between geochemical fields for different tectono-magmatic settings. According to Moyen and Laurent (2018), the occurrence of LP and MP TTGs precedes that of HP TTGs and the studied migmatite-gneiss confirms this tendency (Fig. 6a). Figure 6b illustrates the Th/U vs Nb/Hf diagram for the zircons of the UB migmatite-gneiss and shows that it is associated with an orogenic tectonic setting.

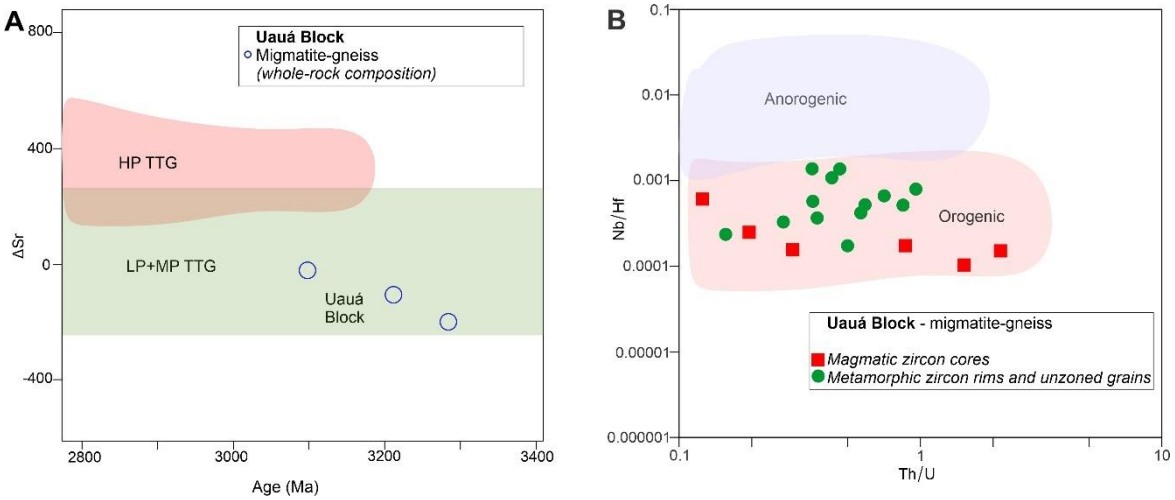

Figure 6 – Binary diagrams. A – Time composition diagram for the Palaeoarchaean Uauá Block migmatite-gneiss showing the TTG types of Moyen and Laurent (2018). LP – low pressure TTG, MP – médium pressure TTG, HP – high pressure TTG. B – Nb/Hf vs Th/U diagram showing that most of the zircons from the Uauá Block migmatite-gneiss are related to orogenic settings, suggesting the occurence of collisional tectonics within the UB since the Palaeoarchaean.

4.6. Conclusions

Research was conducted in the Uauá Block, northeastern edge of the São Francisco Craton, Brazil, in order to investigate the petrogenesis of an migmatite-gneiss that is part of the block's basement, at the Uauá Complex. Thus, it is possible to conclude that:

(1) Field and petrographic descriptions allowed the identification of a migmatite-gneiss composed essentially of a Hbl+Pl+Qz residue and a Pl+Qz+Cpx+Opx+Hbl leucosome. The opx-bearing leucosome indicates high temperature metamorphism, whereas pervasive Hbl suggests retrogressed conditions under amphibolite facies.

(2) The migmatite-gneiss geochemically resemble the low-pressure (LP) to medium-pressure (MP) Tonalite-Trondhjemite-Granodiorite (TTG) suites in their major and trace element signatures.

(3) Cathodoluminescence (CL) images show that the cores of both igneous and metamorphic zircons present well-defined oscillatory zoning and homogeneous unzoned overgrowth and recrystallization rims and the presence of both kinds of textures in the zircons evidence the occurrence of tectono-magmatic and metamorphic processes within this portion of the São Francisco Craton.

(4) LA-ICP-MS U-Pb zircon data which yield rock crystallization ages from 3320 to 3245 Ma, and metamorphic ages from 3099 to 2989 Ma, indicating a Palaeoarchaean origin for this terrane and Mesoarchaean granulitization and retrograde metamorphism.

(5) Zircon grains show significantly sub chondritic to chondritic initial ƐHf(t) values (-7.06 to 1.55) and two-stage model ages from 3.53 to 3.76 Ga, which may indicate either the existence of a reworked Eoarchaean to early Palaeoarchaean crust or melting of the mantle in this region.

(6) The values of the Th/U and Nb/Hf ratios of the zircons (between 0.12 and 2.14 and between 0.0007 and 0.01, respectively) from the migmatite-gneiss indicate that it is associated with an orogenic setting.

The Palaeo-to-Mesoarchaean crustal evolution of the Uauá Block can be summarized as follows: a 3320 Ma igneous protolith was reworked in an arc-like setting at 3245 Ma and was submitted to high temperature metamorphism (granulite facies) at 3099 Ma, which was then retrogressed to amphibolite facies at 2989 Ma and all that is evidenced by field and petrography features, whole-rock geochemistry, zircon textures, U-Pb ages, Hf isotopes and zircon trace elements.

Acknowledgements

Gordilho-Barbosa, R. would like to thank Coordenação de Aperfeiçoamento de Pessoal de Nível Superior – CAPES for financial support (Ph.D. scholarship – proc. 88887.484774/2020-00 and sandwich-Ph.D. scholarship – proc. 88887.696441/2022-00) and SEG Canada Foundation (SEGCF) for a student research grant (SRG 21-40). Leitzke, F.P. would like to thank Fundação de Amparo à Pesquisa do Estado do Rio Grande do Sul – FAPERGS for a young doctor grant (proc. 21/2551-0000742-7) and Conselho Nacional de

Desenvolvimento Científico e Tecnológico – CNPq for a Universal Project grant (proc. 403740/2021-5). Barbosa, J.S.F. would like to thank CNPq for a research productivity grant (proc. 303508/2019-1). This article is dedicated to the memory of Prof. Hervé Martin, from Université Clermont-Auvergne, a great reference to all those studying the crustal evolution of Archean terranes.

5. Conclusão

No Paleo e Mesoarqueano, os dados geológicos, sobretudo os geocronológicos indicam que, antes do Neoarqueano, o BG, o BS e o BU estavam unidos, formando um bloco único. Assim, no BG, interpreta-se que houveram três etapas de produção de TTG, conforme as faixas de idades de 3642-3529 (Oliveira et al., 2020; Werlang, 2020), 3403-3378 (Bastos Leal et al., 2003) e 3259-3240 Ma (Santos Pinto et al., 2012), todas essas idades obtidas pelo método U-Pb em zircão. Considera-se que esses TTGs foram gerados pela subducção de crosta oceânica, ou de platôs oceânicos e/ou de basaltos de arcos de ilhas, hidratados, onde os processos predominantes tiveram idades variando entre o final do Paleo e todo o Mesoarqueano.

Pertencentes ao chamado “Mar de Basaltos” toleíiticos do início da formação da Terra (Martin et al., 2010; Moyen e Martin, 2012), partes dessas crostas oceânicas, ao se resfriarem ficaram mais pesadas e afundaram em relação às partes mais quentes. Ajudado pelas correntes de convecção do Manto, surgiram as primeiras zonas de subducção e, como produto dessa fusão, os primeiros TTG1. Esses cicatrizaram as zonas de subducção deixando ao lado dessas faixas de TTG1, restos do material oceânico e seus sedimentos de fundo, parcialmente subductados. Configuraram-se assim os primeiros GB1. Esses processos tectônicos e de fusão mantélica onde, em alguns casos, os magmas básicos evoluíram até dacitos se repetiram ao longo do Mesoarqueano, formando novas gerações de TTG e GB. Ainda no BG, identificou-se a nucleação de no mínimo mais duas gerações de crosta continental: TTG2, TTG3 e GB2, GB3 formadas no intervalo de 150-200 Ma.

Verifica-se que os dados isotópicos indicam a predominância de valores negativos de εNd(t) e valores de TDM entre 3,4 e 4,2 Ga para as rochas TTGs do BG, cujas idades variam de 3642 a 3259 Ma, o que sugere retrabalhamento de crosta hadeana a paleoarqueana neste Bloco. Também ocorrem, embora em menor proporção, valores positivos de εNd(t), o que sugere a ocorrência de processos juvenis na região. Neste Bloco, os valores de εHf(t) compilados vão

ao encontro dos dados de Nd. Já para os TTGs mesoarqueanos dos Blocos Serrinha e Uauá, cujas idades variam entre 3150 e 2983 Ma, verificou-se uma relativa predominância de valores positivos de εNd(t) e valores de TDM entre 3,0 e 3,3 Ga, o que sugere que a origem destes segmentos crustais está relacionada a processos de natureza juvenil, embora ocorram, também valores negativos associados a retrabalhamento crustal.

Especificamente no caso do Bloco Uauá, os novos dados de geocronologia U-Pb obtidos, isto é, as idades de 3320 Ma e 3245 Ma para os zircões ígneos, indicam que ele é cerca de 100 a 150 milhões de anos mais velho do que o que foi previamente mostrado pela literatura. Os dados também permitiram indicar que a origem destas rochas de idade paleoarqueana está associada a um ambiente colisional no qual houve retrabalhamento de uma crosta mais antiga. Também se verificou a ocorrência de um evento metamórfico de idade mesoarqueana (3099 Ma) , em condições de fácies granulito, que foi posteriormente retrogradado pro fácies anfibolito em 2989 Ma.

6. Referências

Alkmim, F.F., Brito Neves, B.B., Alves, J.A.C. 1993. Arcabouço tectônico do Cráton do São Francisco: uma revisão. In: Misi, A., Dominguez, J.M.L. (eds). O Cráton do São Francisco. Salvador, SBG, 45-62.

Alkmim, F.F., Noce, C.M. 2006. Outline of the geology of Quadrilátero Ferrífero. In: Alkmim, F.F., Noce, C.M. (eds) The Paleoproterozoic Record of São Francisco Craton. IGCP 509 Field Workshop, Bahia and Minas Gerais. Field Guide and Abstracts, 37–73.

Almeida, F.F.M., Brito Neves, B.B., Fuck, R., 1981. Brazilian structural provinces: an introduction. Earth Science Reviews 17, 1–29.

Barbosa, J.S.F., Barbosa, R.G. 2017. The Paleoproterozoic Eastern Bahia Orogenic Domain. In: Heilbron, M.; Cordani, U.G.; Alkmim, F.F. (Eds.). São Francsico Craton, Eastern Brazil. Tectonic Genealogy of a Miniature Continent. Mumbai, India. Springer, (Regional Geology Reviews).

Barbosa, J.S.F., Cruz, S.C.P., Souza, J.S., 2012. Terrenos Metamórficos do embasamento. In: Barbosa, J.S.F., Mascarenhas, J.F., Correa Gomes, L.C., Dominguez, J.M.L., Souza, J.S. (Eds.), CBPM-Companhia Baiana de Pesquisa Mineral, 1 ed. Geologia da Bahia. Pesquisa e Atualização, Salvador, pp. 101–201.

Barbosa, J.S.F., Luciano, R.L., Cruz Filho, B.E., Santana, J.S, Moraes, A.M.V. 2020. Mapa tectônico-geocronológico da Bahia – implicações metalogenéticas. CBPM-CPRM. 1 Mapa. Escala: 1:1.000.000.

Barbosa, J.S.F., Luciano, R.L., Cruz Filho, B.E., Santana, J.S, Gordilho Barbosa, R., Moraes, A.M.V. 2021. Ambientes tectônicos e metalogênese arqueana no Cráton do São Francisco, Bahia. In: Anais do 50º Congresso Brasileiro de Geologia. Brasília, 928p.

Barbosa, J.S.F., Luciano, R.L., Cruz Filho, B.E., Santana, J.S, Moraes, A.M.V. 2021. Mapa tectônico-geocronológico da Bahia – implicações metalogenéticas. Escala 1:1.000.000 Nota Explicativa. CBPM-CPRM, Série Publicações Especiais 24, 54p.

Barbosa, J.S.F., Sabaté, P. 2002. Geological and Geochronological Features and the Paleoproterozoic Collision of The Four Archean Crustal Segments of The São Francisco Craton, Bahia, Brazil. Revista da Academia Brasileira de Ciências. 74(2):343-359.

Barbosa, J.S.F., Sabaté, P. 2004. Archean and Paleoproterozoic crust of the

São Francisco Craton, Bahia, Brazil: geodynamic features. Precambrian Research 133: 1-27.

Barbosa, N.S., Teixeira, W., Bastos-Leal, L.R., Menezes Leal, A.B., 2013. Evolução crustal do setor Ocidental do Bloco Arqueano Gavião, Cráton do São Francisco, com base em evidências U-Pb, Sm-Nd e Rb-Sr. Revista Geologia USP. Série Científica 4, 63–88.

Barbosa, N.S., Leal, A.B.M., Debruyne, D., Leal, L.R.B., Barbosa, N.S., Marinho, M.M., Mercês, L., Barbosa, J.S.F., Koproski, L.M. 2020. Paleoarchean to Paleoproterozoic crustal Evolution in the Guanambi-Correntina Block (GCB), north São Francisco Craton, Brazil, unraveled by U-Pb geochronology, Nd-Sr isotopes and geochemical constraints. Precambrian Research 340: 1-16.

Barker, F., Arth, J.G. 1976. Generation of trondhjemitic-tonalitic liquids and Archean bimodal trondhjemite-basalt suites. Geology 4, 596–600. https://doi.org/10.1130/ 0091-7613(1976)4<596:GOTLAA>2.0.CO;2.

Bastos Leal, L.R., Cunha, J.C., Cordani, U.G., Teixeira, W., Nutman, A.P., Leal, A.B.M., Macambira, M.J.B. 2003. SHRIMP U-Pb, 207Pb/206Pb zircon dating, and Nd isotopic signature of the Umburanas greenstone belt, northern São Francisco craton, Brazil. Journal of South American Earth Sciences. 15(7), 775-785.

Bauer, A.M., Fisher, C.M., Vervoort, J.D., Bowring, S.A. 2017. Coupled zircon Lu–Hf and U–Pb isotopic analyses of the oldest terrestrial crust, the >4.03 Ga Acasta Gneiss Complex. Earth and Planetary Sciences Letters 458, 37–48. https://doi.org/10.1016/j.epsl.2016.10.036.

Brito, R.S.C., 2000. Geologia e petrologia do sill máfico-ultramáfico do Rio Jacaré, Bahia e estudo das mineralizações de Fe-Ti-V e platinóides associadas. [Ph.D. thesis]: Brasília, University of Brasília, 90p.

Chaudhuri, T., 2020. A review of Hadean to Neoarchean crust generation in the Singhbhum Craton, India and possible connection with Pilbara Craton, Australia: The geochronological perspective. Earth-Science Reviews 202, 103085. https://doi.org/10.1016/j.earscirev.2020.103085.

Condie, K.C. 1989. Origin of the Earth's crust. Palaeogeography, Palaeoclimatology, Palaeoecology (Global and Planetary Change Section) 75, 57–81.

Condie, K. C. 2019. Earth's oldest rocks and minerals. In: M. J. Van Kranendonk, V. C. Bennett, & J. Elis Hoffmann (Eds.), Earth's oldest rocks (2nd ed., pp. 239–253). Amsterdam: Elsevier, Chapter 11.

Cordani, U.G., Sato, K., Marinho, M.M. 1985. The geologic evolution of the

ancient granite-greenstone terrane of central-southern Bahia, Brazil. Precambrian Research 27, 187–213.

Cordani, U.G., Sato, K., Nutman, A.P. 1999. Single zircon SHRIMP determination from Archean tonalitic rocks near Uauá, Brazil. II SSAGI - South American Symposium on Isotope Geology Actas, 27–30.

Corfu, F., Hanchar, J.M., Hoskin, P.W.O., Kinny, P. 2003. Atlas of zircon textures. In: Hanchar, J.M., Hoskin, P.W.O. (eds). Zircon. Reviews in Mineralogy and Geochemistry 53, 27-62. Mineralogical Society of America, Washington, D.C.

Cruz, S.C.P., Peucat, J.J., Teixeira, L., Carneiro, M.A., Martins, A.A.M., Santana, J.S., Souza, J.S., Barbosa, J.S.F., Leal, A.B.M., Dantas, E., Pimentel, M. 2012. The Caraguataí syenitic suite, a ca. 2.7 Ga-old alkaline magmatism (petrology, geochemistry and U-Pb zircon ages). Southern Gavião Block (São Francisco Craton), Brazil. Journal of South American Earth Sciences 37, 95-112.

Dantas, E.L., Brito Neves B.B., Fuck, R.A. 2010. Looking for the oldest rocks of South America: Paleoarchean orthogneiss of the Sobradinho Block, northernmost foreland of the São Francisco Craton, Petrolina, Pernambuco, Brazil. VII SSAGI South Am Symp Isotope Geology, S0136.

Dantas, E.L., Brito Neves, B.B., Fuck, R.A. 2013. Looking for the Early Archean rocks in South America: U–Pb dating and Hf isotopes in zircons from the north São Francisco Craton, Brazil. Geol Soc Amer, Annual Meeting 2013, Paper 269-5.

De Brito, M.M., Evers, M. 2016. Multi-criteria decision-making for flood risk management: a survey of the current state of the art. Natural Hazards Earth Systems Science 16, 1019-1033. https://doi.org/10.5194/nhess-16-1019-2016

Dey, S., Topno, A., Liu, Y., & Zong, K. 2017. Generation and evolution of Palaeoarchaean continental crust in the central part of the Singhbhum craton, eastern India. Precambrian Research, 298, 268-291. DOI: https://doi.org/10.1016/j.precamres.2017.06.009

Ferreira, A.C.D., Dantas, E.L., Fuck, R.A., 2021. The previously missing c. 2.9 Ga high-K continental crust in West Gondwana revealed in Northeast Brazil. Terra Nova 33, 184–194. https://doi.org/10.1111/ter.12504

Fraser, G., Ellis, D., Eggins, S. 1997. Zirconium abundance in granulite-facies minerals, with implications for zircon geochronology in high-grade rocks. Geology 25, 607-610.

Gagnevin, D., Daly, J.S., Kronz, A. 2010. Zircon Texture and Chemical Composition as a Guide to Magmatic Processes and Mixing in a Granitic

Environment and Coeval Volcanic System. Contributions to Mineralogy and Petrology 159, 579-596. https://doi.org/10.1007/s00410-009-0443-0

Gardiner, N.J., Mulder, J.A., Kirkland, C.L., Johnson, T.E., Nebel, O., 2021. Palaeoarchaean TTGs of the Pilbara and Kaapvaal cratons compared; an early Vaalbara supercraton evaluated. South African Journal of Geology 124, 37–52. https://doi.org/10.25131/sajg.124.0010

Gordilho Barbosa, R., Lana, C.C., Zincone, S.A. 2021. Paleoproterozoic granitic magmatism in the northern São Francisco Craton, NE Brazil: New perspectives from geochemistry, U-Pb geochronology and Hf isotopes. Journal of South American Earth Sciences 105, 103004. https://doi.org/10.1016/j.jsames.2020.103004

Gordilho Barbosa, R., Ferreira, A.C.D., Leitzke, F.P., Santos, T.N., Conceição, R.V., Martin, H. 2023. A review of 3.66 to 2.77 Ga crustal differentiation in the northern São Francisco Craton, Brazil. International Geology Review 65 (9), 1541-1557. DOI: https://doi.org/10.1080/00206814.2022.2098542

Goulart, L.E.A., Carneiro, M.A., Endo, I., Suita, M.T.F. 2013. New evidence of Neoarchean crustal growth in southern São Francisco Craton: the Carmópolis de Minas Layered Suite, Minas Gerais, Brazil. Brazilian Journal of Geology 43(3), 445–459.

Grimes, C.B., John, B.E., Kelemen, P., Mazdab, F., Wooden, J., Cheadle, M.J., Hanghøj, K., Schwartz, J.J. 2007. Trace element chemistry of zircons from oceanic crust: a method for distinguishing detrital zircon provenance. Geology, 35, 643–646.

Grimes, C.B., Wooden, J.L., Cheadle, M.J., John, B.E. 2015. “Fingerprinting” tectono-magmatic provenance using trace elements in igneous zircon. Contributions to Mineralogy and Petrology 170, 46. DOI: https://doi.org/10.1007/s00410-015-1199-3.

Guitreau, M., Blichert-Toft, J., Martin, H., Mojzsis, S.F., Albarède, F., 2012. Hafnium isotope evidence from Archean granitic rocks for deep-mantle origin of continental crust. Earth and Planetary Science Letters 337–338, 211-223. https://doi.org/10.1016/j.epsl.2012.05.029

Hawkesworth, C.J., Kemp, A.I.S. 2006. Using hafnium and oxygen isotopes in zircons to unravel the record of crustal evolution. Chemical Geology 226, 144-162. DOI: https://doi.org/10.1016/j.chemgeo.2005.09.018

Heilimo, E., Halla, J., Hölttä, P. 2010. Discrimination and origin of the sanukitoid series: Geochemical constraints from the Neoarchean western Karelian Province (Finland). Lithos, 115, 27–39.

https://doi.org/10.1016/j.lithos.2009.11.001

Hofmann, A., Kröner, A., Iaccheri, L.M., Wong, J., Geng, H., Xie, H. 2022. 3.63 Ga grey gneisses reveal the Eoarchaean history of the Zimbabwe craton. South African Journal of Geology, 125(1), 1-12. https://doi.org/10.25131/sajg.125.0005

Horstwood, M.S.A., Nesbitt, R.W., Noble, S.R., Wilson, J.F. 1999. U–Pb zircon evidence for an extensive early Archean craton in Zimbabwe: a reassessment of the timing of craton formation, stabilization and growth. Geology 27, 707-710. https://doi.org/10.1130/0091-7613(1999)027<0707:UPZEFA>2.3.CO;

Hoskin, P.W.O., Black, L.P. 2000. Metamorphic zircon formation by solid-state recrystallization of protolith igneous zircon. Journal of Metamorphic Geology 18, 423-439.

Hoskin, P.W.O., Schaltegger, U. 2003. The composition of zircon and igneous and metamorphic petrogenesis. In: Hanchar, J.M., Hoskin, P.W.O. (eds). Zircon. Reviews in Mineralogy and Geochemistry 53, 27-62. Mineralogical Society of America, Washington, D.C.

Iizuka, T., Horie, K., Komiya, T., Maruyama, S., Hirata, T., Hidaka, H., Windley, B.F., 2006. 4.2 Ga zircon xenocryst in an Acasta gneiss from northwestern Canada: evidence for early continental crust. Geology 34, 245–248.

Jelsma, H.A., Nesbitt, R.W., Fanning, C.M. 2021. Exploring our current understanding of the geological evolution and mineral endowment of the Zimbabwe Craton. South African Journal of Geology, v.124, p. 279-310. https://doi.org/10.25131/sajg.124.0020

Kearey, P., Klepeis, K.A., Vine, F.J. 2009. Precambrian tectonics and the supercontinent cycle. In: Kearey, P., Klepeis, K.A., Vine, F.J. Global tectonics. 3th ed. Oxford: Wiley-Blackwell, c2009.

Kemp, A.I.S., Hickman, A.H., Kirkland, C.L., Vervoort, J.D. 2015. Hf isotopes in detrital and inherited zircons of the Pilbara Craton provide no evidence for Hadean continents. Precambrian Research 261, 112-126. https://doi.org/10.1016/j.precamres.2015.02.011

Kröner, A., Elis Hoffmann, J., Xie, H., Wu, F., Münker, C., Hegner, E., Wong, J., Wan, Y., Liu, D. 2013a. Generation of early Archaean felsic greenstone volcanic rocks through crustal melting in the Kaapvaal, craton, southern Africa. Earth and Planetary Sciences Letters 381, 188–197. https://doi.org/10.1016/j.epsl.2013.08.029.

Kröner, A., Kovach, V., Belousova, E., Hegner, E., Armstrong, R.,

Dolgopolova, A., Seltmann, R., Alexeiev, D.V., Hoffmann, J.E., Wong, J., Sun, M., Cai, K., Wang, T., Tong, Y., Wilde, S.A., Degtyarev, K.E., Rytsk, E. 2014. Reassessment of continental growth during the accretionary history of the Central Asian Orogenic Belt. Gondwana Research https://doi.org/10.1016/j.gr.2012.12.023.

Lacerda, C.M.M. 2000. Evolução estrutural e petrogenética do domo granodiorítico de Ambrósio, Bahia: implicações para o mecanismo de colocação. Ph.D. Thesis. Universidade Estadual de Campinas, Campinas, pp. 209.

Lana, C., Alkmim, F.F., Armstrong, R., Scholz, R., Romano, R., Nalini, H.A. 2013. The ancestry and magmatic evolution of Archaean TTG rocks of the Quadrilátero Ferrífero province, southeast Brazil. Precambrian Research 230, 1–30.

Laurent, O., Zeh, A. 2015. A linear Hf isotope-age array despite different granitoid sources and complex Archean geodynamics: example from the Pietersburg block (South Africa). Earth and Planetary Science Letters 430, 326–338. https://doi.org/10.1016/j.epsl.2015.08.028.

Laurent, O., Björnsen, J., Wotzlaw, J.F., Bretscher, S., Silva, M.P., Moyen, J.F., Ulmer, P., Bachmann, O., 2020. Earth's earliest granitoids are crystal-rich magma reservoirs tapped by silicic eruptions. Nature Geoscience 13, 163–169.

Leal, L.R.B., Teixeira, W., Cunha, J.C., Macambira, M.J.B., Cordani. U.G. 1996. Evolução crustal dos terrenos TTGs Arqueanos do Bloco do Gavião, Cráton do São Francisco: Geocronologia U-Pb (SHRIMP) e Pb-Pb em zircões. In: Anais do XXXIX Congresso Brasileiro de Geologia, Salvador: SBG 6, 539-541.

Leal, L.R.B., 1998. Geocronologia U/Pb (SHRIMP), 207Pb/206Pb, Rb/Sr, Sm/Nd e K/Ar dos Terrenos Granito-Greenstone do Bloco do Gavião: Implicações para a Evolução Arqueana e Paleoproterozoica do Cráton do São Francisco, Brasil. Ph.D. Thesis. Universidade de São Paulo, São Paulo, pp.178. http://www.teses.usp.br/teses/disponiveis/44/44134/tde-08012016-145912/pt-br.php.

Leal, L.R.B., Teixeira, W., Cunha, J.C., Macambira, M.J.B. 1998. Archaean tonalitic-trondhjemitic and granitic plutonism in the Gavião Block, São Francisco Craton, Bahia, Brazil: geochemical and geochronological characteristics. Revista Brasileira de Geociências 28(2), 209-220.

Lopes, L.B.L., Ganade, C.E., Campos, L.D., Rodrigues, J.B., Oliveira, L.B.T., Larizzatti, J.H., Shen, M., Gao, T., Xu, M., Zhou, Y., Yao, Z. 2021. Crustal reworking and Archean TTG generation in the south Gavião Block, São Francisco Craton, Brazil. Precambrian Research 363, 106333.

https://doi.org/10.1016/j.precamres.2021.106333

Machado, N., Noce, C.M., Ladeira, E.A., Belo de Oliveira, O.A. 1992. U–Pb geochronology of Archean magmatism and Proterozoic metamorphism in the Quadrilátero Ferrífero, southern São Francisco craton, Brazil. Geological Society of America Bulletin 104 (9), 1221–1227.

Maltese, A., Mezger, K., Upadhyay, D., Berndt, J., Scherer, E.E. 2021. On the petrogenesis of Paleoarchean continental crust: U-Pb-Hf isotope and major-trace element constraints from the Bastar Craton, India. Chemical Geology 579, 120337. DOI: https://doi.org/j.chemgeo.2021.120337.

Marinho, M.M., 1991. La sequence volcano - sedimentaire de Contendas - Mirante et la bordure occidentale du bloc Jequié (Craton du São Francisco, Brésil): un exemple de transition Archeen – Proterozoique. Ph.D. Thesis, Université Blaise Pascal, Clermont Ferrand II, France, pp. 388.

Martin, H. 1993. The mechanisms of petrogenesis of the Archean continental crust –comparison with modern processes. Lithos, 30, 373-388. https://doi.org/10.1016/0024-4937(93)90046 -f

Martin, H. 1994. The Archean grey gneisses and the genesis of continental crust. Developments on Precambrian Geology 11, 205–259. https://doi.org/10.1016/S0166-2635(08)70224-X.

Martin, H., Peucat, J.J., Sabaté, P., Cunha, J.C., 1997. Crustal evolution in the early Archaean of South America: example of the Sete Voltas Massif, Bahia State, Brazil. Precambrian Research 82, 35-62. https://doi.org/10.1016/S0301-9268(96)00054-X.

Martin, H., Smithies, R., Rapp, R., Moyen, J., Champion, D. 2005. An overview of adakite, tonalite Trondhjemite Granodiorite (TTG), and sanukitoid: Relationships and some implications for crustal evolution. Lithos, 79, 1–24. https://doi.org/10.1016/j.lithos.2004.04.048

Martin, H., Moyen, J.-F., Rapp, R., 2010. Sanukitoids and the Archaean–Proterozoic boundary. In: Clemens, J.D., Frost, C.D., Kisters, A., Moyen, J.-F., Rushmer, T., Stevens, G. (Eds.), Sixth Hutton Symposium on The Origin of Granites and Related Rocks: Proceedings of a Symposium held in Stellenbosch, South Africa, 2–6 July 2007. Geological Society of America, Boulder, pp. 15–33.

Martin, H., Moyen, J.-F., Guitreau, M., Blichert-Toft, J., Le Pennec, J.-L. 2014. Why Archaean TTG cannot be generated by MORB melting in subduction zones. Lithos 198-199, 1–13. https://doi.org/10.1016/j.lithos.2014.02.017.

Medeiros, E.L.M., Cruz, S.C.P., Barbosa, J.S.F., Paquette, J.L., Peucat, J.J.,

Jesus, S.S.G.P., Barbosa, R.G., Brito, R.S.C., Carneiro, M.C., 2017. The Santa Izabel Complex, Gavião Block, Brazil: Components, geocronology, regional correlations and tectonic implications. Journal of South American Earth Sciences 80, 66–94.

Mello, E.F., Xavier, R.P., McNaughton, N.J., Hagemann, S.G., Fletcher, I., Snee, L. 2006. Age constraints on felsic intrusions, metamorphism and gold mineralization in the Paleoproterozoic Rio Itapicuru greenstone belt, NE Bahia State, Brazil. Mineralium Deposita 40, 849–866.

Moreira, I.C., Oliveira, E.P., Sousa, D.F.M. 2022. Evolution of the 3.65-2.58 Ga Mairi Gneiss Complex, Brazil: Implications for growth of the continental crust of the São Francisco Craton. Geoscience Frontiers 101366. https://doi.org/10.1016/j.gsf.2022.101366.

Moyen, J.-F. 2011. The composite Archaean grey gneisses: Petrological significance, and evidence for a non-unique tectonic setting for Archaean crustal growth. Lithos, 123, 21–36. https://doi.org/10.1016/j.lithos.2010.09.015

Moyen, J.F., Martin, H., 2012. Forty years of TTG research. Lithos 148, 312-336.

Moyen, J.-F., Laurent, O. 2018. Archaean tectonic systems: A view from igneous rocks. Lithos 302-303, 99-125. DOI: https://doi.org/10.1016/j.lithos.2017.11.038.

Moyen, J.F., Zeh, A., Cuney, M., Dziggel, A., Carrouée, S. 2021. The multiple ways of recycling Archaean crust: A case study from the ca. 3.1 Ga granitoids from the Barberton Greenstone Belt, South Africa. Precambrian Research 353, 105998. DOI: https://doi.org/10.1016/j.precamres.2020.105998.

Mühlberg, M., Stevens, G., Moyen, J-F., Kisters, A.F.M., Lana, C., 2021. Thermal evolution of the Stolzburg Block, Barberton granitoid-greenstone terrain, South Africa: Implications for Paleoarchean tectonic processes. Precambrian Research 359, 106082. DOI: https://doi.org/10.1016/j.precamres.2020.106082.

Nebel, O., Capitanio, F.A., Moyen, J.F., Weinberg, R., Clos, R., Nebel-Jacobsen, Y.J., Cawood, P.A. 2018. When crust comes of age: of the chemical evolution of Archaean, felsic continental crust by crustal drip tectonics. Philosophical Transactions Royal Society Acta 376: 20180103. DOI: https://dx.doi.org/10.1098/rsta.2018.0103

Nutman, A.P., Cordani, U.G., 1993. SHRIMP U-Pb zircon geochronology of Archaean granitoids from the Contendas-Mirante area of the São Francisco Craton, Bahia, Brazil. Precambrian Research 63, 179–188.

Oliveira, E.P. 2011. The Late Archaean Uauá Mafic Dyke Swarm, São

Francisco Craton, Brazil, and Implications for Palaeoproterozoic extrusion tectonics and Orogen Reconstruction. In: Srivastava RK (Ed) “Dyke Swarms: Keys for Geodynamic Interpretation”. Springer-Verlag Berlin Heidelberg, p. 19–31. DOI:10.1007/978-3-642-12496-9-2.

Oliveira, E.P., Lafon, J-M., Souza, Z.S. 1999. Archaean-Proterozoic transition in the Uauá Block, NE São Francisco Craton, Brazil: U-Pb, Pb-Pb and Nd isotope constraints. In: Proceedings, VII Simpósio Nacional de Estudos Tectônicos (SNET).

Oliveira, E.P., Souza, Z.S., Correa-Gomes, L.C. 2000. U-Pb dating of deformed mafic dyke and host gneiss: implications for understanding reworking processes on the western margin of the Archaean Uauá Block, NE São Francisco Craton, Brazil. Revista Brasileira de Geociências 30(1), 149-152.

Oliveira, E.P., Mello, E.F., McNaughton, N. 2002a. Reconnaissance U-Pb geochronology of Precambrian quartzites from the Caldeirão belt and their basement, NE São Francisco Craton, Bahia, Brazil: implications for the early evolution of the Paleoproterozoic Itabuna-Salvador-Curaçá Orogen. Journal of South American Earth Sciences 15, 349-362.

Oliveira, E.P., McNaughton, N., Armstrong, R. 2010. Mesoarchean to Paleoproterozoic growth of the northern segment of the Itabuna-Salvador-Curaçá Orogen, São Francisco Craton, Brazil. In: Kusky, T., Mingguo, Z., Xiao, W. (Eds.) The evolving continents: understanding processes of continental growth. Geological Society of London Special Publications 338, 263-286.

Oliveira, E.P., Souza, Z.S., McNaughton, N.J., Lafon, J.-M., Costa, F.G., Figueiredo, A.M. 2011. The Rio Capim volcanic-plutonic-sedimentary Belt, São Francisco Craton, Brazil: Geological, geochemical and isotopic evidence for oceanic arc accretion during Paleoproterozoic continental collision. Gondwana Research 19, 735-750.

Oliveira, E.P., Silveira, E.M., Sõderlund, U., Ernst, R.E. 2013. U-Pb ages and geochemistry of mafic dyke swarms from the Uauá Block, São Francisco Craton, Brazil: LIPs remnants relevant for Late Archaean break-up of a supercraton. Lithos 174, 308-322.

Oliveira, E.P., Talavera, C., Windley, B.F., Zhao, L., Semprich, J.J., McNaughton, N.J., Amaral, W.S., Sombini, G., Navarro, M., Silva, D. 2019. Mesoarchean (2820 Ma) high-pressure mafic granulite at Uauá, São Francisco Craton, Brazil, and its potential significance for the assembly of Archaean supercratons. Precambrian Research 331, 1-20.

Oliveira, E.P., McNaughton, N.J., Zincone, S.A., Talavera, C., 2020.

Birthplace of the São Francisco Craton, Brazil: evidence from 3.60 to 3.64 Ga Gneisses of the Mairi Gneiss complex. Terra Nova 32, 281–289. https://doi.org/10.1111/ter.12460

Paixão, M.A.P., Oliveira, E. P. 1998. The Lagoa da Vaca complex: an Archaean layered anorthosite body on the western edge of the Uauá block, Bahia, Brazil. Revista Brasileira de Geociências 28, 201-208.

Palme, H., O'Neill, H.S.C. 2014. Cosmochemical estimates of mantle composition. In: Holland, H.D., Turekian, K.K. (eds.), Treatise on Geochemistry, Amsterdam, Netherlands, Elsevier, 1-39.

Paquette, J.L., Barbosa, J.S.F., Rohais, S., Cruz, S.C.P., Goncalves, P., Peucat, J.-J., Leal, Â.B.M., Santos-Pinto, M., Martin, H. 2015. The geological roots of South America: 4.1 Ga and 3.7 Ga zircon crystals discovered in N.E. Brazil and N.W. Argentina. Precambrian Research 271, 49–55.

Petersson, A., Kemp, A.I.S., Hickman, A.H., Whitehouse, M.J., Martin, L., Gray, C.M., 2019. A new 3.59 Ga magmatic suite and a chondritic source to the east Pilbara Craton. Chemical Geology 511, 51-70. https://doi.org/10.1016/j.chemgeo.2019.01.021

Petersson, A., Kemp, A.I.S., Gray, C.M., Whitehouse, M.J., 2020. Formation of early Archean Granite-Greenstone Terranes from a globally chondritic mantle: Insights from igneous rocks of the Pilbara Craton, Western Australia. Chemical Geology 551, 119757. https://doi.org/10.1016/j.chemgeo.2020.119757

Peucat, J.J., Mascarenhas, J.F., Barbosa, J.S., Souza, F.S., Marinho, M.M., Fanning, C.M., Leite, C.M.M. 2002. 3.3 Ga SHRIMP U–Pb zircon age of a felsic metavolcanic rock from the Mundo Novo greenstone belt in the São Francisco Craton, Bahia (NE Brazil). Journal of South American Earth Sciences 15, 363–373.

Pickering, C. M., Byrne, J. 2014. The benefits of publishing systematic quantitative literature reviews for PhD candidates and other early career researchers. High. Educ. Res. Dev. 33, 534–548. doi:10.1080/07294360.2013.841651

Pinese, J.P.P., Teixeira, W., Piccirillo, E.M., Quéméneur, J.J.G., Bellieni, G. 1995. The Precambrian Lavras mafic dykes, southern São Francisco Craton, Brazil: preliminary geochemical and geochronological results. In: Baer, G., Heimann, A. (eds.) Physics and Chemistry of Dykes, Rotterdam – Netherlands; 3rd Int Dyke Conf, pp. 205–219.

Rios, D.C. 2002a. Granitogênese no Núcleo Serrinha, Bahia, Brasil: geocronologia e litogeoquímica. Ph.D. Thesis, Universidade Federal da Bahia,

Salvador, pp. 143.

Rios, D.C., Davis, D.W., Conceição, H., Rosa, M.L.S., Davis, W.J., Dickin, A.P., Marinho, M.M., Stern, R. 2008. 3.65–2.10 Ga history of crust formation from zircon geochronology and isotope geochemistry of the Quijingue and Euclides plutons, Serrinha nucleus, Brazil. Precambrian Research 167, 53-70.

Rios, D.C., Davis, D.W., Conceição, H., Davis, W.J., Rosa, M.L.S., Dickin, A.P., 2009. Geologic evolution of the Serrinha nucleus granite-greenstone terrane (NE Bahia, Brazil) constrained by U-Pb single zircon geochronology. Precambrian Res. 170 (3–4), 175–201. https://doi.org/10.1016/j.precamres.2008.10.001.

Roberts, M.P., Finger, F. 1997. Do U-Pb zircon ages from granulites reflect peak metamorphic conditions? Geology 25, 319-322.

Rollinson, H. 2007. Early Earth systems. A geochemical approach. Blackwell, 285p.

Rollinson, H., Pease, V. 2021. Using geochemical data to understand geological processes: Cambridge, Cambridge University Press, 346p.

Romano, R., Lana, C., Alkmim, F.F., Stevens, G., Armstrong, R. 2013 Stabilization of the Southern São Francisco Craton, SE Brazil, through a long-lived and episodic period of potassic magmatism. Precambrian Research 224, 1–20.

Rosa, M.L.S. 1999. Geologia, Geocronologia, Mineralogia, Litogeoquímica e Petrologia do Batólito Monzo-Sienítico Guanambi-Urandi (SW-Bahia) [Ph.D. thesis]: Salvador, Universidade Federal da Bahia, 220p.

Rosa, M.L.S., Conceição, H., Oberli, F., Meier, M., Martin, H., Macambira, M.B., Santos, E.B., Paim, M.M., Leahy, G.A.S., Bastos Leal, L.R., 2000. Geochronology (UPb/Pb-Pb) and isotopic signature (Rb-Sr/Sm-Nd) of the Paleoproterozoic Guanambi batholith, southwest Bahia state (NE Brazil). Revista Brasileira de Geociências 30, 62–65.

Rubatto, D. 2002. Zircon trace element geochemistry: partitioning with garnet and the link between U-Pb ages and metamorphism. Chemical Geology 184, 123-138.

Sabaté, P.; Marinho, M.M.; Vidal, P.; Caen Vachette, M. 1990. The 2 Ga peraluminous magmatism of the Jacobina–Contendas Mirante belts (Bahia, Brazil): geologic and isotopic constraints on the sources. Chemical Geology 83, 325–338.

Santos, C., Zincone, S.A., Queiroga, G.N., Bersan, S.M., Lana, C.C., Oliveira, E.P. 2022. Evidence for change in crust formation process during the Palaeoarchaean in the São Francisco Craton (Gavião Block): Coupled zircon Lu-

Hf and U-Pb isotopic analyses and tectonic implications. Precambrian Research 368, 106472. DOI: https://doi.org/10.1016/j.precamres.2021.106472.

Santos Pinto, M.A., 1996. Le recyclage de la croûte continentale archéenne: exemple du bloc du Gavião-Bahia, Brésil. Mémoires Geosciences Rennes 75, Ph.D Thesis, pp. 229.

Santos-Pinto, M.A., Peucat, J.J., Martin, H., Barbosa, J.S.F., Fanning, C.M., Cocherie, A., Paquette, J.L. 2012. Crustal evolution between 2.0 and 3.5 Ga in the southern Gavião block (Umburanas-Brumado-Aracatu region), São Francisco Craton, Brazil: A 3.5–3.8 Ga proto-crust in the Gavião block? Journal of South American Earth Sciences 40, 129-142.

Sato, K. 1998. Evolução crustal da Plataforma Sul-Americana com base na geoquímica isotópica Sm-Nd. Ph.D Thesis. Universidade de São Paulo, São Paulo, pp. 325.

Smithies, R.H., Van Kranendonk, M.J., Champion, D.C., 2007. The Mesoarchean emergence of modern-style subduction: Gondwana Research 11, 50-68.

Taylor, S.R., McLennan, S.M. 1985. The Continental Crust: its Composition and Evolution. Blackwell, Oxford, p. 312.

Teixeira, W., Sabaté, P., Barbosa, J.S.F., Noce, C.M., Carneiro, M.A. 2000. Archean and Paleoproterozoic tectonic evolution of the São Francisco Craton. In: Cordani, U.G, Milani, E.J., Thomaz-Filho, A., Campos, D.A. (eds) Tectonic Evolution of South America. 31st IGC, 101–137.

Teixeira, W., Oliveira, E.P., Marques, L.S. 2017. Nature and Evolution of the Archean Crust of the São Francisco Craton. In: Heilbron, M.; Cordani, U.G.; Alkmim, F.F. (Eds.). São Francsico Craton, Eastern Brazil. Tectonic Genealogy of a Miniature Continent. Mumbai, India. Springer (Regional Geology Reviews).

Teles, G.S. 2013. Proveniência e idades de deposição dos sedimentos auríferos da Bacia de Jacobina: implicações sobre a evolução da bacia durante o paleoarqueano e a gênese da mineralização. 120 f. Dissertação (Mestrado em Geologia) - Instituto de Geociências, Universidade de Brasília, Brasília.

Teles, G., Chemale, F., de Oliveira, C.G., 2015. Paleoarchean record of the detrital pyrite bearing, Jacobina Au–U deposits, Bahia, Brazil. Precambrian Research 256: 289–313.

Vervoort, J.D., Blichert-Toft, J. 1999. Evolution of the depleted mantle: Hf isotope evidence from juvenile rocks through time. Geochimica et Cosmochimica Acta, 63(3-4), 533-556.

Vervoort J.D., Kemp, A.I.S., Fisher, C.M., Bauer, A.M. 2017. Growth of the

Earth's earliest crust: The perspective from the depleted mantle, in Proceedings, Goldschmidt 2017, Paris, France, European Association of Geochemistry/Geochemical Society, p.1.

Wang, X., Griffin, W.L., Chen, J. 2011. U and Th Contents and Th/U Ratios of Zircon in Felsic and Mafic Magmatic Rocks: Improved Zircon-Melt Distribution Coefficients. Acta Geologica Sinica, English Edition, 85, 164-174. DOI: https://doi.org/10.1111/j.1755-6724.2011.00387.x

Wilde, S.A., Valley, J.W., Peck, W.H., Graham, C.M., 2001. Evidence from detrital zircons for the existence of continental crust and oceans on the Earth 4.4 Ga ago. Nature 409, 175–178.

Wedepohl, K.H. 1995. The compositions of the continental crust. Geochimica et Cosmochimica Acta 59, 1217–1232.

Werlang, T. 2020. Um fragmento Paleoarqueano no Cráton do São Francisco, Brasil. 80 f. Dissertação (Mestrado em Geologia) – Instituto de Geociências, Universidade de Brasília, Brasília.

Whitney, D.L., Evans, B.W. 2010. Abbreviations for names of rock forming minerals. American Mineralogist 95, 185-187.

White, R.W., Powell, R. 2010. Retrograde melt–residue interaction and the formation of near-anhydrous leucosomes in migmatites, Journal of Metamorphic Geology 28, 579–597.

Zeh, A., Gerdes, A., Barton, J.M., 2009. Archean accretion and crustal evolution of the Kalahari Craton the zircon age and Hf isotope record of granitic rocks from Barberton/Swaziland to the Francistown arc. Journal of Petrology 50, 933-966. https://doi.org/10.1093/petrology/egp027

Zincone, S.A, Oliveira, E.P., Laurent, O., Zhang, H., Zhai, M., 2016. 3.30Ga high-silica intraplate volcanic–plutonic system of the Gavião Block, São Francisco Craton, Brazil: Evidence of an intracontinental rift following the creation of insulating continental crust. Lithos 266–267, 414-434. https://doi.org/10.1016/j.lithos.2016.10.01

Zindler, A., Hart, S. 1986. Chemical Geodynamics. Annual Reviews on Earth and Planetary Sciences 14, 493-571.

7. APÊNDICES

7.1. APÊNDICE 1

Sample	Portion	Geological Unit	Rock	Rb ppm	Sr ppm	$^{87}Rb/^{86}Sr$	error 1	$^{87}Sr/^{86}Sr$ measured	±2sigma	Age (Ma)	$^{87}Sr/^{86}Sr(i)$	error abs	Eps Sr	References
RS-310	West	Riacho de Santana Complex	Grt Gneiss	91.4	160	1.66164	0.01662	0.762520	0.000035	3300	0.682802498	0.000798742	822.6411	Barbosa et al. 2020
RS-307b	West	Riacho de Santana Complex	Hbl-Grt-Gneiss	50.8	358	0.41096	0.00411	0.717890	0.000035	3300	0.698174036	0.000203401	189.1961	Barbosa et al. 2020
BR-WP-12A	West	Riacho de Santana Complex	Migmatite/Orthogneiss			#DIV/0!	#DIV/0!		0.000035		#DIV/0!	#DIV/0!	-10000	Barbosa et al. 2013
BR-WP-12B	West	Riacho de Santana Complex	Migmatite/Orthogneiss			#DIV/0!	#DIV/0!		0.000035		#DIV/0!	#DIV/0!	-10000	Barbosa et al. 2013
JM-BA610	West	Guanambi/Santa Izabel	Granulite			#DIV/0!	#DIV/0!	0.789600	0.000035	3030	#DIV/0!	#DIV/0!	1206.994	Sato. 1986
BR-09	West	Santa Izabel Complex	Granulite			#DIV/0!	#DIV/0!		0.000035		#DIV/0!	#DIV/0!	-10000	Barbosa et al. 2013
BR-12A A22	West	Santa Izabel Complex	Orthogneiss			#DIV/0!	#DIV/0!		0.000035		#DIV/0!	#DIV/0!	-10000	Barbosa et al. 2013
BR-12B A22	West	Santa Izabel Complex	Orthogneiss			#DIV/0!	#DIV/0!		0.000035		#DIV/0!	#DIV/0!	-10000	Barbosa et al. 2013
BR-12B A22-1	West	Santa Izabel Complex	Orthogneiss			#DIV/0!	#DIV/0!		0.000035		#DIV/0!	#DIV/0!	-10000	Barbosa et al. 2013
SSR 680C	North	Mundo Novo Greenstone Belt	Metadacite	52	61	2.49758	0.02498	0.837013	0.000035	3300	0.717190702	0.001199266	1879.939	Peucat et al. 2002
SSR 526A	North	Mairi Complex	Gneiss	92	350	0.76262	0.00763	0.736043	0.000035	3100	0.701722525	0.000346828	446.8463	Peucat et al. 2002
SSR 600	North	Mundo Novo Greenstone Belt	Metadacite	44	45	2.86355	0.02864	0.832663	0.000035	3300	0.695283556	0.001374704	1818.199	Peucat et al. 2002
SSR 533C	North	Mundo Novo Greenstone Belt	Metadacite	123	18	21.7221	0.21722	1.716713	0.000035	3300	0.674587631	0.010421374	14365.75	Peucat et al. 2002
RR-025	North	Miguel Calmon Granite	Metagranite	74.2	333	0.64604	0.00646	0.729151	0.000035	3355	0.697628242	0.000319168	349.0263	Spreafico et al., 2019
RR-008	North	Fazenda Coqueiro Metagranite	Metagranite	73.6	22	10.1033	0.10103	1.155501	0.000035	3227	0.681762982	0.004737644	6400.321	Spreafico et al., 2019
JM-BA304	North	Remanso Complex	Gneiss			#DIV/0!	#DIV/0!	1.006100	0.000035	3180	#DIV/0!	#DIV/0!	4279.834	Sato, 1986
JB 378C	North	Gavião Block	Granitoid			#DIV/0!	#DIV/0!		0.000035		#DIV/0!	#DIV/0!	-10000	Sato, 1998
JB 378C-1	North	Gavião Block	Granitoid			#DIV/0!	#DIV/0!		0.000035		#DIV/0!	#DIV/0!	-10000	Sato, 1998
JB 378E	North	Gavião Block	Granitoid			#DIV/0!	#DIV/0!		0.000035		#DIV/0!	#DIV/0!	-10000	Sato, 1998
BA-82-38-I	North	Gavião Block	Granitoid			#DIV/0!	#DIV/0!		0.000035		#DIV/0!	#DIV/0!	-10000	Sato, 1998
G-6	North	Gavião Block	Granitoid			#DIV/0!	#DIV/0!		0.000035		#DIV/0!	#DIV/0!	-10000	Sato, 1998
G-9	North	Gavião Block	Granitoid			#DIV/0!	#DIV/0!		0.000035		#DIV/0!	#DIV/0!	-10000	Sato, 1998
BR-JC-11H	South	Malhada de Pedras Bt-Granodiorite	Bt-Granodiorite	90.5	272.6	0.96402	0.00964	0.744920	0.000035	2840	0.705248239	0.000399856	572.8398	Leal et al. 1998
BR-JC-16D	South	Laoca da Macambira Granitoid	Granite	103	368	0.81261	0.00813	0.743214	0.000035	3146	0.706088993	0.000374602	548.6261	Bastos Leal et al. 2003
BR-JC-02	South	Gavião Block	TTG			#DIV/0!	#DIV/0!		0.000035		#DIV/0!	#DIV/0!	-10000	Leal. 1998
BR-JC-300	South	Gavião Block	TTG			#DIV/0!	#DIV/0!		0.000035		#DIV/0!	#DIV/0!	-10000	Leal. 1998
BR-JC-178	South	Gavião Block	TTG			#DIV/0!	#DIV/0!		0.000035		#DIV/0!	#DIV/0!	-10000	Leal et al. 1998
BR-JC-479J	South	Ibitiara-Brumado Complex	Metabasalt			#DIV/0!	#DIV/0!		0.000035		#DIV/0!	#DIV/0!	-10000	Leal. 1998
BR-702L	South	Umburanas Greenstone Belt	Metakomatiite			#DIV/0!	#DIV/0!		0.000035		#DIV/0!	#DIV/0!	-10000	Leal. 1998
BR-JC-711D	South	Umburanas Greenstone Belt	Metakomatiite			#DIV/0!	#DIV/0!		0.000035		#DIV/0!	#DIV/0!	-10000	Leal. 1998
BR-JC-707B	South	Umburanas Greenstone Belt	Metakomatiite			#DIV/0!	#DIV/0!		0.000035		#DIV/0!	#DIV/0!	-10000	Leal. 1998
MAR-94.1	South	Mariana Massif	Orthogneiss	81.1	67.1	3.65527	0.03655	0.878277	0.000035	3255	0.710091913	0.001992594	2465.61	Santos-Pinto. 1996
MAR-12.3	South	Mariana Massif	Orthogneiss	64	62	3.03208	0.03032	0.863418	0.000035	3259	0.719802323	0.001437027	2254.712	Santos-Pinto. 1996
SV-1	South	Sete Voltas Massif	Young Grey Gneiss	66	607	0.31485	0.00315	0.716082	0.000035	3140	0.701725968	0.000102018	163.5247	Martin et al. 1997
SV-2	South	Sete Voltas Massif	Young Grey Gneiss	83	447	0.5382	0.00538	0.726291	0.000035	3140	0.701750528	0.000250447	308.4336	Martin et al. 1997
SV-4	South	Sete Voltas Massif	Old Grey Gneiss	72	601	0.34693	0.00347	0.716987	0.000035	3420	0.699722971	0.000179735	176.3796	Martin et al. 1997
SV-6	South	Sete Voltas Massif	Young Grey Gneiss	144	465	0.89934	0.00899	0.742628	0.000035	3140	0.701634579	0.000412972	540.3898	Martin et al. 1997
SV-7	South	Sete Voltas Massif	Old Grey Gneiss	87	544	0.46338	0.00463	0.722502	0.000035	3420	0.699443104	0.000235948	254.6554	Martin et al. 1997
SV-9	South	Sete Voltas Massif	Old Grey Gneiss	79	432	0.53004	0.0053	0.725951	0.000035	3420	0.699575069	0.000268457	303.6079	Martin et al. 1997
SV-10	South	Sete Voltas Massif	Young Grey Gneiss	92	385	0.69311	0.00693	0.731300	0.000035	3140	0.701746244	0.000331968	408.6238	Martin et al. 1997
SV-11	South	Sete Voltas Massif	Old Grey Gneiss	24	756	0.09181	0.00092	0.703809	0.000035	3420	0.699240077	0.77311E-05	-10.6591	Martin et al. 1997
SV-12	South	Sete Voltas Massif	Porphyritic Granodiorite	94	566	0.48147	0.00481	0.728285	0.000035	3170	0.706116764	0.000227251	336.735	Martin et al. 1997
SV-14	South	Sete Voltas Massif	Porphyritic Granodiorite	58	555	0.30259	0.00303	0.715363	0.000035	3170	0.701431224	0.000148018	153.3297	Martin et al. 1997
SV-16	South	Sete Voltas Massif	Porphyritic Granodiorite	85	483	0.51002	0.0051	0.724823	0.000035	3170	0.701340481	0.000240089	287.5979	Martin et al. 1997
SV-18	South	Sete Voltas Massif	Porphyritic Granodiorite	81	469	0.50051	0.00501	0.724493	0.000035	3170	0.701448299	0.000235809	282.9142	Martin et al. 1997
SV-20	South	Sete Voltas Massif	Porphyritic Granodiorite	75	417	0.52127	0.00521	0.724450	0.000035	3170	0.701449257	0.00024516	296.4971	Martin et al. 1997
SV-24	South	Sete Voltas Massif	Young Grey Gneiss	80	465	0.49858	0.00499	0.724485	0.000035	3140	0.701751161	0.000232772	282.8006	Martin et al. 1997
SV-25	South	Sete Voltas Massif	Young Grey Gneiss	138	522	0.76704	0.00767	0.736489	0.000035	3140	0.701514365	0.000353302	453.1765	Martin et al. 1997
SV-27	South	Sete Voltas Massif	Young Grey Gneiss	63	341	0.53549	0.00535	0.726045	0.000035	3140	0.701628238	0.000249234	304.9421	Martin et al. 1997
SV-28	South	Sete Voltas Massif	Old Grey Gneiss	45	658	0.1979	0.00198	0.709542	0.000035	3420	0.699693851	0.000110447	70.7108	Martin et al. 1997
ARA-06.2A	South	Aracatu Massif	Aracatu Massif			#DIV/0!	#DIV/0!		0.000035		#DIV/0!	#DIV/0!	-10000	Santos-Pinto. 1996
ARA-78.1	South	Aracatu Massif	Gneiss	73	532	0.39753	0.00398	0.721150	0.000035	3240	0.702433203	0.000193731	235.4661	Santos-Pinto. 1996
ARA-78.1A	South	Aracatu Massif	Gneiss			#DIV/0!	#DIV/0!		0.000035		#DIV/0!	#DIV/0!	-10000	Santos-Pinto. 1996
VZP-65	South	Serra do Eixo Massif	K-rich calc--alkaline gneiss	155	608	0.73958	0.0074	0.735335	0.000035	3160	0.701392533	0.000343088	436.7974	Santos-Pinto et al. 2012
SEX-96	South	Serra do Eixo Massif	Gneiss	163	535	0.88433	0.00884	0.740524	0.000035	3160	0.699938686	0.000408921	510.4462	Santos-Pinto. 1996
ARN-58.1	South	Umburanas Massif	Granite	140	223	1.83001	0.0183	0.784300	0.000035	2830	0.709261729	0.000752047	1131.77	Santos-Pinto et al. 2012
UMB-164	South	Umburanas Massif	Granite	141	286	1.43484	0.01435	0.768200	0.000035	3130	0.702988719	0.000564027	903.2588	Santos-Pinto et al. 2012
UMB-165	South	Umburanas Massif	Granite	122	218	1.63391	0.01634	0.800800	0.000035	3000	0.729691608	0.00071284	1365.959	Santos-Pinto et al. 2012
AC-1B	South	Boa Vista Massif	Tonalite	137.3	152.2	2.6415	0.02641	0.831000	0.000035	3380	0.701126944	0.001299693	1794.595	Sato. 1998
31 BV-MV	South	Boa Vista/Mata Verde Massifs	Orthogneiss	58	373	0.4506	0.00451	0.723000	0.000035	3350	0.701946804	0.000225154	274.4976	Sato. 1998
32 BV-MV	South	Boa Vista/Mata Verde Massifs	Orthogneiss	62	330	0.54478	0.00545	0.730210	0.000035	3350	0.703668594	0.000270083	364.057	Sato. 1998
33 BV-MV	South	Boa Vista/Mata Verde Massifs	Orthogneiss	68	372	0.52988	0.0053	0.727210	0.000035	3350	0.701394238	0.000262955	321.4772	Sato. 1998
34 BV-MV	South	Boa Vista/Mata Verde Massifs	Orthogneiss			#DIV/0!	#DIV/0!		0.000035		#DIV/0!	#DIV/0!	-10000	Sato. 1998
35 BV-MV	South	Boa Vista/Mata Verde Massifs	Orthogneiss	40	415	0.27908	0.00279	0.715320	0.000035	3350	0.701723523	0.000144867	152.7194	Sato. 1998
36 BV-MV	South	Boa Vista/Mata Verde Massifs	Orthogneiss	54	360	0.43455	0.00435	0.726840	0.000035	3350	0.699689065	0.000217534	231.0662	Sato. 1998
37 BV-MV	South	Boa Vista/Mata Verde Massifs	Orthogneiss	76	206	1.07322	0.01073	0.763280	0.000035	3350	0.710993182	0.000525253	833.428	Sato. 1998
38 BV-MV	South	Boa Vista/Mata Verde Massifs	Orthogneiss	83	171	1.41483	0.01415	0.784110	0.000035	3350	0.715180183	0.000691109	1129.073	Sato. 1998
AC-4D	South	Lagoa do Morro Granitoid	Qz-Monzonite	134.4	281.9	1.38746	0.01387	0.767400	0.000035	3243	0.702012652	0.000605782	891.9042	Nutman and Cordani, 1993
AC-4F	South	Lagoa do Morro Granitoid	Granitoid	111.3	379.6	0.85128	0.00851	0.743400	0.000035	3243	0.703281603	0.000404288	551.266	Nutman and Cordani, 1993
AC-4H	South	Lagoa do Morro Granitoid	Granite	155.1	146.1	3.11334	0.03113	0.847000	0.000035	3243	0.700276253	0.001468089	2021.687	Nutman and Cordani, 1993
AC-4L	South	Lagoa do Morro Granitoid	Qz-Monzodiorite	138.5	199.4	2.02293	0.02027	0.795800	0.000035	3243	0.70027609	0.000956547	1294.993	Nutman and Cordani, 1993
MM-209B	South	Lagoa do Morro Granitoid	Granite	123.6	372.4	0.96367	0.00964	0.743878	0.000035	3200	0.69907851	0.000450776	558.0504	Marinho, 1991
MM-209C	South	Lagoa do Morro Granitoid	Granite	122.3	391.2	0.90739	0.00907	0.742807	0.000035	3200	0.700624181	0.000424781	542.8494	Marinho, 1991
42 B	South	Contendas-Mirante metavolcano-sedimentary Sequence	Subvolcanic	52	69	2.20323	0.02203	0.814610	0.000035	3300	0.708909401	0.001058188	1561.968	Marinho. 1991
42 D	South	Contendas-Mirante metavolcano-sedimentary Sequence	Subvolcanic	53	67	2.31333	0.02313	0.817710	0.000035	3300	0.706727479	0.001110951	1605.967	Marinho. 1991
42 E	South	Contendas-Mirante metavolcano-sedimentary Sequence	Subvolcanic	46	65	2.06746	0.02067	0.807180	0.000035	3300	0.707992909	0.00099313	1456.512	Marinho. 1991
42 F	South	Contendas-Mirante metavolcano-sedimentary Sequence	Subvolcanic	35	60	1.7027	0.01703	0.798320	0.000035	3300	0.716632705	0.000818402	1330.76	Marinho. 1991
42 G	South	Contendas-Mirante metavolcano-sedimentary Sequence	Subvolcanic	51	59	2.52941	0.02529	0.824010	0.000035	3300	0.702660941	0.00121452	1695.384	Marinho. 1991
42 I	South	Contendas-Mirante metavolcano-sedimentary Sequence	Subvolcanic	68	75	2.65448	0.02654	0.829500	0.000035	3300	0.70215973	0.001274474	1773.305	Marinho. 1991
42 J	South	Contendas-Mirante metavolcano-sedimentary Sequence	Subvolcanic	68	76	2.61943	0.02619	0.829020	0.000035	3300	0.70335221	0.001257672	1766.493	Marinho. 1991
MM-213C	South	Contendas-Mirante metavolcano-sedimentary Sequence	BIF			#DIV/0!	#DIV/0!		0.000035		#DIV/0!	#DIV/0!	-10000	Marinho. 1991
MM-213E	South	Contendas-Mirante metavolcano-sedimentary Sequence	BIF			#DIV/0!	#DIV/0!		0.000035		#DIV/0!	#DIV/0!	-10000	Marinho. 1991
MM-230B	South	Contendas-Mirante metavolcano-sedimentary Sequence	BIF			#DIV/0!	#DIV/0!		0.000035		#DIV/0!	#DIV/0!	-10000	Marinho. 1991
MM-230D	South	Contendas-Mirante metavolcano-sedimentary Sequence	BIF			#DIV/0!	#DIV/0!		0.000035		#DIV/0!	#DIV/0!	-10000	Marinho. 1991
MM-230E	South	Contendas-Mirante metavolcano-sedimentary Sequence	BIF			#DIV/0!	#DIV/0!		0.000035		#DIV/0!	#DIV/0!	-10000	Marinho. 1991
MM-8	South	Contendas-Mirante metavolcano-sedimentary Sequence	Tholeiitic Volcanic			#DIV/0!	#DIV/0!		0.000035		#DIV/0!	#DIV/0!	-10000	Marinho. 1991
MM-9	South	Contendas-Mirante metavolcano-sedimentary Sequence	Tholeiitic Volcanic			#DIV/0!	#DIV/0!		0.000035		#DIV/0!	#DIV/0!	-10000	Marinho. 1991
MM-15	South	Contendas-Mirante metavolcano-sedimentary Sequence	Tholeiitic Volcanic			#DIV/0!	#DIV/0!		0.000035		#DIV/0!	#DIV/0!	-10000	Marinho. 1991
MM-17	South	Contendas-Mirante metavolcano-sedimentary Sequence	Tholeiitic Volcanic			#DIV/0!	#DIV/0!		0.000035		#DIV/0!	#DIV/0!	-10000	Marinho. 1991
MM-20	South	Contendas-Mirante metavolcano-sedimentary Sequence	Tholeiitic Volcanic			#DIV/0!	#DIV/0!		0.000035		#DIV/0!	#DIV/0!	-10000	Marinho. 1991
MM-21	South	Contendas-Mirante metavolcano-sedimentary Sequence	Tholeiitic Volcanic			#DIV/0!	#DIV/0!		0.000035		#DIV/0!	#DIV/0!	-10000	Marinho. 1991
MM-22C	South	Contendas-Mirante metavolcano-sedimentary Sequence	Tholeiitic Volcanic			#DIV/0!	#DIV/0!		0.000035		#DIV/0!	#DIV/0!	-10000	Marinho. 1991
MM-23	South	Contendas-Mirante metavolcano-sedimentary Sequence	Tholeiitic Volcanic			#DIV/0!	#DIV/0!		0.000035		#DIV/0!	#DIV/0!	-10000	Marinho. 1991
MM-40	South	Contendas-Mirante metavolcano-sedimentary Sequence	Tholeiitic Volcanic			#DIV/0!	#DIV/0!		0.000035		#DIV/0!	#DIV/0!	-10000	Marinho. 1991
MM-68	South	Contendas-Mirante metavolcano-sedimentary Sequence	Tholeiitic Volcanic			#DIV/0!	#DIV/0!		0.000035		#DIV/0!	#DIV/0!	-10000	Marinho. 1991
MM-68bs	South	Contendas-Mirante metavolcano-sedimentary Sequence	Tholeiitic Volcanic			#DIV/0!	#DIV/0!		0.000035		#DIV/0!	#DIV/0!	-10000	Marinho. 1991
MM-100B	South	Contendas-Mirante metavolcano-sedimentary Sequence	Tholeiitic Volcanic			#DIV/0!	#DIV/0!		0.000035		#DIV/0!	#DIV/0!	-10000	Marinho. 1991
JM-BA-331D	South	Brumado Complex	Orthogneiss			#DIV/0!	#DIV/0!		0.000035		#DIV/0!	#DIV/0!	-10000	Sato, 1998
Retiroândia	Serrinha	Basement of the Rio Itapicuru Greenstone Belt	Migmatite/Orthogneiss			#DIV/0!	#DIV/0!		0.000035		#DIV/0!	#DIV/0!	-10000	Lacerda. 2000
Pedras Pretas	Serrinha	Basement of the Rio Itapicuru Greenstone Belt	Migmatite/Orthogneiss			#DIV/0!	#DIV/0!		0.000035		#DIV/0!	#DIV/0!	-10000	Lacerda. 2000
AM-4	Serrinha	Basement of the Rio Itapicuru Greenstone Belt	Migmatite/Orthogneiss			#DIV/0!	#DIV/0!		0.000035		#DIV/0!	#DIV/0!	-10000	Lacerda. 2000
1599	Serrinha	Araci Granite	Monzogranite	204	129	4.63313	0.04633	0.836710	0.000035	3070	0.630266237	0.002065043	1875.639	Rios, 2002a
1381	Serrinha	Pedra Alta Massif	Trondhiemite	62	480	0.37404	0.00374	0.716720	0.000035	3080	0.699997877	0.000174536	172.59	Rios. 2002a
1536	Serrinha	Santa Luz Complex	Diorite	71	509	0.4039	0.00404	0.715740	0.000035	3100	0.697563385	0.000188518	158.6806	Rios et al. 2009
CL-AB 9A	Serrinha	Ambrósio Dome	Migmatite/Orthogneiss			#DIV/0!	#DIV/0!		0.000035		#DIV/0!	#DIV/0!	-10000	Lacerda. 2000
UA96-2.3	Uauá	Uauá Block	Gneiss			#DIV/0!	#DIV/0!		0.000035		#DIV/0!	#DIV/0!	-10000	Oliveira et al. 2000
JM/BA 180A	Uauá	Rio Caim	Tonalite			#DIV/0!	#DIV/0!		0.000035		#DIV/0!	#DIV/0!	-10000	Sato. 1998
JM/BA 180B	Uauá	Rio Caim	Tonalite			#DIV/0!	#DIV/0!		0.000035		#DIV/0!	#DIV/0!	-10000	Sato. 1998
MS-1.2	Uauá	Caldeirão Belt	Metaolelite			#DIV/0!	#DIV/0!		0.000035		#DIV/0!	#DIV/0!	-10000	Oliveira et al. 2002a
EO-57.2	Uauá	Caldeirão Belt	Metaolelite			#DIV/0!	#DIV/0!		0.000035		#DIV/0!	#DIV/0!	-10000	Oliveira et al. 2002a
JM/BA 345	Uauá	Rio Caim	Granitoid			#DIV/0!	#DIV/0!		0.000035		#DIV/0!	#DIV/0!	-10000	Sato. 1998
JM/BA 377A	Uauá	Uauá Block	Granitoid			#DIV/0!	#DIV/0!		0.000035		#DIV/0!	#DIV/0!	-10000	Sato. 1998

Sample	Sm ppm	Nd ppm	$^{147}Sm/^{144}Nd$	error (%) 0.1	$^{143}Nd/^{144}Nd$ measured	±2sigma	Age (Ma)	$^{143}Nd/^{144}Nd(i)$	error t	eNd(0)	eNd(t)	error (t)	T(DM) Ga		T(DM) $^{147}Sm/^{144}Nd=$	References
RS-310	5.300	25.700	0.1247	0.000124700000000	0.510996	2E-06	3300	0.508275473	0.000003	-32.030	-1.401	0.066	3.59	-85.100	3.432	Barbosa et al. 2020
RS-307b	2.300	12.400	0.1122	0.000112200000000	0.510666	2E-06	3300	0.50821818	0.000003	-38.468	-2.528	0.062	3.65	-86.217	3.474	Barbosa et al. 2020
BR-WP-12A	5.387	41.035	0.0794	0.000079380000000	0.510430	2E-06	2840	0.508941185	0.000002	-43.071	-0.169	0.049	2.99	-72.101	2.942	Barbosa et al. 2013
BR-WP-12B	4.000	25.300	0.0950	0.000095060000000	0.510061	2E-06	3300	0.507988425	0.000003	-50.269	-7.047	0.057	3.91	-90.699	3.644	Barbosa et al. 2013
JM-BA610				0.000000000000000		2E-06		0	0.000002	-10000.000	-10000.000	0.039	#NUM!	-10000.000	#NUM!	Sato. 1986
BR-09	2.700	17.900	0.0896	0.000089600000000	0.510396	2E-06	2950	0.508650564	0.000003	-43.735	-3.059	0.052	3.29	-77.783	3.156	Barbosa et al. 2013
BR-12A A22	2.700	18.500	0.0909	0.000090900000000	0.510600	2E-06	2900	0.508859538	0.000003	-39.755	-0.241	0.052	3.06	-73.706	3.002	Barbosa et al. 2013
BR-12B A22	3.900	25.300	0.0950	0.000095000000000	0.510607	2E-06	2900	0.508788035	0.000003	-39.619	-1.646	0.053	3.17	-75.101	3.055	Barbosa et al. 2013
BR-12B A22-1	3.900	24.900	0.0941	0.000094100000000	0.510630	2E-06	2900	0.508828268	0.000003	-39.170	-0.850	0.053	3.11	-74.316	3.025	Barbosa et al. 2013
SSR 680C	9.700	48.000	0.1223	0.000122300000000	0.511005	2E-06	3300	0.508336833	0.000003	-31.855	-0.194	0.066	3.47	-83.903	3.387	Peucat et al. 2002
SSR 526A	2.160	15.000	0.0869	0.000086900000000	0.510357	2E-06	3100	0.508577209	0.000003	-44.495	-0.633	0.053	3.27	-79.214	3.210	Peucat et al. 2002
SSR 600	10.000	49.300	0.1231	0.000123100000000	0.511044	2E-06	3300	0.508358938	0.000003	-31.094	0.230	0.066	3.43	-83.482	3.371	Peucat et al. 2002
SSR 533C	13.900	69.300	0.1216	0.000121600000000	0.510992	2E-06	3300	0.508339104	0.000003	-32.108	-0.149	0.065	3.46	-83.858	3.385	Peucat et al. 2002
RR-025	2.400	18.400	0.0789	0.000078900000000	0.510000	2E-06	3355	0.508249667	0.000003	-51.459	-0.486	0.052	3.49	-85.603	3.451	Spreafico et al., 2019
RR-008	10.300	49.400	0.1261	0.000126100000000	0.510962	2E-06	3227	0.508272431	0.000003	-32.894	-3.347	0.066	3.71	-85.159	3.434	Spreafico et al., 2019
JM-BA304				0.000000000000000		2E-06		0	0.000002	-10000.000	-10000.000	0.039	#NUM!	-10000.000	#NUM!	Sato, 1986
JB 378C	1.774	8.419	0.1274	0.000127420000000	0.510805	2E-06	3000	0.508280334	0.000003	-35.756	-8.048	0.063	4.09	-85.005	3.428	Sato, 1998
JB 378C-1	1.728	8.196	0.1275	0.000127490000000	0.510810	2E-06	3000	0.508283947	0.000003	-35.659	-8.977	0.063	4.08	-84.934	3.426	Sato, 1998
JB 378E	4.385	24.978	0.1062	0.000106160000000	0.511038	2E-06	3190	0.508799962	0.000003	-31.211	6.072	0.059	2.87	-74.868	3.046	Sato, 1998
BA-82-38-I	0.773	5.592	0.0836	0.000083590000000	0.510209	2E-06	2900	0.508608503	0.000003	-47.382	-5.174	0.050	3.36	-78.603	3.187	Sato, 1998
G-6	11.920	72.888	0.0989	0.000098910000000	0.510601	2E-06	2920	0.508693985	0.000003	-39.736	-2.979	0.054	3.29	-76.936	3.124	Sato, 1998
G-9	2.756	17.823	0.0935	0.000093510000000	0.510363	2E-06	2920	0.508560098	0.000003	-44.378	-5.610	0.053	3.45	-79.547	3.222	Sato, 1998
BR-JC-11H	4.802	38.737	0.0754	0.000075400000000	0.510115	2E-06	2840	0.508701464	0.000002	-49.216	-4.892	0.048	3.26	-76.790	3.118	Leal et al. 1998
BR-JC-16D	3.419	24.782	0.0839	0.000083900000000	0.510239	2E-06	3146	0.50849489	0.000003	-46.797	-1.064	0.052	3.34	-80.819	3.270	Leal et al. 1998
BR-JC-02	3.865	24.255	0.0969	0.000096900000000	0.510441	2E-06	3300	0.508326974	0.000003	-42.857	-0.388	0.057	3.45	-84.095	3.394	Leal. 1998
BR-JC-300	2.851	18.287	0.0948	0.000094800000000	0.510540	2E-06	2840	0.508782769	0.000003	-40.926	-3.687	0.053	3.25	-75.594	3.073	Leal. 1998
BR-JC-178	3.698	19.939	0.1128	0.000112800000000	0.510702	2E-06	3202	0.50831494	0.000003	-37.765	-3.157	0.061	3.61	-84.330	3.403	Bastos Leal et al. 2003
BR-JC-479J	2.932	11.889	0.1501	0.000150100000000	0.511754	2E-06	3000	0.508779958	0.000004	-17.244	0.773	0.070	3.15	-75.259	3.061	Leal. 1998
BR-702L	0.931	3.359	0.1686	0.000168600000000	0.512486	2E-06	3000	0.509145404	0.000004	-2.965	7.956	0.077	1.87	-68.130	2.793	Leal. 1998
BR-JC-711D	0.207	0.764	0.1651	0.000165100000000	0.512604	2E-06	3000	0.509332752	0.000004	-0.663	11.639	0.075	1.37	-64.475	2.657	Leal. 1998
BR-JC-707B	0.353	1.097	0.1957	0.000195700000000	0.512875	2E-06	3000	0.508997452	0.000004	4.623	5.048	0.086	1.40	-71.016	2.902	Leal. 1998
MAR-94.1	14.633	65.370	0.1354	0.000134800000000	0.511337	2E-06	3255	0.50844096	0.000003	-25.379	0.691	0.069	3.36	-81.871	3.310	Santos-Pinto. 1996
MAR-12.3	12.570	56.390	0.1347	0.000134700000000	0.511243	2E-06	3259	0.508341209	0.000004	-27.212	-1.168	0.069	3.56	-83.817	3.384	Santos-Pinto. 1996
SV-1				0.000000000000000		2E-06		0	0.000002	-10000.000	-10000.000	0.039	#NUM!	-10000.000	#NUM!	Martin et al. 1997
SV-2	4.760	32.150	0.0889	0.000088900000000	0.510102	2E-06	3140	0.508257511	0.000003	-44.703	-5.887	0.053	3.66	-85.450	3.445	Martin et al.

7.2. APÊNDICE 2

Lithostratigraphic unit	Compartment	Sample/spot	U-Pb Age	176Hf/177Hf	±2SE	176Lu/177Hf	±2SE	176Hf/177Hf	epsilon Hf	TDM (Ga)
Contendas	Southern Gavião Block	TZD12-31-01	3300	0.280687836	1.12128E-05	0.001641643	7.93708E-06	0.280583501	-2.35	3.57
Contendas	Southern Gavião Block	TZD12-31-02	3310	0.280643841	9.96339E-06	0.000958728	9.1841E-07	0.280582729	-2.16	3.57
Contendas	Southern Gavião Block	TZD12-31-03	3299	0.280677829	1.03389E-05	0.001162275	9.04121E-07	0.28060398	-1.64	3.54
Contendas	Southern Gavião Block	TZD12-31-04	3300	0.280603158	1.12129E-05	0.000942361	2.49111E-06	0.280543276	-3.80	3.62
Contendas	Southern Gavião Block	TZD12-31-05	3312	0.280685434	9.75E-06	0.0009179	7.52417E-07	0.280626878	-0.52	3.51
Contendas	Southern Gavião Block	TZD12-31-06	3306	0.280554308	1.03978E-05	0.001176937	1.63723E-06	0.280479382	-5.94	3.71
Contendas	Southern Gavião Block	TZD12-31-07	3308	0.280673534	9.55514E-06	0.001172822	1.34128E-06	0.280598827	-1.64	3.55
Contendas	Southern Gavião Block	TZD12-31-08	3302	0.280654786	9.17063E-06	0.000874186	4.34419E-06	0.280599199	-1.76	3.55
Contendas	Southern Gavião Block	TZD12-31-09	3307	0.280592203	9.55305E-06	0.000865222	2.30718E-06	0.280537094	-3.84	3.63
Contendas	Southern Gavião Block	TZD12-31-10	3308	0.280677425	1.07486E-05	0.001344184	2.35741E-06	0.280591794	-1.88	3.56
Contendas	Southern Gavião Block	TZD12-31-11	3298	0.280676995	9.82846E-06	0.001050111	1.84253E-06	0.280610306	-1.46	3.53
Contendas	Southern Gavião Block	TZD12-31-12	3293	0.280688757	8.8199E-06	0.00119546	4.62731E-06	0.280612956	-1.48	3.53
Contendas	Southern Gavião Block	TZD12-31-13	3313	0.280666575	1.20126E-05	0.000980103	4.56573E-07	0.280604043	-1.33	3.54
Contendas	Southern Gavião Block	TZD12-31-14	3290	0.280733855	1.12957E-05	0.002396098	4.66625E-06	0.280582041	-2.64	3.58
Contendas	Southern Gavião Block	TZD12-31-15	3285	0.280707609	1.03749E-05	0.001398424	3.95051E-06	0.280619171	-1.46	3.52
Contendas	Southern Gavião Block	TZD12-31-15	3293	0.280707609	1.03749E-05	0.001398424	3.95051E-06	0.280618937	-1.27	3.52
Contendas	Southern Gavião Block	TZD12-31-16	3293	0.280661141	1.14396E-05	0.001973733	5.10694E-06	0.280535983	-4.22	3.64
Contendas	Southern Gavião Block	TZD12-31-17	3314	0.280640273	1.02338E-05	0.001321529	1.43901E-06	0.280555927	-3.01	3.61
Contendas	Southern Gavião Block	TZD12-31-18	3303	0.280619285	1.12234E-05	0.001689454	1.48238E-05	0.28051181	-4.84	3.67
Contendas	Southern Gavião Block	TZD12-31-19	3314	0.280581442	1.38528E-05	0.000939463	1.04854E-06	0.280521486	-4.25	3.65
Contendas	Southern Gavião Block	TZD12-31-20	3310	0.28064126	1.03865E-05	0.000731762	3.01977E-06	0.280594614	-1.73	3.55
Contendas	Southern Gavião Block	TZD12-31-21	3314	0.280726477	1.19767E-05	0.001061789	2.11844E-06	0.280658707	0.65	3.47
Contendas	Southern Gavião Block	TZD12-31-22	3305	0.280510545	1.10195E-05	0.001775262	4.84659E-06	0.280397546	-8.86	3.82
Contendas	Southern Gavião Block	TZD12-31-23	3305	0.280608999	1.27587E-05	0.002114881	2.18918E-06	0.28047438	-6.12	3.72
Contendas	Southern Gavião Block	TZD12-31-24	3309	0.280671954	1.31531E-05	0.001331467	4.29545E-06	0.280587101	-2.02	3.56
Contendas	Southern Gavião Block	TZD12-31-25	3306	0.280676304	1.3142E-05	0.001899423	7.00794E-06	0.280555365	-3.22	3.61
Contendas	Southern Gavião Block	TZD12-31-26	3298	0.280675726	1.13086E-05	0.001233558	6.58573E-07	0.280597374	-1.91	3.55
Contendas	Southern Gavião Block	TZD12-31-27	3305	0.280606324	1.23568E-05	0.001102454	2.09237E-06	0.280536155	-3.93	3.63
Contendas	Southern Gavião Block	TZD12-31-28	3303	0.280540513	1.0503E-05	0.001087495	1.09178E-06	0.280471345	-6.29	3.72
Contendas	Southern Gavião Block	TZD12-31-29	3303	0.280650316	1.19667E-05	0.001007433	5.33109E-06	0.280586233	-2.19	3.56
Contendas	Southern Gavião Block	TZD12-31-30	3291	0.280749632	1.36935E-05	0.002071371	1.04704E-05	0.280618373	-1.33	3.53
Contendas	Southern Gavião Block	TZD12-31-31	3287	0.280707905	8.99148E-06	0.001576266	1.46521E-06	0.280608131	-1.78	3.54
Contendas	Southern Gavião Block	TZD12-31-32	3303	0.280570525	1.06581E-05	0.001631246	7.88567E-06	0.280466751	-6.44	3.73
Contendas	Southern Gavião Block	TZD12-31-33	3329	0.280666305	1.14399E-05	0.000927174	3.66057E-07	0.280606845	-0.83	3.53
Contendas	Southern Gavião Block	TZD12-31-34	3309	0.280634227	1.05099E-05	0.001000578	1.25887E-06	0.280570464	-2.61	3.58
Contendas	Southern Gavião Block	TZD12-31-35	3305	0.280665843	1.19781E-05	0.001120198	1.48808E-06	0.280594546	-1.85	3.55
Contendas	Southern Gavião Block	TZD12-31-36	3291	0.280635467	1.12599E-05	0.001167609	7.32666E-07	0.280561484	-3.37	3.60
Contendas	Southern Gavião Block	TZD12-31-37	3319	0.280581518	1.35329E-05	0.001678288	7.38357E-06	0.280474248	-5.81	3.72
Contendas	Southern Gavião Block	TZD12-31-38	3304	0.28073891	1.2972E-05	0.001208019	6.09463E-06	0.280662045	0.53	3.46
Contendas	Southern Gavião Block	TZD12-31-39	3296	0.280613032	9.6661E-06	0.001016819	2.11255E-06	0.280548488	-3.69	3.61
Sete Voltas	Southern Gavião Block	SV11-4	3421	0.280573	0.000055	0.00036	0.000005	0.280549	-0.70	3.61
Sete Voltas	Southern Gavião Block	SV11-7	3430	0.280518	0.000004	0.00036	0.000005	0.280494	-2.45	3.68
Sete Voltas	Southern Gavião Block	SV2-1	3395	0.280582	0.000007	0.00045	0.0000027	0.280553	-1.20	3.60
Sete Voltas	Southern Gavião Block	SV2-2	3382	0.280586	0.000067	0.0011	0.0000023	0.280514	-2.88	3.66
Sete Voltas	Southern Gavião Block	SV2-3	3318	0.280573	0.000063	0.00097	0.0000035	0.280511	-4.52	3.66
Sete Voltas	Southern Gavião Block	SV2-4	3350	0.280486	0.000029	0.00034	0.000007	0.280464	-5.43	3.72
Sete Voltas	Southern Gavião Block	SV2-5	3424	0.280606	0.000076	0.00032	0.0000037	0.280585	0.64	3.56

Sete Voltas	Southern Gavião Block	SV9-4	3405	0.280541	0.000034	0.00046	0.0000023	0.280511	-2.45	3.66
Sete Voltas	Southern Gavião Block	SV9-5	3404	0.280588	0.000029	0.00082	0.000012	0.280534	-1.64	3.63
Sete Voltas	Southern Gavião Block	SV11-1	3372	0.280595	0.000048	0.00072	0.0000015	0.280548	-1.91	3.61
Sete Voltas	Southern Gavião Block	SV11-2	3437	0.280511	0.000064	0.00045	0.000005	0.280481	-2.75	3.70
Sete Voltas	Southern Gavião Block	SV11-3	3261	0.280607	0.000054	0.00072	0.0000017	0.280562	-4.06	3.59
Sete Voltas	Southern Gavião Block	SV11-5	3398	0.28063	0.000044	0.00064	0.0000031	0.280588	0.13	3.56
Sete Voltas	Southern Gavião Block	SV11-6	3381	0.280576	0.000059	0.00052	0.0000047	0.280542	-1.91	3.62
Sete Voltas	Southern Gavião Block	SV11-7	3430	0.280518	0.00004	0.00036	0.000005	0.280494	-2.45	3.68
Sete Voltas	Southern Gavião Block	SV2-7	3440	0.28076	0.0004	0.0023	0.0000081	0.280607	1.82	3.53
Sete Voltas	Southern Gavião Block	SV9-1	3264	0.280549	0.000047	0.0015	0.0000019	0.280455	-7.80	3.74
Sete Voltas	Southern Gavião Block	SV9-2	3410	0.28051	0.00001	0.001	0.0000041	0.280444	-4.71	3.75
Sete Voltas	Southern Gavião Block	SV9-3	3472	0.280499	0.000057	0.00063	0.0000011	0.280457	-2.78	3.73
Sete Voltas	Southern Gavião Block	SV9-7	3420	0.280483	0.000047	0.00045	0.0000024	0.280453	-4.14	3.73
Sete Voltas	Southern Gavião Block	SV9-8	3438	0.28052	0.000068	0.00049	0.0000014	0.280488	-2.50	3.69
Sete Voltas	Southern Gavião Block	SV9-9	3403	0.280511	0.000052	0.00036	0.0000085	0.280487	-3.34	3.69
Caldeirão Complex	Southern Gavião Block	CSD23B - 81	3480	0.280591	21.951767	0.000428	2.567607	0.280562	1.16	3.65
Caldeirão Complex	Southern Gavião Block	CSD23B - 82	3475	0.280361	97.860328	0.000742	4.453435	0.280311	-7.91	4.14
Caldeirão Complex	Southern Gavião Block	CSD23B - 83	3542	0.280388	105.394265	0.000428	2.567795	0.280359	-4.60	4.05
Caldeirão Complex	Southern Gavião Block	CSD23B - 84	3528	0.280566	21.649186	0.000536	3.213932	0.280529	1.13	3.71
Caldeirão Complex	Southern Gavião Block	CSD23B - 85	3512	0.280555	20.769407	0.000570	3.423435	0.280516	0.31	3.74
Caldeirão Complex	Southern Gavião Block	CSD23B - 86	3485	0.280513	31.880783	0.000448	2.687594	0.280483	-1.53	3.80
Caldeirão Complex	Southern Gavião Block	CSD23B - 87	3385	0.280434	72.353120	0.000438	2.639414	0.280405	-6.70	3.96
Caldeirão Complex	Southern Gavião Block	CSD23B - 88	3509	0.280509	23.774047	0.000316	1.896568	0.280487	-0.80	3.79
Caldeirão Complex	Southern Gavião Block	CSD23B - 89	3497	0.280494	37.468553	0.000289	1.747093	0.280474	-1.55	3.82
Caldeirão Complex	Southern Gavião Block	CSD23B - 90	3482	0.280410	124.400942	0.000670	4.111154	0.280365	-5.84	4.03
Caldeirão Complex	Southern Gavião Block	CSD23B - 91	3475	0.280506	36.289735	0.000352	2.166991	0.280482	-1.82	3.80
Caldeirão Complex	Southern Gavião Block	CSD23B - 92	3510	0.280395	83.587690	0.000827	4.964714	0.280339	-6.09	4.09
Caldeirão Complex	Southern Gavião Block	CSD23B - 93	3553	0.280481	210.972607	0.000499	2.996787	0.280447	-1.21	3.87
Caldeirão Complex	Southern Gavião Block	CSD25 - 188	3389	0.280505	14.104635	0.000463	3.285652	0.280475	-4.12	3.88
Caldeirão Complex	Southern Gavião Block	CSD25 - 189	3342	0.280514	26.077633	0.000505	3.662483	0.280481	-4.99	3.89
Caldeirão Complex	Southern Gavião Block	CSD25 - 190	3337	0.280594	119.785050	0.000562	9.287523	0.280558	-2.38	3.75
Caldeirão Complex	Southern Gavião Block	CSD25 - 191	3396	0.280498	33.318168	0.000295	2.363263	0.280478	-3.81	3.87
Caldeirão Complex	Southern Gavião Block	CSD25 - 192	3361	0.280474	52.948990	0.000780	5.514933	0.280423	-6.62	4.00
Caldeirão Complex	Southern Gavião Block	CSD25 - 193	3391	0.280376	66.642588	0.001032	8.389074	0.280308	-10.01	4.21
Caldeirão Complex	Southern Gavião Block	CSD25 - 194	3434	0.280528	45.089859	0.001027	7.579337	0.280460	-3.57	3.89
Caldeirão Complex	Southern Gavião Block	CSD25 - 195	3355	0.280530	31.536874	0.000583	4.088663	0.280493	-4.30	3.86
Caldeirão Complex	Southern Gavião Block	CSD25 - 196	3364	0.280522	20.172173	0.000378	3.357248	0.280498	-3.91	3.85
Caldeirão Complex	Southern Gavião Block	CSD25 - 197	3339	0.280457	55.067664	0.000346	2.276165	0.280434	-6.75	3.99
Caldeirão Complex	Southern Gavião Block	CSD25 - 198	3385	0.280647	49.972966	0.001105	12.178233	0.280575	-0.63	3.69
Caldeirão Complex	Southern Gavião Block	CSD25 - 199	3412	0.280584	23.298969	0.000809	6.893758	0.280531	-1.58	3.76
Caldeirão Complex	Southern Gavião Block	CSD25 - 200	3335	0.280519	32.356220	0.000312	2.173034	0.280499	-4.53	3.86
Caldeirão Complex	Southern Gavião Block	CSD25 - 201	3345	0.280523	19.763342	0.000442	2.805383	0.280495	-4.44	3.87
Caldeirão Complex	Southern Gavião Block	CSD25 - 202	3386	0.280523	27.928732	0.000743	4.818232	0.280474	-4.20	3.88
Caldeirão Complex	Southern Gavião Block	TZD217 - 60	3360	0.280701	32.216462	0.000168	1.367125	0.280690	2.87	3.47
Caldeirão Complex	Southern Gavião Block	TZD217 - 61	3390	0.280508	24.703600	0.000451	3.606891	0.280479	-3.94	3.87
Caldeirão Complex	Southern Gavião Block	TZD217 - 62	3360	0.280541	13.474918	0.000251	1.548789	0.280525	-3.02	3.80
Caldeirão Complex	Southern Gavião Block	TZD217 - 63	3372	0.280528	16.883494	0.000260	2.033860	0.280511	-3.25	3.82
Caldeirão Complex	Southern Gavião Block	TZD217 - 64	3391	0.280571	141.907697	0.000378	4.081496	0.280546	-1.52	3.74

Caldeirão Complex	Southern Gavião Block	TZD217 - 66	3295	0.280495	29.456901	0.000322	2.701816	0.280475	-6.34	3.93
Caldeirão Complex	Southern Gavião Block	TZD217 - 68	3339	0.280387	51.449894	0.000268	1.712178	0.280370	-9.05	4.11
Caldeirão Complex	Southern Gavião Block	TZD217 - 69	3362	0.280453	20.872204	0.000337	2.651295	0.280431	-6.31	3.98
Caldeirão Complex	Southern Gavião Block	TZD217 - 70	3382	0.280451	28.448477	0.000467	4.095354	0.280420	-6.23	3.99
Caldeirão Complex	Southern Gavião Block	TZD217 - 71	3374	0.280482	37.079699	0.000613	5.066394	0.280442	-5.63	3.95
Caldeirão Complex	Southern Gavião Block	TZD217 - 72	3401	0.280404	44.098270	0.000426	2.601782	0.280376	-7.36	4.07
Caldeirão Complex	Southern Gavião Block	TZD217 - 73	3385	0.280510	19.887015	0.000489	2.996483	0.280478	-4.09	3.88
Caldeirão Complex	Southern Gavião Block	TZD217 - 74	3321	0.280412	58.458841	0.000440	2.879155	0.280384	-8.97	4.09
Caldeirão Complex	Southern Gavião Block	TZD217 - 75	3347	0.280424	47.379180	0.000421	6.032258	0.280397	-7.87	4.06
Caldeirão Complex	Southern Gavião Block	TZD217 - 77	3387	0.280434	37.052991	0.000388	3.083565	0.280409	-6.52	4.01
Caldeirão Complex	Southern Gavião Block	TZD217 - 78	3357	0.280516	75.863395	0.000302	2.043935	0.280496	-4.11	3.86
Caldeirão Complex	Southern Gavião Block	TZD217 - 79	3353	0.280501	57.960933	0.000256	1.533361	0.280484	-4.64	3.88
Caldeirão Complex	Southern Gavião Block	TZD217 - 80	3369	0.280445	175.962846	0.000353	2.120205	0.280422	-6.48	4.00
Caldeirão Complex	Southern Gavião Block	CSD30A - 167	3373	0.280569	26.521148	0.000798	4.789231	0.280517	-2.98	3.81
Caldeirão Complex	Southern Gavião Block	CSD30A - 168	3383	0.280516	19.081229	0.000290	1.739046	0.280497	-3.46	3.84
Caldeirão Complex	Southern Gavião Block	CSD30A - 169	3385	0.280524	24.777000	0.000709	4.264660	0.280477	-4.13	3.88
Caldeirão Complex	Southern Gavião Block	CSD30A - 170	3365	0.280543	22.876058	0.000627	3.767916	0.280502	-3.73	3.84
Caldeirão Complex	Southern Gavião Block	CSD30A - 171	3419	0.280605	29.063642	0.000670	4.032957	0.280561	-0.34	3.70
Caldeirão Complex	Southern Gavião Block	CSD30A - 172	3419	0.280523	26.542929	0.000603	3.658697	0.280484	-3.09	3.85
Caldeirão Complex	Southern Gavião Block	CSD30A - 173	3384	0.280587	21.917864	0.000720	4.324051	0.280540	-1.89	3.76
Caldeirão Complex	Southern Gavião Block	CSD30A - 174	3391	0.280626	29.547840	0.000672	4.037416	0.280582	-0.25	3.67
Caldeirão Complex	Southern Gavião Block	CSD30A - 175	3393	0.280615	55.107375	0.000703	4.278781	0.280569	-0.68	3.69
Caldeirão Complex	Southern Gavião Block	CSD30A - 176	3367	0.280521	15.293659	0.000200	1.213962	0.280508	-3.47	3.83
Caldeirão Complex	Southern Gavião Block	CSD30A - 177	3393	0.280561	21.551106	0.000558	3.441748	0.280524	-2.26	3.78
Caldeirão Complex	Southern Gavião Block	CSD30A - 178	3415	0.280544	24.711313	0.000557	3.510892	0.280507	-2.34	3.80
Caldeirão Complex	Southern Gavião Block	CSD30A - 179	3418	0.280529	21.695591	0.000474	2.918537	0.280498	-2.62	3.82
Caldeirão Complex	Southern Gavião Block	CSD30A - 180	3378	0.280410	49.184303	0.000387	2.375689	0.280385	-7.60	4.06
Caldeirão Complex	Southern Gavião Block	CSD30A - 181	3398	0.280574	32.900255	0.000521	3.626856	0.280539	-1.60	3.75
Caldeirão Complex	Southern Gavião Block	CSD30A - 182	3388	0.280554	23.935783	0.000504	3.322929	0.280521	-2.49	3.79
Caldeirão Complex	Southern Gavião Block	CSD30A - 183	3378	0.280548	21.758224	0.000526	3.162611	0.280514	-2.99	3.81
Caldeirão Complex	Southern Gavião Block	CSD30A - 184	3389	0.280590	27.069034	0.000252	1.937310	0.280573	-0.61	3.69
Caldeirão Complex	Southern Gavião Block	CSD30A - 185	3400	0.280526	20.660194	0.000486	3.709377	0.280495	-3.14	3.84
Caldeirão Complex	Southern Gavião Block	CSD30A - 186	3391	0.280595	22.855323	0.000469	2.943852	0.280565	-0.88	3.70
Caldeirão Complex	Southern Gavião Block	CSD30A - 187	3386	0.280495	24.201708	0.000626	5.188655	0.280454	-4.94	3.92
Mundo Novo	Northern Gavião Block	PO119-01	3279	0.28055987	1.05439E-05	0.000886421	1.1233E-06	0.280503906	-5.69	3.67
Mundo Novo	Northern Gavião Block	PO119-02	3273	0.280584964	1.01987E-05	0.000847097	1.74378E-06	0.280531588	-4.85	3.63
Mundo Novo	Northern Gavião Block	PO119-03	3300	0.280723776	1.00753E-05	0.001233767	7.64688E-06	0.280645365	-0.15	3.49
Mundo Novo	Northern Gavião Block	PO119-04	3314	0.280682256	9.9285E-06	0.000954266	4.92095E-07	0.280621341	-0.67	3.52
Mundo Novo	Northern Gavião Block	PO119-05	3295	0.280572368	1.03245E-05	0.001287021	1.11149E-06	0.28049072	-5.80	3.69
Mundo Novo	Northern Gavião Block	PO119-06	3301	0.280578973	1.04621E-05	0.001457013	2.27365E-06	0.280486367	-5.81	3.70
Mundo Novo	Northern Gavião Block	PO119-07	3287	0.280669565	1.07709E-05	0.000965677	4.26127E-07	0.280608453	-1.79	3.53
Mundo Novo	Northern Gavião Block	PO119-08	3297	0.280702935	9.70307E-06	0.001186752	1.60327E-05	0.280627596	-0.87	3.51
Mundo Novo	Northern Gavião Block	PO119-08	3315	0.280654882	9.45244E-06	0.001290186	1.12151E-06	0.280572521	-2.41	3.58
Mundo Novo	Northern Gavião Block	PO119-10	3292	0.280649721	9.98087E-06	0.001177614	7.98107E-07	0.280575085	-2.86	3.58
Mundo Novo	Northern Gavião Block	PO119-11	3330	0.280634069	8.41804E-06	0.000851842	3.76246E-06	0.280579434	-1.80	3.57
Mundo Novo	Northern Gavião Block	PO119-12	3313	0.280604441	8.50036E-06	0.001069751	2.44503E-06	0.280536178	-3.73	3.63
Mundo Novo	Northern Gavião Block	PO119-13	3319	0.28060743	8.19191E-06	0.000907753	6.34535E-07	0.280549406	-3.13	3.61
Mundo Novo	Northern Gavião Block	PO119-14	3293	0.280677462	7.83756E-06	0.001519716	1.17515E-05	0.280581092	-2.61	3.57

Mundo Novo	Northern Gavião Block	PO119-15	3286	0.280704477	1.07737E-05	0.001637375	1.52237E-05	0.280600895	-2.09	3.55
Mundo Novo	Northern Gavião Block	PO119-16	3328	0.280642314	1.08255E-05	0.001868568	7.1751E-06	0.28052253	-3.87	3.65
Mundo Novo	Northern Gavião Block	PO119-17	3284	0.280633962	7.98287E-06	0.001438849	6.57118E-06	0.280542979	-4.18	3.62
Mundo Novo	Northern Gavião Block	PO119-18	3302	0.280652655	9.44568E-06	0.00226744	5.16635E-06	0.280508463	-4.98	3.68
Mundo Novo	Northern Gavião Block	PO119-19	3280	0.280590761	9.99927E-06	0.00177566	7.96553E-07	0.280478643	-6.58	3.72
Mundo Novo	Northern Gavião Block	PO119-20	3316	0.280736092	1.00469E-05	0.001808942	5.85015E-06	0.280620565	-0.66	3.52
Mundo Novo	Northern Gavião Block	PO119-21	3313	0.280723988	1.10999E-05	0.001806217	4.51536E-06	0.280608736	-1.15	3.54
Mundo Novo	Northern Gavião Block	PO119-22	3288	0.280680617	9.54403E-06	0.001819878	1.33472E-05	0.280565418	-3.30	3.60
Mundo Novo	Northern Gavião Block	PO119-23	3289	0.280637037	9.51078E-06	0.001811739	6.98255E-06	0.28052231	-4.81	3.66
Mundo Novo	Northern Gavião Block	PO119-24	3316	0.280636036	1.02819E-05	0.001766282	9.19304E-06	0.280523237	-4.13	3.65
Mundo Novo	Northern Gavião Block	PO119-25	3302	0.280691774	1.12012E-05	0.001953216	1.12747E-05	0.280567572	-2.88	3.60
Mundo Novo	Northern Gavião Block	PO119-26	3292	0.280712156	1.02757E-05	0.001909259	2.51574E-06	0.280591148	-2.29	3.56
Mundo Novo	Northern Gavião Block	PO119-27	3306	0.280642005	8.44989E-06	0.001194818	1.8823E-06	0.280565924	-2.84	3.59
Mundo Novo	Northern Gavião Block	PO119-28	3297	0.28069447	9.86606E-06	0.001037883	9.28415E-07	0.28062858	-0.83	3.51
Mundo Novo	Northern Gavião Block	PO119-29	3297	0.280632258	1.09614E-05	0.001791875	1.47687E-06	0.28051848	-4.74	3.66
Mundo Novo	Northern Gavião Block	PO119-30	3295	0.280563859	9.91556E-06	0.000778484	2.87137E-07	0.280514464	-4.94	3.66
Piritiba	Northern Gavião Block	17ED-14-1-z14c	3609	0.280347	0.000015	0.000719	0.000004	0.280297	-5.21	3.93
Piritiba	Northern Gavião Block	17ED-14-1-z17c	3589	0.280372	0.000013	0.000225	0.000004	0.280356	-3.57	3.85
Piritiba	Northern Gavião Block	17ED-14-1-z12c	3598	0.280349	0.000017	0.001216	0.000007	0.280265	-6.63	3.98
Piritiba	Northern Gavião Block	17ED-14-1-z8c	3601	0.2804	0.000013	0.000719	0.000005	0.280350	-3.51	3.87
Piritiba	Northern Gavião Block	17ED-14-1-z27c	3579	0.280391	0.000015	0.000892	0.000006	0.280329	-4.77	3.89
Piritiba	Northern Gavião Block	17ED-14-1-z31c	3584	0.28047	0.000015	0.000483	0.000003	0.280437	-0.83	3.75
Piritiba	Northern Gavião Block	17ED-14-1-z29	3585	0.28039	0.000012	0.000755	0.000005	0.280338	-4.33	3.88
Piritiba	Northern Gavião Block	18DE-17-z28ac	3589	0.280392	0.000017	0.000438	0.000003	0.280362	-3.38	3.85
Piritiba	Northern Gavião Block	18DE-17-z22c	3585	0.280385	0.000031	0.000779	0.000006	0.280331	-4.57	3.89
Piritiba	Northern Gavião Block	18DE-17-z21c	3576	0.280408	0.000017	0.000712	0.000005	0.280359	-3.79	3.85
Piritiba	Northern Gavião Block	18DE-17-z23c	3553	0.28041	0.000016	0.000795	0.000007	0.280355	-4.46	3.86
Piritiba	Northern Gavião Block	18DE-17-z13c	3581	0.280434	0.000029	0.000872	0.000009	0.280374	-3.14	3.84
Piritiba	Northern Gavião Block	18DE-17-z4c	3592	0.280411	0.000017	0.000738	0.000007	0.280360	-3.37	3.85
Piritiba	Northern Gavião Block	18DE-17-z10c	3620	0.280418	0.000031	0.000844	0.000007	0.280359	-2.73	3.85
Piritiba	Northern Gavião Block	18DE-17-z14c	3598	0.280398	0.000044	0.000458	0.000008	0.280366	-3.00	3.84
Piritiba	Northern Gavião Block	18DE-17-z16c	3620	0.280441	0.000015	0.001135	0.000008	0.280362	-2.64	3.85
Piritiba	Northern Gavião Block	18DE-17-z17c	3609	0.280393	0.000019	0.000569	0.000004	0.280353	-3.20	3.86
Piritiba	Northern Gavião Block	18DE-17-z18c	3561	0.280437	0.000029	0.000884	0.00001	0.280376	-3.53	3.83
Piritiba	Northern Gavião Block	18DE-17-z32c	3595	0.280421	0.000014	0.000796	0.000005	0.280366	-3.09	3.85
Piritiba	Northern Gavião Block	18DE-17-z36ac	3614	0.280422	0.000017	0.000648	0.000006	0.280377	-2.24	3.83
Piritiba	Northern Gavião Block	18DE-17-z41bc	3608	0.280435	0.000015	0.000713	0.000006	0.280385	-2.08	3.82
Piritiba	Northern Gavião Block	18DE-17-z42c	3588	0.280426	0.000021	0.00074	0.000006	0.280375	-2.94	3.83
Piritiba	Northern Gavião Block	18DE-17a-z1c	3609	0.280409	0.000022	0.00078	0.000006	0.280355	-3.15	3.86
Piritiba	Northern Gavião Block	18DE-17a-z2c	3529	0.280424	0.000021	0.000837	0.000006	0.280367	-4.62	3.85
Piritiba	Northern Gavião Block	18DE-17a-z3c	3591	0.280475	0.000023	0.000405	0.000003	0.280447	-0.29	3.74
Piritiba	Northern Gavião Block	18DE-17a-z16c	3559	0.280445	0.000012	0.000595	0.000004	0.280404	-2.58	3.79
Piritiba	Northern Gavião Block	18DE-17a-z26c	3583	0.280483	0.000021	0.001021	0.00001	0.280412	-1.71	3.79
Piritiba	Northern Gavião Block	18DE-17a-z29c	3554	0.280448	0.000027	0.000747	0.000006	0.280397	-2.96	3.81
Piritiba	Northern Gavião Block	18DE-17a-z44c	3554	0.280416	0.000015	0.000383	0.000003	0.280390	-3.22	3.81
Piritiba	Northern Gavião Block	18DE-17a-z39c	3553	0.280468	0.000019	0.000771	0.000008	0.280415	-2.33	3.78
Piritiba	Northern Gavião Block	18DE-17a-z33c	3545	0.280456	0.000016	0.000858	0.000008	0.280397	-3.16	3.81
Piritiba	Northern Gavião Block	18DE-17a-z31c	3532	0.280447	0.000022	0.000797	0.000005	0.280393	-3.64	3.81

Piritiba	Northern Gavião Block	18DE-17a-z36c	3570	0.280449	0.000013	0.000923	0.000008	0.280385	-2.99	3.82
Piritiba	Northern Gavião Block	18DE-17a-z43c	3558	0.280481	0.00002	0.000898	0.000006	0.280419	-2.06	3.78
Piritiba	Northern Gavião Block	18DE-1.2-z3c	3619	0.280448	0.000018	0.001471	0.000011	0.280345	-3.25	3.88
Piritiba	Northern Gavião Block	18DE-1.2-z6c	3587	0.280397	0.000018	0.000531	0.000004	0.280360	-3.48	3.85
Piritiba	Northern Gavião Block	18DE-1.2-z5c	3592	0.280398	0.000013	0.000807	0.000005	0.280342	-4.01	3.88
Piritiba	Northern Gavião Block	18DE-1.2-z18c	3548	0.280464	0.000014	0.000913	0.000005	0.280401	-2.94	3.80
Piritiba	Northern Gavião Block	18DE-1.2-z39c	3580	0.280397	0.000015	0.000569	0.000003	0.280358	-3.74	3.85
Piritiba	Northern Gavião Block	18DE-1.2-z41c	3559	0.280405	0.000015	0.000623	0.000004	0.280362	-4.08	3.85
Piritiba	Northern Gavião Block	18DE-1.2-z42c	3584	0.28046	0.000015	0.001178	0.000007	0.280378	-2.90	3.83
Piritiba	Northern Gavião Block	18DE-1.2-z43c	3617	0.280442	0.000012	0.001292	0.000008	0.280352	-3.06	3.87
Piritiba	Northern Gavião Block	18DE-1.2-z60c	3547	0.280449	0.000014	0.000665	0.000004	0.280403	-2.89	3.80
Piritiba	Northern Gavião Block	18DE-1.2-z51c	3589	0.280431	0.000012	0.001264	0.000008	0.280343	-4.64	3.88
Piritiba	Northern Gavião Block	18DE-1.2-z61r	3521	0.28041	0.000014	0.000554	0.000003	0.280372	-5.22	3.84
Piritiba	Northern Gavião Block	18DE-1.2-z54c	3517	0.280428	0.000013	0.000663	0.000004	0.280383	-4.93	3.82
Piritiba	Northern Gavião Block	18DE-1.2-z65c	3580	0.280397	0.000013	0.000329	0.000002	0.280374	-3.76	3.83
Piritiba	Northern Gavião Block	18DE-1.2-z28c	3533	0.28043	0.000014	0.000536	0.000003	0.280393	-4.18	3.81
Piritiba	Northern Gavião Block	18DE-16.1-z2c	3666	0.280334	0.000015	0.001496	0.000009	0.280228	-6.94	4.03
Piritiba	Northern Gavião Block	18DE-16.1-z31c	3680	0.280368	0.000016	0.003023	0.000023	0.280153	-9.28	4.15
Piritiba	Northern Gavião Block	18DE-20-z25c	3649	0.280365	0.000015	0.001214	0.00001	0.280280	-5.51	3.96
Piritiba	Northern Gavião Block	18DE-4.2-z28c	3687	0.280349	0.000017	0.001332	0.000008	0.280254	-5.51	3.99
EO182- HP mafic granulite	Uauá Block	z3c	3097	0.280845906	1.05439E-05	0.000330803	1.1233E-06	0.280826215	1.47	3.25
EO182- HP mafic granulite	Uauá Block	z4c	3132	0.280881662	1.01987E-05	0.000331697	1.74378E-06	0.280861688	3.56	3.20
EO182- HP mafic granulite	Uauá Block	z5c	3173	0.28083739	1.00753E-05	0.000262608	7.64688E-06	0.280821363	3.10	3.25
EO182- HP mafic granulite	Uauá Block	z5r	2829	0.280941024	9.9285E-06	0.000197484	4.92095E-07	0.280930313	-1.15	3.11
EO182- HP mafic granulite	Uauá Block	z6c	3145	0.28084992	1.03245E-05	0.000364639	1.11149E-06	0.280827869	2.67	3.24
EO182- HP mafic granulite	Uauá Block	z7c	3006	0.280854442	1.04621E-05	0.000326004	2.27365E-06	0.280835623	-0.35	3.24
EO182- HP mafic granulite	Uauá Block	z8c	3047	0.280859481	1.07709E-05	0.000279977	4.26127E-07	0.280843092	0.89	3.22
EO182- HP mafic granulite	Uauá Block	z10c	3062	0.280872331	9.70307E-06	0.000341787	1.60327E-05	0.280852223	1.57	3.21
EO182- HP mafic granulite	Uauá Block	z10r	2817	0.280980186	9.45244E-06	0.000233384	1.12151E-06	0.280967583	-0.11	3.06
EO182- HP mafic granulite	Uauá Block	z20c	3099	0.280827321	9.98087E-06	0.000369988	7.98107E-07	0.280805283	1.52	3.27
EO178-D - leucodioritic gneiss	Uauá Block	z2a	3146	0.280734122	8.50036E-06	0.000436219	2.44503E-06	0.280707733	-1.59	3.40
EO178-D - leucodioritic gneiss	Uauá Block	z5	2823	0.280745256	8.19191E-06	0.000338557	6.34535E-07	0.280726934	-8.53	3.38
EO178-D - leucodioritic gneiss	Uauá Block	z6	3171	0.280735523	7.83756E-06	0.000314753	1.17515E-05	0.280716326	-0.69	3.39
EO178-D - leucodioritic gneiss	Uauá Block	z10	3072	0.280754054	1.07737E-05	0.00037	1.52237E-05	0.280732213	-2.47	3.37
EO178-D - leucodioritic gneiss	Uauá Block	z14	3127	0.280749387	1.08255E-05	0.000355996	7.1751E-06	0.280727984	-1.32	3.38
EO178-D - leucodioritic gneiss	Uauá Block	z15	3136	0.280750078	7.98287E-06	0.00100206	6.57118E-06	0.280689656	-2.47	3.43
EO178-D - leucodioritic gneiss	Uauá Block	z17b	3151	0.280758185	9.44568E-06	0.000411608	5.16635E-06	0.280733244	-0.56	3.37
EO178-D - leucodioritic gneiss	Uauá Block	z18	3034	0.280734079	9.99927E-06	0.000509896	7.96553E-07	0.280704362	-4.36	3.41
EO178-D - leucodioritic gneiss	Uauá Block	z23b	3131	0.280757557	1.00469E-05	0.000636593	5.85015E-06	0.280719235	-1.54	3.39

Supplementary material 2 - Hf data for the Eo-to Mesoarchaean units of the northern São Francisco Craton. Soucres: Guitreau *et al.* (2012), Zincone *et al.* (2016), Oliveira *et al.* (2019), Oliveira *et al.* (2020) and Santos *et al.* (2022).

7.3. APÊNDICE 3

Supplementary material 3 – References of the U-Pb, Hf, Nd and Sr isotopes data.

Barbosa, N.S., Teixeira, W., Bastos-Leal, L.R., and Menezes Leal, A.B., 2013, Evolução crustal do setor Ocidental do Bloco Arqueano Gavião, Cráton do São Francisco, com base em evidências U-Pb, Sm-Nd e Rb-Sr. Revista Geologia USP. Série Científica, v. 4, p. 63–88.

Barbosa, N.S., Leal, A.B.M., Debruyne, D., Leal, L.R.B., Barbosa, N.S., Marinho, M.M., Mercês, L., Barbosa, J.S.F., and Koproski, L.M., 2020, Paleoarchean to Paleoproterozoic crustal Evolution in the Guanambi-Correntina Block (GCB), north São Francisco Craton, Brazil, unraveled by U-Pb geochronology, Nd-Sr isotopes and geochemical constraints. Precambrian Research, v. 340, p. 1-16.

Bastos Leal, L.R., Cunha, J.C., Cordani, U.G., Teixeira, W., Nutman, A.P., Leal, A.B.M., and Macambira, M.J.B., 2003, SHRIMP U-Pb, 207Pb/206Pb zircon dating, and Nd isotopic signature of the Umburanas greenstone belt, northern São Francisco craton, Brazil. Journal of South American Earth Sciences, v. 15(7), p. 775-785.

Guitreau, M., Blichert-Toft, J., Martin, H., Mojzsis, S.F., and Albarède, F., 2012, Hafnium isotope evidence from Archean granitic rocks for deep-mantle origin of continental crust. Earth and Planetary Science Letters, v. 337–338, p. 211-223. https://doi.org/10.1016/j.epsl.2012.05.029

Lacerda, C.M.M., 2000, Evolução estrutural e petrogenética do domo granodiorítico de Ambrósio, Bahia: implicações para o mecanismo de colocação.

[Ph.D. thesis]: Campinas, Universidade Estadual de Campinas, 209p.

Leal, L.R.B., 1998. Geocronologia U/Pb (SHRIMP), 207Pb/206Pb, Rb/Sr, Sm/Nd e K/Ar dos Terrenos Granito-Greenstone do Bloco do Gavião: Implicações para a Evolução Arqueana e Paleoproterozoica do Cráton do São Francisco, Brasil. [Ph.D. thesis]: São Paulo, Universidade de São Paulo, 178p.

Leal, L.R.B., Teixeira, W., Cunha, J.C., and Macambira, M.J.B., 1998, Archaean tonalitic-trondhjemitic and granitic plutonism in the Gavião Block, São Francisco Craton, Bahia, Brazil: geochemical and geochronological characteristics. Revista Brasileira de Geociências, v. 28(2), p. 209-220.

Marinho, M.M., 1991. La sequence volcano - sedimentaire de Contendas - Mirante et la bordure occidentale du bloc Jequié (Craton du São Francisco, Brésil): un exemple de transition Archeen – Proterozoique. [Ph.D. thesis]: Clermont Ferrand, Université Blaise Pascal, Clermont Ferrand II, 388p.

Martin, H., Peucat, J.J., Sabaté, P., and Cunha, J.C., 1997, Crustal evolution in the early Archaean of South America: example of the Sete Voltas Massif, Bahia State, Brazil. Precambrian Research, v. 82, p. 35-62. https://doi.org/10.1016/S0301-9268(96)00054-X.

Nutman, A.P., and Cordani, U.G., 1993, SHRIMP U-Pb zircon geochronology of Archaean granitoids from the Contendas-Mirante area of the São Francisco Craton, Bahia, Brazil. Precambrian Research, v. 63, p. 179–188.

Oliveira, E.P., Souza, Z.S., and Correa-Gomes, L.C., 2000, U-Pb dating of deformed mafic dyke and host gneiss: implications for understanding reworking processes on the western margin of the Archaean Uauá Block, NE São Francisco Craton, Brazil. Revista Brasileira de Geociências, v. 30(1), p. 149-152.

Oliveira, E.P., Mello, E.F., and McNaughton, N., 2002a., Reconnaissance U-Pb geochronology of Precambrian quartzites from the Caldeirão belt and their basement, NE São Francisco Craton, Bahia, Brazil: implications for the early evolution of the Paleoproterozoic Itabuna-Salvador-Curaçá Orogen. Journal of South American Earth Sciences, v. 15, p. 349-362.

Oliveira, E.P., Talavera, C., Windley, B.F., Zhao, L., Semprich, J.J., McNaughton, N.J., Amaral, W.S., Sombini, G., Navarro, M., and Silva, D., 2019, Mesoarchean (2820 Ma) high-pressure mafic granulite at Uauá, São Francisco Craton, Brazil, and its potential significance for the assembly of Archaean supercratons. Precambrian Research, v. 331, p. 1-20.

Oliveira, E.P., McNaughton, N.J., Zincone, S.A., and Talavera, C., 2020, Birthplace of the São Francisco Craton, Brazil: evidence from 3.60 to 3.64 Ga Gneisses of the Mairi Gneiss complex. Terra Nova, v. 32, p. 281–289. https://doi.org/10.1111/ter.12460

Peucat, J.J., Mascarenhas, J.F., Barbosa, J.S., Souza, F.S., Marinho, M.M., Fanning, C.M., and Leite, C.M.M., 2002, 3.3 Ga SHRIMP U–Pb zircon age of a felsic metavolcanic rock from the Mundo Novo greenstone belt in the São Francisco Craton, Bahia (NE Brazil). Journal of South American Earth Sciences, v. 15, p. 363–373.

Rios, D.C., 2002a, Granitogênese no Núcleo Serrinha, Bahia, Brasil: geocronologia e litogeoquímica [Ph.D. thesis]: Salvador, Universidade Federal da Bahia, 143p.

Rios, D.C., Davis, D.W., Conceição, H., Davis, W.J., Rosa, M.L.S., and Dickin, A.P., 2009, Geologic evolution of the Serrinha nucleus granite-greenstone terrane

(NE Bahia, Brazil) constrained by U-Pb single zircon geochronology. Precambrian Research, v. 170 (3–4), p. 175–201. https://doi.org/10.1016/j.precamres.2008.10.001.

Santos, C., Zincone, S.A., Queiroga, G.N., Bersan, S.M., Lana, C.C., and Oliveira, E.P., 2022, Evidence for change in crust formation processes during the Paleoarchean in the São Francisco Craton (Gavião Block): Coupled zircon Lu-Hf and U-Pb isotopic analyses and tectonic implications. Precambrian Research, v. 368, 106472. https://doi.org/10.1016/j.precamres.2021.106472

Santos Pinto, M.A., 1996, Le recyclage de la croûte continentale archéenne: exemple du bloc du Gavião-Bahia, Brésil. Mémoires Geosciences Rennes 75 [Ph.D thesis]: Rennes, Université of Rennes, 229p.

Santos-Pinto, M.A., Peucat, J.J., Martin, H., Barbosa, J.S.F., Fanning, C.M., Cocherie, A., and Paquette, J.L., 2012, Crustal evolution between 2.0 and 3.5 Ga in the southern Gavião block (Umburanas-Brumado-Aracatu region), São Francisco Craton, Brazil: A 3.5–3.8 Ga proto-crust in the Gavião block? Journal of South American Earth Sciences, v. 40, p. 129-142.

Sato, K., 1986, Síntese geocronológica do estado da Bahia e evolução crustal, com base no diagrama de evolução do Sr e Razões iniciais 87Sr/86Sr [MSc dissertation]: São Paulo, Universidade de São Paulo, 178p.

Sato, K., 1998, Evolução crustal da Plataforma Sul-Americana com base na geoquímica isotópica Sm-Nd [Ph.D thesis]: São Paulo, Universidade de São Paulo, 325p.

Spreafico, R.R., Barbosa, J.S.F., Barbosa, N.S., and Moraes, A.M.V., 2019, Tectonic Evolution of the Neoarchean Mundo Novo greenstone belt, eastern São

Francisco Craton, NE Brazil: Petrology, U-Pb geochronology, and Nd and Sr constraints. Journal of South American Earth Sciences, v. 95, 102296. https://doi.org/10.1016/j.jsames.2019.102296

Zincone, S.A, Oliveira, E.P., Laurent, O., Zhang, H., and Zhai, M., 2016, 3.30Ga high-silica intraplate volcanic–plutonic system of the Gavião Block, São Francisco Craton, Brazil: Evidence of an intracontinental rift following the creation of insulating continental crust. Lithos, v. 266–267, p. 414-434. https://doi.org/10.1016/j.lithos.2016.10.

7.4. APÊNDICE 4

Supplementary material S1 – Methods

1. Fieldwork and Petrography

During fieldwork, representative samples of the Uauá Block orthogneiss were collected, which allowed the study of their macro and microscopic characteristics, the identification of the rock's mineralogy on both hand specimens and polished thin sections and the observation of the field relations between the orthogneiss and other rocks that occur within the study area.

2. Geochemistry

2.1. Major oxides

Major oxides from three samples of the Uauá Block migmatite-gneiss were analyzed by lithium metaborate fusion digestion and ICP-AES (method ME-ICP06) at ALS Geochemistry Laboratory.

2.2. Trace and rare-earth elements

Major oxides from three samples of the Uauá Block migmatite-gneiss were analyzed by lithium metaborate fusion digestion and ICP-AES (method ME-ICP06) at ALS Geochemistry Laboratory.

3. Geochronology

3.1. Electron microscopy imaging

Petrographic investigation of the samples was based on the optical microscope with cathodoluminescence (CL) and backscattered electron (BSE) images collected using a Zeiss Merlin FE-SEM of the Central Analytical Facility at Stellenbosch University. The imaging was conducted at 10 kV accelerating voltage, 11 nA probe current, with a working distance of 9.5 mm. We divided

the zircons into igneous or magmatic and metamorphic due to their external and internal features (e.g. Corfu et al., 2003). Only a few of our zircon grains are doubly terminated prisms or pyramids and are dark in the CL images (Supplementary Fig. 1). They present internal features such as oscillatory zoning and xenocrystic cores, which are typical features of igneous or magmatic zircons (Corfu et al., 2003). Externally, most of our grains show ovoid or rounded shapes and internally, these zircons, which are bright in the CL images, present features such as metamorphic growth zones, preserved igneous cores and recrystallized domains (Hoskin and Schaltegger, 2003). Since our zircons present the aforementioned characteristics, we defined them as metamorphic zircons.

3.2. U-Pb LA-ICP-MS dating

U-Pb analyses of zircon crystals were carried out on polished thin sections using a 193 nm wavelength Resolution laser ablation system from Applied Spectra coupled to a Thermo Scientific Element 2 single collector magnetic sector field inductively coupled plasma mass spectrometer (SC-SF-ICP-MS) at the Central Analytical Facilities, Stellenbosch University. The mass spectrometer was tuned by ablating a line scan on the NIST610 glass (Jochum et al., 2011) at the start of the analytical session. The torch position, lenses and gas flows settings were optimized while measuring ^{206}Pb, ^{238}U and $^{238}U^{16}O$ to get stable signals and high intensity on ^{206}Pb and ^{238}U, as well as low oxide rates ($^{238}U^{16}O/^{238}U < 0.3\%$). The ablated material was transported from the laser cell in 0.35 l/min of He gas, then mixed with 3 ml/min nitrogen and 0.96 l/min argon before introduction into the ICP-MS. Signals of m/z 202, 204, 206, 207, 208, 232, 235 and 238 were acquired in electrostatic scan mode. The laser

and ICP-MS software packages were synchronized in order to allow automated execution of the analysis. The laser sampling protocol employed a round static spot (with a diameter of 15 and 20 µm for zircon and 20 µm for rutile) and a fluence of ~1.9 J/cm2.

During each analytical session the GJ-1 zircon (Jackson et al., 2004) was used as matrix-matched primary reference material to correct for mass fractionation on measured isotope ratios in unknown zircon, rutile and monazite samples, respectively and simultaneous correction for instrumental drift, while Plešovice zircon (Sláma et al., 2008) was used as secondary reference material.

Data reduction was performed with the software package Iolite v.3.7 (Paton et al., 2011), combined with VizualAge (Petrus and Kamber, 2012). All ages and uncertainties were calculated with IsoplotRgui version 4.3 (Vermeesch, 2018). Common lead correction was applied using a Ms Excel spreadsheet program (Gerdes and Zeh, 2006) based on Stacey and Kramers (1975) Pb composition model. The results table was built according to Horstwood et al. (2016). The U-Pb data are presented in Supplementary Material S3.

4. Lu-Hf isotopes studies

The Lu-Hf isotopic analyses of the previously dated zircon grains took place at the Laboratório de Geoquímica Isotópica of Universidade Federal de Ouro Preto, Brazil. The Lu-Hf data were obtained by using a Thermo-Finnigan Neptune Multicollector ICP-MS coupled with a Photon-Machines 193 nm Excimer Laser System (LA-MC-ICP-MS) according to the methods of Gerdes and Zeh (2006). Laser operated at a spot size of 40 µm and 8 Hz. The performed analyses used the following standards: GJ-1 (Morel et al., 2008), 91500 (Goolaerts et al., 2004), BB (Santos et al., 2017), Temora (Woodhead et al., 2004) and Mud Tank

(Woodhead and Hergt, 2005), which yielded $^{176}Hf/^{177}Hf$ of 0.282000±0.0000005 (n = 10), 0.282677±000013 (n = 10), 0.281674±0000028 (n = 10), 0.282686±0.000007 (n = 11) and 0.282507±000006 (n = 15) respectively.

For the calculation of the εHf values, we used the ^{176}Lu decay constant of $1.867x10^{-11}$ (Scherer et al., 2001) and the values of $^{176}Hf/^{177}Hf$ = 0.282785 and $^{176}Lu/^{177}Hf$ = 0.0336 for the present-day chondrites (Bouvier et al., 2008). For the calculation of the depleted mantle evolution curve and the two-stage Hf model ages, we adopted $^{176}Hf/^{177}Hf$ = 0.28325 and $^{176}Lu/^{177}Hf$ = 0.0388, which are the present-day depleted mantle values of Blichert-Toft and Albarède (2008) and Dhuime et al. (2011). The Lu-Hf data are presented in Supplementary Material S4.

Mostly, the 40 µm Lu-Hf laser spots were drilled “on top” of the 26 µm U-Pb spots. When it was not possible to do so, care was taken to drill the spots in the same domain (e.g. core and/or rim) previously analyzed for U-Pb, characterized by CL imaging.

5. Zircon trace element analysis

LA-ICP-MS trace-element analysis was performed in twenty-one zircon grains from sample RGB-19A of the Uauá Block orthogneiss. The analysis took place at Federal University of Ouro Preto and used a Thermo-Fisher Element 2 mass spectrometer coupled with a 213 nm LSX-213 Teledyne CETAC ablation system. The data was collected during a 30s ablation, using a spot size of 50 µm, frequency of 10 Hz and 4.08 J/cm^2 of fluency. Reference materials utilized were NIST SRM 610 glass (Jochum et al., 2011), BHVO-2 glass (Jochum et al., 2005) and BCR-2 (Jochum et al., 2005). The data were reduced using the methodology reported by Longerich et al. (1996), with Si as an internal standard. The zircon

trace element data is shown in Supplementary Material S5.

The trace elements data were obtained on zircons that were previously observed via CL images, LA-ICP-MS U-Pb dated and analyzed for Lu-Hf isotopes via LA-MC-ICP-MS, and the results allowed the characterization of the nature of the tectonic setting of the studied rock.

References

Blichert-Toft, J., Albarède, F. 2008. Hafnium isotopes in Jack Hills zircons and the formation of the Hadean crust. Earth and Planetary Science Letters 265, 686-702.

Bouvier, A., Vervoort, J.D., Patchett, P.J. 2008. The Lu-Hf and Sm-Nd isotopic composition of CHUR: Constraints from unequilibrated chondrites and implications for the bulk composition of terrestrial planets. Earth and Planetary Science Letters 273(1-2), 48-57. DOI: https://doi.org/10.1016/j.epsl.2008.06.010

Corfu, F., Hanchar, J.M., Hoskin, P.W.O., Kinny, P. 2003. Atlas of zircon textures. In: Hanchar, J.M., Hoskin, P.W.O. (eds). Zircon. Reviews in Mineralogy and Geochemistry 53, 27-62. Mineralogical Society of America, Washington, D.C.

Dhuime, B., Hawkesworth, C.D., Cawood, P. 2011. When continents formed. Science 331, 154-155.

Gerdes, A., Zeh, A. 2006. Combined U-Pb and Hf isotope LA-(MC)-ICP-MS analyses of detrital zircons: comparison with SHRIMP and new constraints for the provenance age of an Armorican metasediment in central Germany. Earth and Planetary Science Letters 249, 47-61. DOI: https://doi.org/10.1016/j.epsl.2006.06.039

Goolaerts, A., Matielli, N., de Jong, J., Weis, D., Scoates, J.S. 2004. Hf and Lu

isotopic reference values for the zircon standard 91500 by MC-ICP-MS. Chemical Geology 206(1-2), 1-9. DOI: https://doi.org/10.1016/j.chemgeo.2004.01.008

Horstwood, M.S.A., Kosler, J., Gehrels, G., Jackson, S.E., McLean, N.M., Paton, C., Pearson, N.J., Sircombe, K., Sylvester, P., Vermeesch, P., Bowring, J.F., Condon, D.J., Schoene, B. 2016. Community-derived standards for LA-ICP-MS U-(Th-)Pb geochronology uncertainty propagation, age interpretation and data reporting. Geostandards and Geoanalytical Research 40 (3), 311–332.

Hoskin, P.W.O., Schaltegger, U. 2003. The composition of zircon and igneous and metamorphic petrogenesis. In: Hanchar, J.M., Hoskin, P.W.O. (eds). Zircon. Reviews in Mineralogy and Geochemistry 53, 27-62. Mineralogical Society of America, Washington, D.C.

Jackson, S.E., Pearson, N. J., Griffin, W.L., Belousova, E.A., 2004. The application of laser ablation-inductively coupled plasma-mass spectrometry to in situ U-Pb zircon geochronology. Chemical Geology 211, 47-69.

Jochum, K.P., Willbold, M., Raczek, I., Stoll, B., Hofmann, A.W. 2005. Geochemical characterization of the USGS reference glasses GSA-1G, GSC-1G, GSD-1G, GSE-1G, BCR-2G, BHVO-2G and BIR-1G using EPMA, ID-TIMS, ID-ICP-MS and LA-ICP-MS. Geostandards and Geoanalytical Research 29, 285-302.

Jochum, K.P., Weis, U., Stoll, B., Kuzmin, D., Yang, Q., Raczek, I., Jacob, D.E., Stracke, A., Birbaum, K., Frick, D.A., Günther, D., Enzweiler, J. 2011. Determination of reference values for NIST SRM 610-617 glasses following ISO guidelines. Geostandards and Geoanalytical Research 35(4), 397-429. DOI: https://doi.org/10.1111/j.1751-908X.2011.00120.x

Longerich, H., Jackson, S., Gunther, D. 1996. Laser ablation inductively coupled plasma mass spectrometric transient signal data acquisition and analyte concentration calculation. Journal of Analytical Atomic Spectrometry 11, 899-904.

Morel, M.L.A., Nebel, O., Nebel-Jacobsen, Y.J., Miller, J.S., Vroon, P.Z. 2008. Hafnium isotope characterization of the GJ-1 reference material by solution and laser-ablation MC-ICPMS. Chemical Geology 255(1-2), 231-235. DOI: https://doi.org/10.1016/j.chemgeo.2008.06.040

Paton, C., Hellstrom, J., Paul, B., Woodhead, J., Hergt, J., 2011. Iolite: freeware for the visualization and processing of mass spectrometric data. J. Anal. At. Spectrom. 26, 2508-2518.

Petrus, J.A., Kamber, B.S. 2012. VizualAge: a novel approach to laser ablation ICP-MS U-Pb geochronology data reduction. Geostand. Geoanal. Res. 36, 247-270.

Santos, M.M., Lana, C., Scholz, R., Buick, I., Schmitz, M.D., Kamo, S.L., Gerdes, A., Corfu, F., Tapster, S., Lancaster, P., Storey, C.D., Basei, M.A.S., Tohver, E., Alkmim, A., Nalini, H., Krambrock, K., Fantini, C., Wiedenbeck, M. 2017. A new appraisal of Sri Lankan BB zircon as a reference material for LA-ICP-MS U-Pb geochronology and Lu-Hf isotope tracing. Geostandards and Geoanalytical Research 41(3), 335-358. DOI: https://doi.org/10.1111/ggr.12167

Scherer, E., Münker, C., Mezger, K. 2001. Calibration of the lutetium-hafnium clock. Science 293, 683-687.

Sláma, J., Košler, J., Condon, D.J., Crowley, J.L., Gerdes, A., Hanchar, J.M., Horstwood, M.S.A., Morrish, G.A., Nadala, L., Noberg, N., Schaltergger, U., Schoene, B., Tubrett, M.N., Whitehouse, M.J. 2008. Plešovice zircon — a new

natural reference material for U-Pb and Hf isotopic microanalysis. Chemical Geology 249 (1–2), 1-35.

Stacey, J.S., Kramers, J.D. 1975. Approximation of terrestrial lead isotope evolution by a two-stage model. Earth Planet Science Letters 26, 207–221.

Vermeesch, P. 2018. IsoplotR: a free and open toolbox for geochronology. Geoscience Frontiers 9, 1479-1493.

Webb, P.C., Potts, P.J., Thompson, M., Gowing, C.J.B., Wilson, S.A. 2021. GeoPT49 – An international proficiency test for analytical geochemistry laboratories – report on round 49 (Basalt, BVA-1)/July 2021. International Association of Geoanalysts and Geostandards Newsletter 49, 1-37.

Woodhead, J.D., Hergt, J.M., Shelley, M., Eggins, S., Kemp, R. 2004. Zircon Hf-isotope analysis with an excimer laser, depth profiling, ablation of complex geometries and concomitant age estimation. Chemical Geology 209, 121-135.

Woodhead, J.D., Hergt, J.M. 2005. A preliminary appraisal of seven natural zircon reference materials for in situ Hf isotope determination. Geostandards and Geoanalytical Research 29, 183-195.

7.5. APÊNDICE 5

Supplementary Material S2 – Whole-rock geochemistry data

Sample	RGB-19A	RGB-19A_1	RGB-19B
Major elements wt.% by ICP-AES			
SiO_2	64.00	64.00	64.70
TiO_2	0.63	0.63	0.63
Al2O3	16.00	16.00	16.00
Fe_2O_3(t)	6.10	6.48	6.48
MnO	0.09	0.09	0.08
MgO	1.62	1.62	1.86
CaO	4.57	4.57	4.47
Na_2O	4.67	4.67	4.62
K_2O	1.04	1.04	1.42
P2O5	0.19	0.19	1.16
LOI (1000 ºC)	0.46	0.46	0.49
Total	99.98	99.98	101.19
Trace elements ppm by ICP-MS			
Be	0.00	0.00	0.00
Sc	0.00	0.00	0.00
V	93.00	93.00	83.00
Cr	26.00	26.00	33.00
Co	0.00	0.00	0.00
Ni	0.00	0.00	0.00
Cu	0.00	0.00	0.00
Zn	0.00	0.00	0.00
Ga	22.60	22.60	23.20
Rb	17.65	18.20	33.80
Y	18.08	21.00	19.50
Sr	359.34	471.00	428.00
Zr	220.80	208.00	228.00
Nb	7.13	7.23	8.55
Mo	0.00	0.00	0.00
Cs	0.38	0.38	0.50
Ba	763.04	713.00	930.00
La	22.64	24.50	29.90
Ce	49.01	48.60	56.20
Pr	4.79	5.66	6.21
Nd	18.17	21.60	23.90
Sm	3.76	4.35	4.48
Eu	1.10	1.36	1.23
Gd	3.80	4.25	4.10
Tb	0.58	0.60	0.67
Dy	3.38	3.55	3.88
Ho	0.68	0.78	0.80
Er	1.84	1.81	2.07
Tm	0.26	0.28	0.26
Yb	1.59	1.89	1.56
Lu	0.23	0.30	0.31
Hf	5.84	4.85	6.12
Ta	0.32	0.50	0.50
Pb	7.10	7.10	0.00
Bi	0.00	0.00	0.00
Th	2.70	1.08	1.89
U	0.54	0.43	0.45

7.6. APÊNDICE 6

Supplementary Figure 1 – CL images of the analyzed zircons.

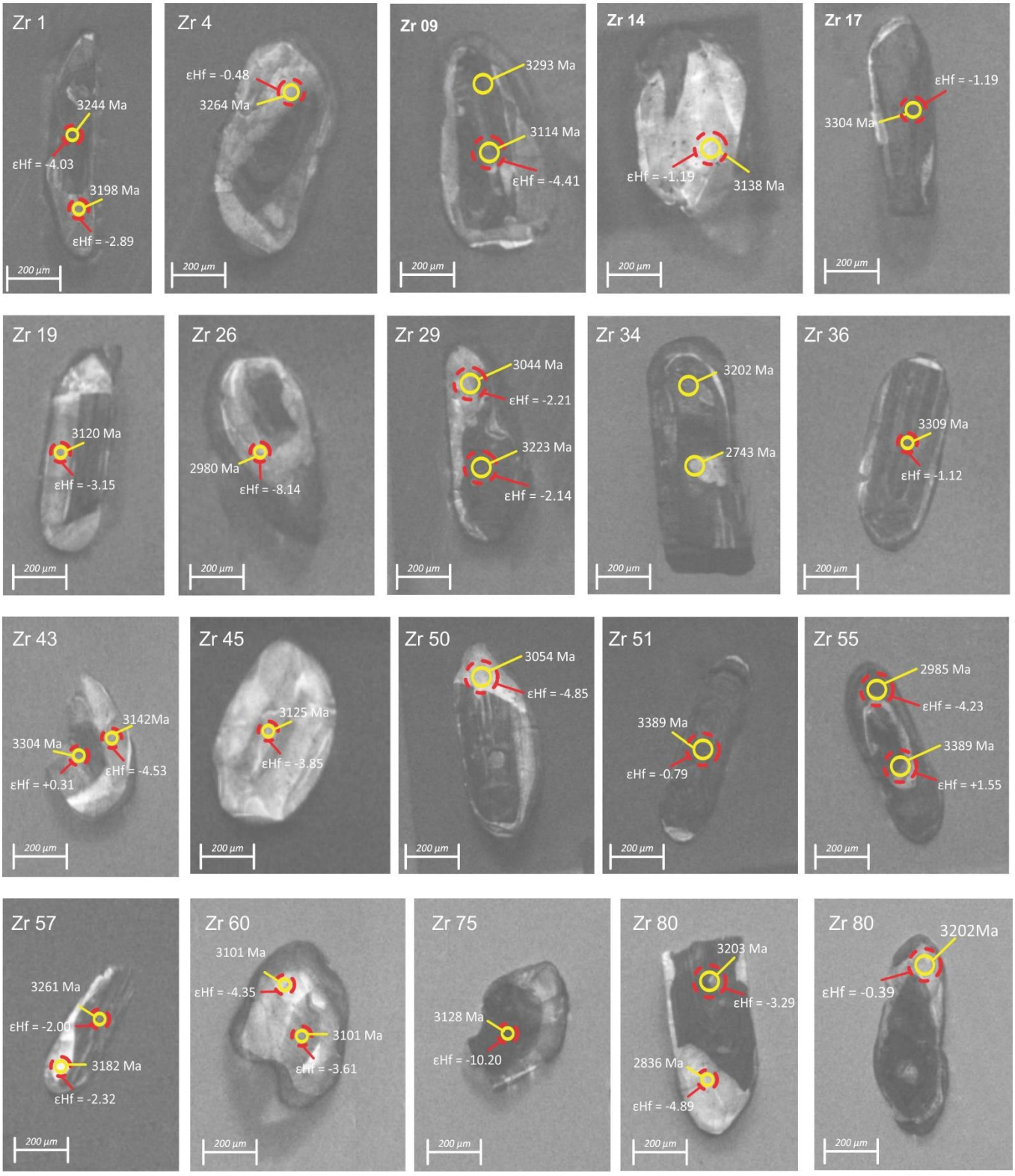

7.7. APÊNDICE 7

Supplementary Material S3 - Zircon U-Pb ages

		Analytical conditions							Plot Age									Final Age									
Sample	Spot	^{202}Hg (CPS)	^{204}Pb (CPS	^{206}Pb (CPS)	^{207}Pb (CPS)	^{232}PTh (CPS)	^{208}Th (CPS)	^{238}U (CPS)	^{207}Pb/^{235}U	2se (abs)	2se (%)	^{206}Pb/^{238}U	2se (abs)	2se (%)	Rho	^{207}Pb/^{206}Pb	2s	^{207}Pb/^{235}U	2s	^{206}Pb/^{238}U	2s	^{207}Pb/^{206}Pb	2s	U (µg/g)	Th(µg/g)	Pb(µg/g)	Th/U ratios
RGB_19A	RGB_19_1	107	59	213100	53200	10150	46400	377000	20.49	0.27	1.317716	0.5876	0.008	1.36147	1.033205	0.2527	0.0025	3116	13	2977	33	3198	16	184.7	38.9	464	0.2106
RGB_19A	RGB_19_2	81	37	120500	31170	18200	86000	192300	23.05	0.31	1.344902	0.639	0.0075	1.173709	0.872709	0.2599	0.0032	3232	13	3191	29	3244	20	94.5	72	830	0.7619
RGB_19A	RGB_19_3	119	88	377000	72000	35100	359000	1.58E+06	6.77	0.18	2.658789	0.2583	0.0053	2.051878	0.771734	0.191	0.0019	2080	24	1479	27	2752	17	777	302	1606	0.3887
RGB_19A	RGB_19_4	131	-1	195500	51400	18200	78200	328000	24.03	0.32	1.331669	0.6509	0.0088	1.351974	1.015248	0.2649	0.0029	3267	13	3236	34	3273	17	161.3	65.5	832	0.4061
RGB_19A	RGB_19_5	143	73	302000	79500	38400	234000	595000	20.99	0.61	2.906146	0.578	0.015	2.595156	0.892989	0.2628	0.0029	3133	28	2936	62	3264	17	293	195	1750	0.6655
RGB_19A	RGB_19_6	177	36	303200	72500	32220	185200	677000	15.24	0.3	1.968504	0.4487	0.0088	1.961221	0.9963	0.2418	0.0028	2829	19	2386	39	3131	19	332.6	152.9	1474	0.4597
RGB_19A	RGB_19_7	100	105	44460	10790	48900	249400	150600	10.94	0.34	3.107861	0.341	0.012	3.519062	1.13231	0.2436	0.0068	2520	29	1884	58	3135	43	73.9	204.1	2240	2.7618
RGB_19A	RGB_19_8	232	106	381700	85900	52000	434000	1.32E+06	9.69	0.17	1.754386	0.3112	0.0051	1.638817	0.934126	0.2258	0.0019	2407	16	1745	25	3020	13	647	350.8	2381	0.5422
RGB_19A	RGB_19_9	328	17	86800	20760	45500	204700	152900	20.28	0.22	1.084813	0.609	0.0076	1.247947	1.150381	0.2395	0.0026	3105	10	3066	31	3114	18	74.8	163.2	2086	2.1818
RGB_19A	RGB_19_10	188	24	379000	100900	88100	408000	661000	23.13	0.26	1.124081	0.6267	0.0082	1.308441	1.164009	0.268	0.0023	3232	11	3139	33	3293	14	323	320	4040	0.9907
RGB_19A	RGB_19_11	158	76	194000	37400	7900	45600	551000	9.65	0.25	2.590674	0.353	0.0097	2.747875	1.06068	0.1954	0.0028	2399	25	1951	47	2787	23	273	33.1	363	0.1212
RGB_19A	RGB_19_12	244	165	906000	211100	161000	1.34E+06	3.24E+06	9.61	0.18	1.873049	0.2929	0.0043	1.468078	0.78379	0.2387	0.0027	2397	17	1655	22	3113	18	1609	969	7400	0.6022
RGB_19A	RGB_19_13	50	4	365700	91900	31700	185800	735000	21.07	0.57	2.705268	0.612	0.014	2.287582	0.845603	0.2522	0.0037	3138	26	3076	57	3200	22	366	134.3	1458	0.3669
RGB_19A	RGB_19_14	139	-24	26690	6440	17580	81500	47300	20.66	0.45	2.178122	0.6214	0.0099	1.593177	0.731445	0.2431	0.0048	3121	21	3112	39	3138	30	23.59	59	809	2.5011
RGB_19A	RGB_19_15	115	10	90000	19600	9430	41000	161000	18.15	0.3	1.652893	0.564	0.011	1.950355	1.179965	0.2298	0.0039	2994	16	2882	43	3048	27	81	29.8	434	0.3679
RGB_19A	RGB_19_16	231	61	349800	70400	46200	395800	1.23E+06	8.56	0.13	1.518692	0.3055	0.0044	1.440262	0.948357	0.2017	0.0022	2290	14	1717	22	2838	18	613	288.1	2126	0.4700
RGB_19A	RGB_19_17	240	-7	180500	48200	24820	109500	308100	25.13	0.39	1.55193	0.685	0.012	1.751825	1.128804	0.2697	0.0034	3311	15	3359	45	3304	19	154.4	80.1	1143	0.5188
RGB_19A	RGB_19_18	223	114	374000	94000	49600	380000	931000	15.92	0.56	3.517588	0.46	0.015	3.26087	0.927019	0.2509	0.0027	2862	34	2431	68	3189	17	467	279	2290	0.5974
RGB_19A	RGB_19_19	126	17	83200	19690	20200	96600	146400	21.51	0.36	1.67364	0.652	0.011	1.687117	1.008052	0.2401	0.0031	3161	16	3237	42	3120	21	73.3	71.4	932	0.9741
RGB_19A	RGB_19_20	195	1470	293000	68100	82000	131800	1.43E+06	7.09	0.72	10.15515	0.227	0.013	5.726872	0.563938	0.2156	0.0094	2042	74	1308	66	2924	66	713	98.1	3800	0.1376
RGB_19A	RGB_19_21	199	136	267400	61100	34400	253600	963000	9.63	0.3	3.115265	0.3047	0.0085	2.789629	0.895471	0.2305	0.0031	2386	29	1710	42	3052	21	481	189.6	1588	0.3942
RGB_19A	RGB_19_22	118	78	321400	77800	35700	232900	795000	14.76	0.61	4.132791	0.447	0.015	3.355705	0.811971	0.2421	0.0032	2797	41	2378	70	3129	21	396	175	1646	0.4419
RGB_19A	RGB_19_23	140	125	431000	86000	54100	495000	1.68E+06	8.18	0.25	3.056235	0.3019	0.0097	3.212984	1.051289	0.2015	0.0048	2247	27	1699	48	2840	37	836	373	2500	0.4462
RGB_19A	RGB_19_24	68	205	555000	110800	56000	490000	2.37E+06	6.88	0.2	2.906977	0.2478	0.0055	2.219532	0.763519	0.202	0.0026	2086	26	1425	28	2837	21	1172	369	2589	0.3148
RGB_19A	RGB_19_26	106	35	83500	18360	9670	56000	156100	17.37	0.26	1.496834	0.5709	0.0084	1.471361	0.982982	0.2198	0.0031	2960	14	2908	35	2980	22	75.2	41.3	448	0.5492
RGB_19A	RGB_19_27	200	112	212000	52300	42300	237000	562000	15.38	0.61	3.96619	0.451	0.016	3.547672	0.894479	0.2444	0.0026	2827	37	2393	68	3146	17	269	173	1960	0.6431
RGB_19A	RGB_19_28	112	33	324000	61000	27450	238700	1.25E+06	7.33	0.19	2.592087	0.2823	0.0064	2.267092	0.87462	0.1897	0.0021	2145	24	1603	32	2735	19	591	172.4	1272	0.2917
RGB_19A	RGB_19_29	131	76	135000	34800	24000	113300	218000	21.84	0.4	1.831502	0.6182	0.0086	1.391136	0.75956	0.2565	0.0028	3179	18	3099	34	3223	17	102.9	81	1115	0.7872
RGB_19A	RGB_19_30	94	6	25600	5810	1080	5200	49900	19.45	0.58	2.982005	0.623	0.016	2.568218	0.861239	0.2297	0.0051	3062	28	3121	60	3044	35	23.4	3.68	49.9	0.1573
RGB_19A	RGB_19_31	120	59	219800	46900	28800	218000	598000	13.47	0.57	4.231626	0.458	0.02	4.366812	1.031947	0.2188	0.0036	2719	40	2424	91	2974	27	279	153	1337	0.5484
RGB_19A	RGB_19_32	118	2200	679000	174000	301000	529000	2.14E+06	12.88	0.83	6.444099	0.372	0.017	4.569892	0.709159	0.2487	0.0049	2612	49	2024	74	3176	31	994	368	14000	0.3702
RGB_19A	RGB_19_33	133	544	529000	115200	93900	687000	2.20E+06	7.87	0.26	3.303685	0.2622	0.0072	2.745995	0.831192	0.2164	0.0026	2207	30	1498	37	2952	20	1015	474	4360	0.4670
RGB_19A	RGB_19_34	206	2	69100	17500	14330	70000	122300	22.99	0.66	2.870813	0.652	0.013	1.993865	0.69453	0.2532	0.0047	3217	28	3240	51	3202	29	56.3	48.1	666	0.8544
RGB_19A	RGB_19_35	230	122	289300	55000	39550	434600	1.43E+06	6.27	0.2	3.189793	0.2421	0.0085	3.510946	1.100682	0.19	0.0027	2007	28	1395	44	2743	24	659	297.9	1839	0.4520
RGB_19A	RGB_19_36	95	2	294400	79400	37300	174000	499000	23.95	0.32	1.336117	0.6405	0.0095	1.483216	1.110095	0.2702	0.0023	3265	13	3191	37	3309	13	230.2	119.2	1735	0.5178
RGB_19A	RGB_19_37	138	64	243400	53000	25100	151000	828000	9.56	0.62	6.485356	0.314	0.015	4.77707	0.736593	0.2154	0.0047	2364	59	1754	72	2935	36	383	104	1170	0.2715
RGB_19A	RGB_19_38	174	28	121000	31900	21300	112000	236000	20.84	0.52	2.495202	0.568	0.013	2.288732	0.917254	0.2635	0.0033	3129	24	2893	54	3265	20	110	78	990	0.7091
RGB_19A	RGB_19_39	103	58	154900	41700	10060	101700	305000	20.24	0.36	1.778656	0.547	0.01	1.828154	1.027829	0.2671	0.003	3103	17	2811	43	3289	17	142.9	71.5	469	0.5003
RGB_19A	RGB_19_41	140	68	299600	69400	35140	220600	770000	13.43	0.19	1.414743	0.4163	0.006	1.441268	1.018749	0.2346	0.0024	2712	14	2244	27	3084	17	378	168	1640	0.4444
RGB_19A	RGB_19_42	208	104	398000	73200	85600	1.02E+06	1.90E+06	5.63	0.24	4.262877	0.221	0.0068	3.076923	0.721795	0.1854	0.003	1903	33	1284	36	2695	27	939	783	4000	0.8339
RGB_19A	RGB_19_43	134	4	276600	73800	26720	115700	450000	24.87	0.31	1.246482	0.6673	0.0088	1.318747	1.057976	0.2698	0.0022	3305	12	3292	34	3304	13	224.3	90.1	1249	0.4017
RGB_19A	RGB_19_44	122	18	78700	19390	12920	55300	136600	20.32	0.39	1.919291	0.597	0.011	1.842546	0.960014	0.2438	0.0032	3103	19	3017	47	3142	21	68.6	43.3	604	0.6312
RGB_19A	RGB_19_45	45	19	32400	7720	20590	93600	56600	20.85	0.35	1.678657	0.6267	0.009	1.436094	0.855502	0.2399	0.0037	3130	16	3133	36	3125	24	28.6	73.4	963	2.5664
RGB_19A	RGB_19_46	44	38	27980	6910	25870	129300	55200	19.08	0.38	1.991614	0.5534	0.0083	1.499819	0.753067	0.2497	0.0045	3042	19	2839	34	3176	30	28	100.1	1213	3.5750
RGB_19A	RGB_19_47	120	28	310800	80700	38130	180800	544000	23.87	0.34	1.424382	0.667	0.011	1.649175	1.157818	0.2611	0.0028	3264	14	3292	41	3252	17	274.3	138.6	1789	0.5053
RGB_19A	RGB_19_48	130	3	44800	10390	25900	126600	81600	20.41	0.45	2.204802	0.627	0.013	2.073365	0.940386	0.2364	0.0053	3108	22	3144	54	3093	35	41	96.2	1215	2.3463
RGB_19A	RGB_19_49	105	5	162000	41900	21200	181000	317000	19.61	0.51	2.600714	0.549	0.012	2.185792	0.840459	0.2561	0.0032	3066	25	2820	49	3227	20	158	136	1000	0.8608
RGB_19A	RGB_19_50	152	-4	46700	10880	5900	27460	84400	19.59	0.32	1.633486	0.6064	0.0083	1.368734	0.837922	0.2319	0.0035	3070	16	3059	33	3064	24	41.8	20.44	277.2	0.4890
RGB_19A	RGB_19_51	106	8	288000	74400	38700	188000	509000	23.39	0.41	1.752886	0.656	0.012	1.829268	1.043575	0.2592	0.0028	3242	17	3252	47	3242	17	249	139	1820	0.5582
RGB_19A	RGB_19_53	244	317	160000	29000	24700	60000	596000	7.8	0.37	4.74359	0.299	0.011	3.67893	0.775558	0.1889	0.0037	2197	45	1679	53	2728	32	282	42.9	1163	0.1521
RGB_19A	RGB_19_54	100	24	96300	24440	26310	134400	166100	23.83	0.52	2.182123	0.68	0.015	2.205882	1.010888	0.2558	0.0035	3257	21	3346	55	3218	21	78.6	97	1240	1.2341
RGB_19A	RGB_19_55	215	2130	379000	108700	148500	1.36E+06	1.79E+06	8.49	0.15	1.766784	0.2154	0.0036	1.671309	0.945961	0.2847	0.0028	2282	16	1257	19	3389	15	848	988	7000	1.1651
RGB_19A	RGB_19_56	123	5	340000	74500	47500	244000	692000	16.41	0.19	1.157831	0.5408	0.006	1.109467	0.95823	0.2206	0.0017	2900	11	2790	26	2985	13	330	178.6	2242	0.5412
RGB_19A	RGB_19_57	196	8	270300	71000	35520	151700	476100	23.53	0.4	1.699958	0.654	0.011	1.681957	0.989411	0.2624	0.0029	3254	17	3259	42	3261	17	228.3	112	1677	0.4906
RGB_19A	RGB_19_58	126	31	370000	93300	38500	250000	862000	16.73	0.69	4.124328	0.486	0.02	4.115226	0.997793	0.25	0.0027	2919	39	2539	88	3182	17	416.7	186.4	1820	0.4473
RGB_19A	RGB_19_59	170	215	499000	118100	52000	844000	1.94E+06	10.37	0.31	2.989392	0.3175	0.0079	2.488189	0.832339	0.2385	0.0035	2463	28	1776	39	3110	23	950	636	2460	0.6695
RGB_19A	RGB_19_60	102	-3	54000	12890	32900	152400	98000	19.86	0.3	1.510574	0.6049	0.0079	1.306001	0.864573	0.2376	0.003	3084	15	3047	32	3101	20	48.2	116.2	1557	2.4108
RGB_19A	RGB_19_61	104	7	28400	6610	5910	28400	52300	18.97	0.43	2.266737	0.582	0.011	1.890034	0.833813	0.2386	0.0046	3038	22	2951	45	3101	31	25.9	21.9	279	0.8456
RGB_19A	RGB_19_62	202	361	235400	56500	73000	118600	528000	15.01	0.93	6.195869	0.453	0.019	4.19426	0.676945	0.2329	0.0052	2790	59	2392	83	3072	37	263.9	92	3470	0.3486
RGB_19A	RGB_19_63	2	-10	33380	7760	31920	149100	59900	19.3	0.34	1.761658	0.6035	0.0086	1.425021	0.808909	0.2325	0.0043	3057	17	3044	35	3062	30	30.09	116.2	1512	3.8617
RGB_19A	RGB_19_67	81	244	325000	60600	29000	310000	1.84E+06	5.43	0.3	5.524862	0.2053	0.0083	4.042864	0.731758	0.1862	0.0035	1847	48	1202	45	2709	31	894	227	1380	0.2539
RGB_19A	RGB_19_68	151	33	269000	65200	46000	316000	691000	14.94	0.78	5.220884	0.438	0.019	4.3379	0.830875	0.245	0.0036	2782	51	2327	85	3152	23	331	225	2180	0.6798
RGB_19A	RGB_19_69	54	53	298000	64500	35100	336000	1.05E+06	9.93	0.2	2.014099	0.3239	0.0053	1.636308	0.812427	0.2192	0.0023	2426	19	1809	26	2972	17	493	232.8	1668	0.4722

RGB_19A	RGB_19_70	66	32	53440	12690	33200	166500	100900	18.78	0.35	1.863685	0.5691	0.0098	1.722017	0.923985	0.2383	0.0035	3026	18	2899	40	3106	23	46.57	112.2	1578	2.4093
RGB_19A	RGB_19_71	116	137	1.55E+06	383000	89900	391000	3.43E+06	16.62	0.36	2.166065	0.4903	0.0099	2.019172	0.932184	0.2444	0.0022	2911	20	2572	42	3152	14	1557	257	4280	0.1651
RGB_19A	RGB_19_73	175	91	238000	58100	54900	535000	693000	11.76	0.42	3.571429	0.346	0.012	3.468208	0.971098	0.2428	0.0028	2579	32	1918	56	3136	18	304	335	2620	1.1020
RGB_19A	RGB_19_74	103	18	74700	16410	16900	79800	137600	17.86	0.28	1.567749	0.589	0.0082	1.39219	0.888018	0.2209	0.0026	2984	15	2986	33	2988	19	59.7	49.1	806	0.8224
RGB_19A	RGB_19_75	20	87	224200	44400	21960	247000	923000	7.61	0.16	2.102497	0.2726	0.005	1.834189	0.872386	0.2008	0.002	2186	18	1552	25	2834	17	395	150	1048	0.3797
RGB_19A	RGB_19_76	205	-5	57200	13920	38640	183600	106600	20.71	0.46	2.221149	0.629	0.013	2.066773	0.930497	0.2411	0.0044	3131	23	3141	53	3128	28	45.4	110.6	1845	2.4361
RGB_19A	RGB_19_78	170	50	44900	9910	16650	93000	105100	14.72	0.36	2.445652	0.4714	0.0091	1.93042	0.789327	0.2247	0.004	2792	23	2490	39	3014	29	45	56.6	796	1.2578
RGB_19A	RGB_19_79	118	64	447000	91300	72000	408000	1.01E+06	13.59	0.17	1.25092	0.4751	0.0063	1.326037	1.060049	0.2078	0.002	2719	12	2504	28	2888	15	439	252.6	3442	0.5754
RGB_19A	RGB_19_80	220	20	323200	81700	41500	183700	587000	22.53	0.48	2.130493	0.655	0.013	1.984733	0.931584	0.2528	0.0034	3204	20	3245	52	3203	22	259	116.7	1987	0.4506
RGB_19A	RGB_19_81	122	-4	22950	5420	4370	20600	41400	19.56	0.42	2.147239	0.6048	0.0097	1.603836	0.746929	0.2347	0.0045	3064	21	3049	39	3075	31	22.5	17.78	209.7	0.7902
RGB_19A	RGB_19_82	170	56	95800	19100	20420	103200	249400	11.03	0.45	4.079782	0.393	0.014	3.562341	0.873169	0.2009	0.0031	2518	38	2129	67	2836	26	137.4	90.1	981	0.6557
RGB_19A	RGB_19_83	163	19	177800	44800	14410	64000	313000	21.57	0.26	1.205378	0.6179	0.0079	1.278524	1.060683	0.2528	0.0025	3166	12	3099	31	3202	15	172.9	55.7	692	0.3222
GJ1 standard	Z_GJ1_1	94	64	53800	3200	567	12460	596000	0.801	0.019	2.372035	0.097	0.0013	1.340206	0.565003	0.0609	0.0014	598	11	596.7	7.4	642	49	280	9.52	25.8	0.0340
GJ1 standard	Z_GJ1_2	98	41	55500	3340	537	12230	641000	0.812	0.023	2.832512	0.0975	0.0014	1.435897	0.506934	0.0612	0.0016	603	13	599.8	8.1	631	55	303	9.54	24.5	0.0315
GJ1 standard	Z_GJ1_3	232	13	52400	3100	522	11860	586000	0.783	0.021	2.681992	0.0962	0.0013	1.351351	0.503861	0.0587	0.0014	586	12	591.7	7.5	535	55	279	9.47	23.8	0.0339
GJ1 standard	Z_GJ1_4	350	11	53900	3180	599	12610	588000	0.803	0.019	2.366127	0.0983	0.0014	1.424212	0.601917	0.059	0.0014	597	11	604.2	8.1	574	53	288	9.46	27.5	0.0328
GJ1 standard	Z_GJ1_5	249	71	53200	3210	579	12930	581000	0.823	0.02	2.430134	0.098	0.0013	1.326531	0.545867	0.061	0.0016	609	11	602.6	7.7	633	56	286	9.57	26.6	0.0335
GJ1 standard	Z_GJ1_6	192	44	53600	3203	550	12630	584000	0.831	0.02	2.406739	0.1	0.0013	1.3	0.54015	0.0602	0.0014	616	11	614.2	7.6	602	49	287	9.5	25.4	0.0331
GJ1 standard	Z_GJ1_7	182	25	55400	3290	577	13450	614000	0.834	0.024	2.877698	0.0995	0.0016	1.60804	0.558794	0.0599	0.0018	615	14	611.5	9.3	594	67	290	9.65	26.9	0.0333
GJ1 standard	Z_GJ1_8	274	-14	53500	3190	569	12770	591000	0.815	0.018	2.208589	0.0987	0.0014	1.41844	0.642238	0.0599	0.0014	604	10	606.5	8.4	592	50	283	9.36	26.5	0.0331
GJ1 standard	Z_GJ1_9	82	46	52600	3120	557	12960	583000	0.803	0.021	2.615193	0.0983	0.0012	1.220753	0.466793	0.0596	0.0015	598	12	604.8	6.9	579	55	282	9.45	26.2	0.0335
GJ1 standard	Z_GJ1_10	236	75	54200	3230	565	13250	609000	0.799	0.022	2.753442	0.0978	0.0015	1.533742	0.557027	0.0599	0.0018	594	13	601.3	8.9	602	64	292	9.58	26.6	0.0328
GJ1 standard	Z_GJ1_11	277	20	51700	3150	543	12450	572000	0.831	0.02	2.406739	0.0982	0.0014	1.425662	0.592363	0.0611	0.0013	613	11	603.7	8.5	630	48	286	9.49	25.8	0.0332
GJ1 standard	Z_GJ1_12	158	-5	52100	3130	536	12710	581000	0.826	0.02	2.421308	0.0982	0.0012	1.221996	0.504684	0.061	0.0013	610	11	603.5	7.3	658	47	287	9.51	25.5	0.0331
GJ1 standard	Z_GJ1_13	266	43	55300	3350	573	14280	640000	0.817	0.021	2.570379	0.0975	0.0014	1.435897	0.558632	0.0604	0.0016	607	12	599.4	8.2	625	57	302	10.04	27.5	0.0332
GJ1 standard	Z_GJ1_14	278	38	50200	2970	562	11970	548000	0.792	0.021	2.651515	0.0969	0.0012	1.23839	0.46705	0.0592	0.0016	590	12	596.2	7.1	563	59	272	9.05	27	0.0333
GJ1 standard	Z_GJ1_15	226	37	53000	3100	568	13080	600000	0.8	0.02	2.5	0.0978	0.0012	1.226994	0.490798	0.0596	0.0017	594	11	601.1	7.1	562	61	294	9.89	27.5	0.0336
GJ1 standard	Z_GJ1_16	288	59	50100	3040	477	11760	572000	0.8	0.019	2.375	0.0969	0.0014	1.444788	0.608332	0.06	0.0014	595	11	595.9	8.2	573	52	281	9.22	23.1	0.0328
GJ1 standard	Z_GJ1_17	166	47	51000	3060	480	11630	568000	0.816	0.019	2.328431	0.0986	0.0013	1.318458	0.566243	0.0603	0.0014	606	11	605.7	7.8	601	51	286	9.5	23.4	0.0332
GJ1 standard	Z_GJ1_18	283	74	51300	3100	496	11810	574000	0.812	0.019	2.339901	0.097	0.0013	1.340206	0.572762	0.0602	0.0013	603	11	596.5	7.4	597	47	288	9.53	24.2	0.0331
GJ1 standard	Z_GJ1_19	206	41	50700	3020	488	11600	572000	0.813	0.021	2.583026	0.0981	0.0013	1.325178	0.513033	0.0597	0.0015	604	12	603	7.7	577	54	288	9.55	24	0.0332
GJ1 standard	Z_GJ1_20	225	61	49900	3030	513	11460	566000	0.813	0.018	2.214022	0.097	0.0011	1.134021	0.512199	0.0608	0.0015	603	10	596.8	6.7	628	53	285	9.45	25	0.0332
GJ1 standard	Z_GJ1_21	138	30	52600	3251	581	12720	610000	0.817	0.019	2.325581	0.0981	0.0014	1.427115	0.61366	0.061	0.0016	606	11	602.9	8.2	626	59	291	9.65	28.7	0.0332
GJ1 standard	Z_GJ1_22	173	15	51200	3130	550	11960	579000	0.815	0.018	2.208589	0.0975	0.0013	1.333333	0.603704	0.0604	0.0014	604	10	599.5	7.6	598	52	282	9.35	27.1	0.0332
GJ1 standard	Z_GJ1_23	122	37	50400	3040	485	11550	564000	0.808	0.024	2.970297	0.098	0.0012	1.22449	0.412245	0.059	0.0017	601	13	602.3	7.3	567	59	282	9.38	24	0.0333
GJ1 standard	Z_GJ1_24	119	1	53300	3210	525	12230	599000	0.827	0.023	2.781137	0.099	0.0013	1.313131	0.472156	0.06	0.0015	610	12	608.7	7.4	610	53	294	9.71	26	0.0330
GJ1 standard	Z_GJ1_25	155	5	50400	3100	500	11490	565000	0.815	0.019	2.331288	0.0981	0.0013	1.325178	0.568432	0.0604	0.0014	606	11	604	7.4	606	51	281	9.2	24.9	0.0327
GJ1 standard	Z_GJ1_26	130	26	51100	3090	560	12980	598000	0.806	0.021	2.605459	0.0974	0.0012	1.232033	0.472866	0.0601	0.0014	603	12	599.5	7.4	598	53	295	9.88	27.9	0.0335
GJ1 standard	Z_GJ1_27	76	13	50200	2990	498	11870	573000	0.799	0.021	2.628285	0.0972	0.0012	1.234568	0.469724	0.0599	0.0016	596	12	598.4	7.3	583	58	286	9.29	24.9	0.0325
GJ1 standard	Z_GJ1_28	160	29	51200	3060	539	12890	584000	0.806	0.02	2.48139	0.0987	0.0014	1.41844	0.571631	0.0593	0.0014	598	11	606.5	8	568	52	288	9.7	27	0.0337
GJ1 standard	Z_GJ1_29	180	33	55600	3290	553	14070	657000	0.803	0.022	2.739726	0.099	0.0014	1.414141	0.516162	0.0596	0.0016	598	12	608.3	7.9	567	62	300	10.19	27.8	0.0340
GJ1 standard	Z_GJ1_30	127	21	49900	3050	504	11720	578000	0.815	0.017	2.08589	0.0975	0.0012	1.230769	0.590045	0.061	0.0013	604.2	9.7	599.4	6.8	618	46	274	9.07	25.3	0.0331
GJ1 standard	Z_GJ1_31	114	15	52300	3090	504	11870	580000	0.808	0.022	2.722772	0.0985	0.0014	1.42132	0.522012	0.0593	0.0015	600	12	605.6	8	579	54	291	9.64	25.4	0.0331
GJ1 standard	Z_GJ1_32	277	63	49800	3050	495	11700	567000	0.812	0.019	2.339901	0.0969	0.0013	1.341589	0.573353	0.0611	0.0014	603	11	595.9	7.5	633	51	285	9.42	24.9	0.0331
91500 standard	Z_91500_1	79	32	15410	1212	1404	18550	92700	1.858	0.084	4.52099	0.1718	0.0031	1.804424	0.399121	0.0782	0.0037	1067	30	1021	17	1133	90	44.7	15.1	64	0.3378
91500 standard	Z_91500_2	133	-23	17480	1294	1544	21410	105800	1.851	0.063	3.403566	0.1784	0.003	1.681614	0.494074	0.0751	0.0026	1064	22	1057	16	1050	72	51.7	16.59	70.8	0.3209
91500 standard	Z_91500_3	76	43	18220	1398	1650	23640	115700	1.902	0.083	4.363828	0.1828	0.0031	1.695842	0.388614	0.0766	0.0036	1082	29	1082	17	1108	95	58.6	18.55	77.2	0.3166
91500 standard	Z_91500_4	124	1	16460	1232	1483	20770	101700	1.868	0.066	3.533191	0.1748	0.0028	1.601831	0.453367	0.0768	0.0029	1060	24	1038	16	1084	75	46.2	13.78	71	0.2983
91500 standard	Z_91500_5	34	-14	16160	1190	1431	20590	101700	1.772	0.069	3.893905	0.1738	0.0024	1.380898	0.354631	0.0742	0.0029	1041	26	1033	13	1018	83	50.9	16.36	70	0.3214
91500 standard	Z_91500_6	160	6	16150	1215	1473	20410	101600	1.797	0.059	3.28325	0.1751	0.0028	1.599086	0.487044	0.0749	0.0026	1051	22	1041	15	1075	68	49	15.93	73.1	0.3251
91500 standard	Z_91500_7	122	29	15940	1194	1421	19920	99100	1.828	0.073	3.993435	0.1764	0.0028	1.587302	0.397478	0.0753	0.0028	1051	26	1047	15	1079	78	42.3	11.77	71.3	0.2783
Plešovice standard	Z_Ples_1	760	158	63200	3350	2430	99900	1.26E+06	0.392	0.01	2.55102	0.05383	0.0008	1.48616	0.582575	0.0535	0.0013	334.9	7.5	338	4.9	331	56	618	83.3	110.7	0.1348
Plešovice standard	Z_Ples_2	638	183	59900	3240	1775	80600	1.22E+06	0.399	0.012	3.007519	0.05382	0.00086	1.597919	0.531308	0.0537	0.0014	340.6	8.7	337.9	5.3	343	57	604	59	81.5	0.0977
Plešovice standard	Z_Ples_3	679	150	58000	3037	1780	77100	1.18E+06	0.4006	0.0096	2.396405	0.05489	0.00091	1.657861	0.691812	0.0533	0.0013	342.1	7.1	344.4	5.6	337	52	598	60.1	83.5	0.1005
Plešovice standard	Z_Ples_4	570	103	69800	3760	2350	112500	1.54E+06	0.408	0.014	3.431373	0.0553	0.001	1.808318	0.526996	0.0537	0.0017	346.9	9.9	346.7	6.3	361	75	819	94.3	112.8	0.1151
Plešovice standard	Z_Ples_5	750	106	76200	3980	2640	115500	1.63E+06	0.395	0.011	2.78481	0.05381	0.00085	1.579632	0.567232	0.0525	0.0013	336.9	7.9	337.8	5.2	312	58	817	92.6	129	0.1133
Plešovice standard	Z_Ples_6	631	137	59200	3080	1870	78100	1.24E+06	0.3902	0.0095	2.434649	0.054	0.00071	1.314815	0.540043	0.0523	0.0013	335.1	7	339	4.3	309	53	589	60.8	92.8	0.1032
Plešovice standard	Z_Ples_7	770	127	57400	3027	1777	76800	1.20E+06	0.392	0.0097	2.47449	0.05384	0.00069	1.281575	0.517915	0.0527	0.0013	335	7.1	338	4.2	317	53	509	45.4	89.1	0.0892
Plešovice standard	Z_Ples_8	520	128	64900	3530	2126	91500	1.34E+06	0.402	0.01	2.487562	0.05408	0.00074	1.368343	0.550074	0.0539	0.0013	343.3	7.2	339.5	4.5	346	54	670	75.3	107	0.1124

7.8. APÊNDICE 8

Supplementary Material S4 - Lu-Hf isotopes data.

Sample	CL feature and Spot position	$^{176}Yb/^{177}Hf$ [a]	±2σ	$^{176}Lu/^{177}Hf$	±2σ	$^{178}Hf/^{177}Hf$	$^{180}Hf/^{177}Hf$	Sig_{Hf} [b]	$^{176}Hf/^{177}Hf$	±2σ [c]	$^{176}Hf/^{177}Hf_{(t)}$ [d]	εHf(t) [d]
ZR-01	Black core	0.037473	40	0.001657	15	1.467093	1.886965	8	0.280707	23	0.280605	-4.03
ZR-02	White rim	0.007229	6	0.000325	2	1.467237	1.886945	9	0.280626	17	0.280606	-2.89
ZR-04	White rim	0.032171	30	0.001324	11	1.467184	1.886917	9	0.280738	23	0.280654	-0.48
ZR-08	Black grain	0.027658	22	0.001190	7	1.467159	1.887030	8	0.280707	19	0.280638	-7.06
ZR-09	White rim	0.030039	25	0.001188	8	1.467198	1.886889	8	0.280721	23	0.280650	-4.41
ZR-14	White rim	0.007574	6	0.000317	2	1.467134	1.886823	8	0.280665	22	0.280646	-3.99
ZR-17	Black core	0.021522	38	0.000890	15	1.467216	1.886815	9	0.280670	23	0.280614	-1.19
ZR-19	Black core	0.011531	10	0.000486	3	1.467205	1.886908	9	0.280710	23	0.280681	-3.15
ZR-26	Black grain	0.036509	34	0.001496	12	1.467216	1.887020	9	0.280720	23	0.280634	-8.14
ZR-28	Black grain	0.028024	23	0.001158	7	1.467155	1.886979	9	0.280694	19	0.280634	-13.91
ZR-29	White rim	0.012014	15	0.000510	5	1.467168	1.886881	9	0.280671	25	0.280639	-2.21
ZR-30	Black core	0.012047	14	0.000544	6	1.467181	1.887002	8	0.280650	22	0.280616	-2.14
ZR-31	White rim	0.007441	6	0.000329	2	1.467209	1.886857	9	0.280651	21	0.280632	-6.72
ZR-36	Black core	0.015801	15	0.000660	5	1.467152	1.887033	10	0.280655	23	0.280612	-1.12
ZR-43	Black core	0.009519	8	0.000410	3	1.467157	1.886849	9	0.280690	24	0.280664	0.61
ZR-44	White rim	0.014287	12	0.000623	4	1.467162	1.886670	9	0.280665	21	0.280628	-4.53
ZR-45	White core	0.010778	11	0.000456	4	1.467169	1.886903	8	0.280686	21	0.280658	-3.85
ZR-50	White rim	0.008197	7	0.000317	2	1.467135	1.886860	9	0.280689	22	0.280671	-4.85
ZR-51	Black core	0.041972	38	0.001749	13	1.467187	1.886937	7	0.280775	26	0.280666	-0.79
ZR-55	Black core	0.034981	36	0.001339	11	1.467154	1.886746	7	0.280721	23	0.280634	1.55
ZR-56	Black rim	0.014648	12	0.000600	4	1.467114	1.886995	10	0.280775	20	0.280741	-4.23
ZR-57	Black core	0.012012	16	0.000483	6	1.467133	1.886821	8	0.280650	24	0.280620	-2.00
ZR-57	White rim	0.008732	9	0.000360	3	1.467212	1.886839	8	0.280739	24	0.280717	-2.32
ZR-60	Black core	0.007233	6	0.000303	2	1.467242	1.886951	8	0.280699	20	0.280681	-3.61
ZR-61	White rim	0.008897	7	0.000347	2	1.467144	1.886879	9	0.280681	19	0.280660	-4.35
ZR-75	Black grain	0.028407	26	0.001251	9	1.467197	1.886924	9	0.280741	23	0.280673	-10.20
ZR-76	White rim	0.006512	5	0.000290	2	1.467135	1.886833	9	0.280658	16	0.280641	-4.40
ZR-80	Black core	0.031173	25	0.001327	8	1.467226	1.886907	9	0.280704	18	0.280622	-3.29
ZR-81	White rim	0.013288	11	0.000485	3	1.467186	1.886787	8	0.280691	19	0.280662	-4.89
ZR-83	White rim	0.010511	9	0.000425	3	1.467158	1.886754	9	0.280730	18	0.280704	-0.39

e - Avg. MORB: Chauvel et al. (2008), f - BLIC TDM: Blichert-Toft et al. (2008), g - NC TDM: Dhuime et al. (2011).

±2σ [c]	age [f]	±2σ	$^{176}Hf/^{177}Hf_{(Avg\ MORB)}$ [e d]	Avg MORB[e]	$^{176}Hf/^{177}Hf_{(DM2)}$ [f d]	T_{DM2} [f]	$^{176}Hf/^{177}Hf_{(DM2)}$ [g d]	T_{DM2} [g]
1.13	**3198**	16	0.280801	3.59	0.280874	3.73	0.280738	3.46
0.87	**3244**	20	0.280766	3.56	0.280838	3.70	0.280702	3.43
1.14	**3273**	17	0.280744	3.45	0.280816	3.59	0.280680	3.32
0.95	**3020**	13	0.280937	3.61	0.281013	3.76	0.280877	3.49
1.14	**3114**	18	0.280865	3.54	0.280940	3.68	0.280804	3.42
1.09	**3138**	30	0.280847	3.53	0.280921	3.68	0.280785	3.41
1.15	**3304**	19	0.280721	3.52	0.280792	3.65	0.280656	3.39
1.16	**3120**	21	0.280861	3.47	0.280935	3.62	0.280799	3.35
1.15	**2980**	22	0.280967	3.63	0.281044	3.78	0.280908	3.52
0.97	**2735**	19	0.281152	3.75	0.281234	3.91	0.281098	3.64
1.23	**3223**	17	0.280782	3.51	0.280855	3.65	0.280719	3.38
1.10	**3261**	17	0.280753	3.53	0.280825	3.67	0.280689	3.41
1.07	**3044**	35	0.280918	3.61	0.280994	3.76	0.280858	3.49
1.14	**3309**	13	0.280717	3.52	0.280788	3.65	0.280652	3.39
1.19	**3304**	13	0.280721	3.42	0.280792	3.55	0.280656	3.29
1.04	**3142**	21	0.280844	3.57	0.280918	3.71	0.280782	3.45
1.06	**3125**	24	0.280857	3.52	0.280931	3.66	0.280795	3.39
1.11	**3064**	24	0.280903	3.52	0.280979	3.67	0.280843	3.40
1.28	**3242**	17	0.280768	3.44	0.280840	3.58	0.280704	3.32
1.16	**3389**	15	0.280656	3.43	0.280725	3.57	0.280589	3.30
0.99	**2985**	13	0.280963	3.42	0.281040	3.57	0.280904	3.31
1.20	**3261**	17	0.280753	3.52	0.280825	3.67	0.280689	3.40
1.22	**3101**	31	0.280875	3.41	0.280950	3.56	0.280814	3.29
1.02	**3101**	20	0.280875	3.48	0.280950	3.63	0.280814	3.36
0.94	**3101**	31	0.280875	3.52	0.280950	3.67	0.280814	3.40
1.13	**2834**	17	0.281078	3.63	0.281157	3.78	0.281021	3.52
0.78	**3128**	28	0.280855	3.55	0.280929	3.69	0.280793	3.43
0.89	**3203**	22	0.280798	3.55	0.280870	3.69	0.280734	3.42
0.93	**3075**	31	0.280895	3.53	0.280970	3.68	0.280834	3.41
0.88	**3202**	15	0.280798	3.39	0.280871	3.53	0.280735	3.26

7.9. APÊNDICE 9

Supplementary Material S5 - Zircon trace elements data.

Sample	Spot location	Mg	Al	Si	Ca 43	Ca 44	Sc	Ti 47	Ti 49	V	Cr	Mn	Fe
ZR-18	Core	672.7935	1535.319	149579.7	31747.99	16149.2	717.4301	1119.366	95.6774	13.0065	-321.88	176.2151	2379.086
ZR-76	White rim	389.8354	4594.347	149579.7	26188.27	23172.83	1112.909	2176.244	207.2104	44.0345	2595.864	479.275	5972.429
ZR-17	Black core	981.6024	2531.363	149579.7	9880.001	19194.02	669.424	1201.502	167.5041	21.2632	-393.786	106.3713	2871.066
ZR-04	White rim	617.1938	2551.819	149579.7	45068.8	12818.49	931.164	1389.44	187.7795	19.0594	-96.82	127.3905	2884.777
ZR-25	Rim	1386.29	4416.095	149579.7	48722.64	9958.29	827.5261	1305.025	137.911	32.8304	7.135	112.7774	3525.149
ZR-08	Black grain	345.3211	1932.172	149579.7	110830.7	19325.1	1129.259	1963.525	718.1327	21.8167	-160.385	85.9045	2849.256
ZR-51	Black core	74.9056	1559.058	149579.7	75373.14	13417.48	1208.249	1862.33	75.4605	2.7598	-119.543	122.4558	1956.262
ZR-29	White rim	153.9928	625.2382	149579.7	44498.3	8402.811	924.8375	1251.723	39.6798	3.3845	-189.868	196.2274	2041.619
ZR-80	Black core	10.8237	229.1826	149579.7	15442.49	13468.41	1069.678	2309.94	36.2989	4.8194	207.7685	58.5473	984.6465
ZR-83	White rim	45.0731	241.4277	149579.7	4711.417	4552.815	1026.935	2381.744	6.5023	0.465	229.7389	4.2365	213.2508
ZR-02	White rim	77.9249	660.4289	149579.7	33631.3	6452.87	903.5256	1225.034	13.1916	-0.3653	-71.312	44.0103	937.7179
ZR-78	Rim	447.5396	1091.561	149579.7	3977.055	7046.749	1128.096	2218.842	20.3056	0.7983	568.8319	20.2982	1073.441
ZR-55	Black core	9.6022	295.8491	149579.7	64499.06	12024.52	1436.532	1827.627	21.4432	1.9082	-163.309	69.635	187.0985
ZR-30	Core	8.9297	109.565	149579.7	21602.74	4711.073	1256.301	1546.936	6.9186	1.1369	-68.8099	2.6012	122.9295
ZR-36	Black core	178.9021	371.625	149579.7	20633.3	22438.19	735.3357	1114.654	13.4892	2.6303	-184.302	10.4434	299.8763
ZR-57	Black core	39.7417	375.6981	149579.7	102015.9	1874.407	1313.789	1877.799	9.7472	0.8014	-86.2909	2.319	282.4654
ZR-68	Core	415.4982	445.7781	149579.7	-1204.91	20201.84	1276.274	1892.993	8.2479	2.3774	48.7299	5.5497	557.0921
ZR-43	Black core	-40.8509	105.6942	149579.7	28287.46	21437.5	818.0924	1227.919	5.2573	0.6977	20.5238	1.3686	27.7314
ZR-50	White rim	11.8228	153.3892	149579.7	52826.49	13708.4	1119.074	1646.782	8.9492	-1.5451	-61.4812	0.5332	19.511
ZR-14	White rim	4.2304	28.1974	149579.7	24976.33	24768.02	931.6271	2315.042	19.8179	-0.6723	121.6846	1.8323	86.4926
ZR-45	White core	-49.0209	207.0677	149579.7	70719.71	4090.609	1234.528	1681.104	13.559	2.0794	-105.47	1.2424	34.8594

Co	Ni	Cu	Zn	Ga	Ge	Rb	Sr	Y	Zr	Nb	Mo	Cd	Sn	Sb
1.8817	-2.794	117.1894	15.8876	3.0969	63.6147	0.4916	16.0583	3658.109	860921.8	6.6206	2.6737	14.2675	0.5291	0.3922
1.2868	2.0925	85.9722	57.2182	18.6159	81.3409	1.186	64.7611	2248.167	663945	13.1629	3.1897	7.7587	0.7475	0.2795
1.8313	2.1811	79.5489	-12.9845	3.5673	50.8733	1.4785	13.8576	3757.285	872943.7	11.6047	4.8861	16.8308	0.7811	0.2472
0.6805	0.4293	16.6344	41.7573	4.49	27.6414	0.6295	35.1261	3977.48	944617.4	19.2167	2.8775	10.2302	1.1036	0.1066
2.7978	3.028	16.6958	68.5269	8.3704	53.8784	3.1147	17.6685	2902.329	1018279	10.4944	3.2436	12.5764	1.002	0.2836
0.7759	1.4269	32.0491	37.6328	1.3781	36.774	0.9707	13.2823	2998.15	1000694	7.1062	3.9679	12.1058	0.3012	-0.1988
0.1928	1.0687	7.6294	18.6078	2.0961	7.6316	0.5185	63.2771	1672.824	963349.8	3.9911	3.7808	12.7268	0.5784	0.0977
0.3012	0.4962	38.3174	23.5293	4.2182	10.4503	0.5839	29.9754	3887.125	1039161	19.6657	1.7512	16.6298	0.1066	-0.0438
0.135	0.2327	12.7538	9.1829	0.7248	7.6446	0.5715	3.5847	1638.953	604746.6	5.0284	1.3432	7.3604	0.2387	0.149
0.3644	0.8773	9.9361	10.4339	0.5264	3.1869	0.307	0.8279	449.3851	608157	1.6657	1.2105	7.1064	1.289	-0.18
0.4316	0.8186	15.084	5.2058	1.5679	10.4005	0.4568	4.1463	646.8602	941086.9	3.0129	2.4248	11.779	0.3577	0.138
2.1262	1.7509	17.5159	21.5275	1.4573	6.7612	0.4113	0.692	1249.328	666949	4.2445	2.4899	7.441	0.4978	0.1612
0.3508	0.5167	7.2587	19.2675	1.1245	8.8825	0.5148	2.0142	1442.814	1026387	5.0631	2.2878	11.5073	0.284	0.091
0.103	0.1609	0.7747	-10.4348	-0.43	0.8192	0.268	1.0725	1154.141	1066739	6.1411	-0.1435	13.8403	0.198	-0.0188
0.2263	0.5418	3.5234	6.9821	-0.6648	0.3532	1.6411	2.2147	1153.574	1005883	3.6296	8.7413	15.3729	-0.1008	-0.1047
0.0824	0.1738	1.1474	-1.9909	-0.1296	0.9535	0.498	0.6545	1074.634	983994.7	2.0095	1.3507	10.5417	0.1693	0.1689
0.8277	1.0431	11.6684	8.9535	-0.1271	1.1146	0.572	0.3209	428.5468	896359.8	1.7575	23.0662	11.3886	0.002	-0.0791
0.0013	0.3857	0.4785	-13.3903	-0.3808	1.7029	0.0445	-0.0539	581.0809	917649.7	2.2222	2.6088	14.9407	0.3933	0.0191
-0.0355	0.0998	1.3062	-6.4803	-0.2556	1.3517	0.0749	0.1666	494.0918	963013.2	2.0861	1.9735	12.9796	0.0303	0.2994
0.031	0.2503	0.7679	15.6503	1.1114	0.1327	0.2535	0.4333	285.0314	566427	1.4857	1.5403	6.4995	-0.1173	0.055
-0.0186	0.3699	3.0295	12.038	0.9823	0.2766	0.2285	0.618	456.6455	1056419	1.3146	0.6925	14.5741	0.2291	-0.1789

Cs	Ba	La	Ce	Pr	Nd	Sm	Eu	Gd	Tb	Dy	Ho	Er	Tm	Yb
0.0168	21.5438	328.7977	1484.485	139.4338	909.5441	483.2749	43.4679	326.2579	34.0259	323.0437	60.4031	223.0868	53.6464	884.9273
0.0193	98.6767	304.3028	1114.138	245.1448	1779.548	618.9899	72.3194	393.6272	37.3926	236.5264	50.0879	222.4948	52.4361	1125.84
-0.0212	13.5383	228.8292	1496.797	126.1805	897.9404	604.2074	58.2118	436.6159	53.395	422.2746	75.1905	243.6786	55.1366	747.827
0.0182	22.9611	73.3296	571.9405	40.4892	298.7429	251.7035	22.983	181.5471	22.7105	263.5503	61.8365	239.9675	57.4802	953.1413
0.0926	44.773	56.8611	868.4755	78.8737	716.6555	575.2243	53.3863	389.4059	40.4247	334.556	57.4727	170.4693	38.9856	578.5842
0.0177	18.3255	56.4943	532.6175	45.7145	417.2981	287.43	24.1431	178.044	20.2702	219.69	44.2358	152.6476	40.2029	647.8995
0.0246	16.0148	44.9573	199.1896	14.8082	102.3385	50.8923	4.609	41.0528	6.1143	92.2973	28.804	136.5535	33.8816	598.9357
0.0167	30.2843	36.4314	160.533	16.5052	121.6975	104.075	9.1216	79.7088	13.2263	220.2744	64.1987	260.3894	66.8211	1126.502
0.0239	3.3044	27.8022	146.421	15.2194	129.5028	88.7268	12.5504	76.0365	11.8894	112.1056	31.5146	149.6174	32.578	547.0434
0.0072	1.3619	25.2744	64.0918	5.9084	55.6197	28.6544	3.9433	23.3759	4.0451	38.3738	11.7083	58.6923	13.0618	217.5372
0.0076	8.2684	23.7805	142.3944	14.0052	111.2263	46.0823	4.4641	32.4456	3.7297	46.9084	13.2356	57.4899	15.914	272.751
0.0224	0.4696	21.8439	96.784	9.0911	90.2959	65.5853	10.6428	60.6665	9.1462	85.8462	22.4906	99.8428	22.9235	387.4064
0.018	5.634	16.798	78.9437	9.0145	79.543	57.8022	5.59	41.1099	7.5455	92.2286	23.2622	103.7601	24.6265	375.7643
0.0043	1.4097	7.0096	20.7632	1.7153	12.5525	9.9197	1.1642	10.6353	2.3673	61.6275	22.3046	110.0571	33.3427	626.0606
-0.0088	6.8291	3.6152	24.9117	1.6199	17.2513	11.1919	1.4084	14.3178	3.9771	81.889	24.7885	105.8821	27.222	431.0406
0.0325	2.535	3.2607	18.4382	1.7344	13.9556	12.4144	1.4701	14.5527	3.9828	68.2004	19.5963	92.1869	22.6117	373.1305
0.022	1.2756	1.7185	20.5179	0.9511	9.5118	6.7115	0.7605	7.4058	1.7981	38.8797	10.8965	46.0766	11.315	174.8314
-0.0514	0.4366	0.8169	15.7465	1.0901	8.7327	5.6107	0.6776	9.4424	2.406	50.059	13.4362	59.8403	15.2357	245.9562
-0.0053	0.17	0.5047	19.4537	0.3749	2.3911	0.9267	0.1374	4.7958	1.9563	45.0956	13.0703	50.3606	12.2466	191.8083
0.0174	0.4348	0.3873	13.0753	0.3594	3.8096	2.4819	0.6647	6.377	1.7511	25.2976	7.6743	41.6973	9.6364	159.4691
-0.0058	-0.4037	0.2423	15.5206	0.239	1.556	2.4774	0.2605	4.138	1.7804	39.356	11.2798	42.1896	10.3865	168.3294

Lu	Hf	W	Pb	U	Th
148.103	12663.78	0.9247	32.2675	792.0329	466.6095
113.3916	12216.92	0.9227	46.4659	1006.575	431.6411
115.8449	14582.64	1.1394	30.3581	781.1725	747.1228
155.7019	13988.91	0.4631	51.1997	1258.201	447.2868
92.638	15809.34	1.1282	30.9883	773.6117	547.0386
95.6841	12409.4	0.5776	31.0134	543.9115	194.77
96.1996	12150.92	0.1297	22.8087	487.7929	131.8202
178.2655	14374.01	0.2961	39.511	1172.02	542.6324
54.5883	9727.795	0.3007	44.9461	359.1692	304.1032
21.3815	9603.772	-0.014	16.019	111.6151	55.6611
51.4163	12787.02	0.2915	9.6595	331.177	51.6128
39.6254	10114.72	0.0056	30.3208	244.1447	138.0836
52.2303	13820.3	0.1067	26.8571	322.0794	120.1966
109.4099	10097.03	0.0756	16.4215	470.8793	58.8485
72.974	14584.38	0.0948	20.6774	386.7035	75.4233
50.3303	13042.72	-0.1385	26.7112	292.1535	83.5145
24.1224	11622.49	0.1197	24.2954	38.6438	82.8486
43.586	14084.26	-0.0106	12.9009	146.4035	42.3226
26.7561	13412.89	0.1604	5.888	74.267	21.9561
14.9788	8549.303	0.1456	19.6876	76.611	66.317
26.302	12719.17	0.405	17.8811	41.6846	63.2207

ANEXO I

Título da Tese:

“EVOLUÇÃO CRUSTAL EO A MESOARQUEANA DA PARTE NORTE DO CRÁTON DO SÃO FRANCISCO: ASPECTOS GEOCRONOLÓGICOS E ISOTÓPICOS”

Área de Concentração: Geoquímica

Autor: **RAFAEL GORDILHO BARBOSA**

Orientador: Prof. Dr. Rommulo Vieira Conceição (URFGS/PPGGEO)
Coorientador: Prof. Dr. Felipe Padilha Leitzke (UFPEL)

Examinador: Prof. Dr. Lauro Valentim Stoll Nardi

Data: 12 09 2023

Conceito: A

PARECER:

A tese é composta por dois artigos, o primeiro já publicado na International Geology Review, em 2022, intitula-se “A review of 3.66 to 2.77 Ga crustal differentiation in the Northern São Francisco Craton, Brazil”. O segundo – Palaeoarchaean crustal formation in the Uauá Block, northern São Francisco Craton, Brazil: evidence for 3.3 to 3.0 Ga collisional tectonics – foi submetido à Geoscience Frontiers em 2023.

Ambos artigos, sendo o primeiro uma revisão muito bem feita e completa de dados anteriores, são bem escritos e fundamentados, perecendo consistentes na apresentação das discussões e conclusões propostas. As ilustrações são relevantes e de ótima qualidade. Os dados obtidos são muito significativos e as discussões baseadas em artigos bastante qualificados. De acordo com minha opinião, ambos constituem ótimas contribuições ao estudo das rochas, ambientes e processos petrogenéticos atuantes no Arqueano, focando o Cráton do São Francisco.

Concluo, pela atribuição de conceito A.

Assinatura: 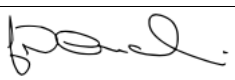 Data: 12 setembro 2023

Ciente do Orientador:

Ciente do Aluno:

ANEXO I

Título da Tese:

“EVOLUÇÃO CRUSTAL EO A MESOARQUEANA DA PARTE NORTE DO CRÁTON DO SÃO FRANCISCO: ASPECTOS GEOCRONOLÓGICOS E ISOTÓPICOS”

Área de Concentração: Geoquímica

Autor: **RAFAEL GORDILHO BARBOSA**

Orientador: Prof. Dr. Rommulo Vieira Conceição (URFGS/PPGGEO)
Coorientador: Prof. Dr. Felipe Padilha Leitzke (UFPEL)

Examinadora: Profa. Dra. Angela Beatriz de Menezes Leal

Data: 12/09/2023

Conceito: A

PARECER:

A tese “Evolução crustal Eo a Mesoarqueana da parte norte do Cráton do São Francisco: aspectos geocronológicos e isotópicos” é estruturada em 7 capítulos, distribuídos em 98 páginas. Apresenta texto organizado, claro, com uma síntese bem-feita. Apresenta raros erros ortográficos. As figuras estão legíveis e em quantidade suficiente. As tabelas estão bem formatadas.

O artigo 1 foi publicado na revista *International Geology Review* e trata da compilação dos 285 dados geocronológicos (U-Pb em zircão) e isotópicos (Hf, Nd e Sr) da literatura sobre as rochas eo a mesoarqueanas da parte norte do Cráton do São Francisco, entre os anos de 1985 a 2022.

O artigo 2 foi submetido à revista *Geoscience Frontiers* e foi elaborado com dados petrográficos, geoquímicos de rocha total, geocronológicos (U-Pb em zircão), isotópicos (Lu-Hf) e de elementos traço em zircão de um gnaisse migmatítico que aflora no Bloco Uauá, na borda nordeste do Cráton do São Francisco.

Algumas sugestões e considerações sobre o texto da tese estão marcadas no volume apresentado, o qual será repassado para o Rafael Gordilho Barbosa.

Na apresentação oral o doutorando mostrou-se seguro e respondeu aos questionamentos com desenvoltura e senso crítico.

A tese apresenta uma contribuição importante para evolução crustal Eo a Mesoarqueana da Parte Norte do Cráton do São Francisco.

Assinatura: Angela Beatriz de Menezes Leal Data: 12/09/2023

Ciente do Orientador:

Ciente do Aluno:

ANEXO I

Título da Tese:

"EVOLUÇÃO CRUSTAL EO A MESOARQUEANA DA PARTE NORTE DO CRÁTON DO SÃO FRANCISCO: ASPECTOS GEOCRONOLÓGICOS E ISOTÓPICOS"

Área de Concentração: Geoquímica

Autor: **RAFAEL GORDILHO BARBOSA**

Orientador: Prof. Dr. Rommulo Vieira Conceição (URFGS/PPGGEO)
Coorientador: Prof. Dr. Felipe Padilha Leitzke (UFPEL)

Examinadora: Profa. Dra. Anelise Losangela Bertotti

Data: 12/09/2023

Conceito: A

PARECER:

Primeiramente, gostaria de agradecer o convite do Programa de Pós-Graduação em Geociências do Instituto de Geociências/UFRGS e dos orientadores Profs. Drs. Rommulo Vieira Conceição e Felipe Padilha Leitzke para compor a banca de avaliação da tese de doutorado intitulada "**Evolução Crustal Eo a Mesoarqueana da Parte Norte do Cráton do São Francisco: Aspectos Geocronológicos e Isotópicos***"* do doutorando **Rafael Gordilho Barbosa**.

De modo geral, o trabalho está bem organizado e escrito apresenta um bom desenvolvimento e discussão dos dados obtidos. Ao longo de todo texto da tese poucos erros de pontuação e de português foram observados. Cabe destacar que o mesmo está obedecendo as normas estabelecidas pelo programa quanto a sua formatação com a escrita de dois artigos, um deles publicado na revista *International Geology Reviews* e outro submetido a *Geoscience Frontiers*.

As correções e os comentários que foram necessários estão assinalados em amarelo e apontados com notas ao longo do texto da tese no arquivo em PDF e que, podem ser conferidos pelo doutorando e seus orientadores no documento anexado ao e-mail de envio do parecer.

No entanto, gostaria de fazer algumas sugestões e destacar alguns pontos ao doutorando e seus orientadores para ficar junto a cópia da tese:

1) No Sumário não deve constar as listas de figuras e abreviações.
2) Na parte introdutória não constam os métodos utilizados para o desenvolvimento da tese, mesmo que eles estejam no material suplementar dos artigos, acho que deveriam estar em português no início da tese. Também os objetivos e questões a serem respondidas com a tese e que foram apresentadas na qualificação não foram adicionadas ao texto final da tese.
3) Em relação a formatação da tese, ficaria melhor os capítulos terem iniciado em uma nova página. Por exemplo, as considerações finais da tese não ganharam destaque, pois iniciou logo após as referências do segundo

artigo.

4) Nos Anexos deveria constar a carta de submissão do segundo artigo a revista *Geoscience Frontiers*, bem como a primeira página do primeiro artigo que foi publicado na *International Geology Reviews*.
5) A notação do Epsilon Hf está apresentada de forma errada ao longo de todo texto da tese, inclusive no artigo já publicado. O correto seria colocar a mesma dessa forma: $\varepsilon_{Hf}(t)$, com HF em subscrito. Também a referencia a idade modelo do manto empobrecido (T_{DM}) deve ser padronizada.
6) Para obtenção dos dados de Hf para o segundo artigo não ficou claro quais grãos de zircão que foram utilizados, se somente os mais concordantes ou se todos que foram analisados para U/Pb foram aproveitados. Também para o cálculo do T_{DM2}, no material suplementar está a tabela com duas colunas com valores do T_{DM2} (Apêndice 8). Quais valores foram os utilizados? Sugiro deixar somente o que foi utilizado para o artigo ou fazer uma discussão maior abordando os diferentes valores encontrados.

Por fim, parabenizo o discente e seus orientadores por sua colaboração com a evolução crustal no arqueano da parte norte do Cráton São Francisco e meu parecer é de A (Excelente).

Assinatura:

Data:12/09/2023

Ciente do Orientador:

Ciente do Aluno: